Technical Report

TR-99-12

Inspection of copper canisters for spent nuclear fuel by means of Ultrasonic Array System

Modelling, defect detection and grain noise estimation

Ping Wu and Tadeusz Stepinski
Uppsala University, Signals and Systems
Department of Material Science

July 1998

Svensk Kärnbränslehantering AB
Swedish Nuclear Fuel
and Waste Management Co
Box 5864
SE-102 40 Stockholm Sweden
Tel 08-459 84 00
+46 8 459 84 00
Fax 08-661 57 19
+46 8 661 57 19

Inspection of copper canisters for spent nuclear fuel by means of Ultrasonic Array System

Modelling, defect detection and grain noise estimation

Ping Wu and Tadeusz Stepinski
Uppsala University, Signals and Systems
Department of Material Science

July 1998

Summary

This report is on phase three of a study aimed at developing ultrasonic array techniques for inspecting welds in copper canisters. The work presented in the report has been split into three overlapping tasks which have the following objectives:

(1) development of beam-forming tools, and verification of modeling tools;

(2) investigation of detection and resolution limits;

(3) evaluation of attenuation, estimation and suppression of grain noise.

For beam-forming tools, a method of designing steered and/or focused beams in immersed solids is presented based on geometrical acoustics. Presently, the beam designs are only related to delays but not to apodization. These focused, steered beams are intended to be used for sizing defects and inspecting the regions close to canisters outer walls.

The modeling tool developed by us previously for simulating elastic fields radiated by planar arrays into immersed solids has been verified by comparing with the results obtained from PASS, a software developed by Dr. Didier Cassereau in Laboratoire Ondes et Acoustique, Universite Paris VII, France. The results from our modeling tool are in excellent agreement with those from PASS.

Since the array coming with the ALLIN ultrasonic array system is not planar, but cylindrically curved in elevation, and it works not in transmission mode, but in pulse echo mode, the above modeling tool for the planar arrays cannot be applied directly. Therefore, the modeling tool has been upgraded for the ALLIN array. The theory underlying this modeling tool is the extended angular spectrum approach (ASA) which was developed based on the conventional ASA that only applies to planar sources. Experimental verification of the modeling tool has shown that the results from the tool agree very well with the measurements. The extended ASA is applicable to the case of an arbitrarily curved source.

To quantify the fields from the ALLIN array and to facilitate the comparison of simulated results with the measured ones, the ALLIN array system has been calibrated based on the existing functionality, and an analytical model has been proposed for simulating measured acoustic echo pulses. For the calibration, several experimental methods have been established for measuring the transmission and reception time delays, and measuring ultrasonic fields from the array.

To investigate the detection and resolution limits, we have carried out a series of experiments. First, the beamforming tool developed in task 1 has been applied to design (electronically) focused beams for the ALLIN array system to perform immersion inspection of copper canisters. Beams focused at different depths have been tested on a copper test block CU2 with a set of side-drilled holes located at different depths. Also, the beamforming tool has been applied to design focused and steered beams for

inspecting of zones close to the outer walls. A copper block CU3 with bottom-drilled holes of various diameter and various distance to the outer wall has been inspected by using focused beams which were steered at various angles. The welds of two copper canister segments with shallow side-drilled holes located close to the outer wall have been examined with focused, steered beams. These experiments have demonstrated that use of focused, steered beams is a very effective solution to the inspection of the zone close to the outer walls of copper canisters, and they have also indicated the most suitable beam angle for this inspection.

For evaluation of attenuation, the log-spectral difference method and the spectral shift method have been employed. Measurements were made on copper specimens of different grades. The results have shown that the spectral shift method gives a stable estimation of attenuation when the echoes from front and back surfaces of a specimen are used. Therefore, the spectral shift method has been chosen for the attenuation evaluation.

For estimation of grain noise, two statistical models, i.e., the independent scattering model (ISM) and the K-distribution model (KDM), are used. The ISM has been applied to estimate grain noise in three copper specimens with different grades. The results have shown that the model gives good prediction under the approximation which is expected to be valid for the early time portion of a signal when the main beam has not been significantly attenuated. They have also demonstrated that the figure of merit (FOM) obtained from the ISM can be a good parameter used for depicting grain noise severity. The KDM has been further exploited and applied to evaluate grain noise from welds in copper canisters, and also applied to detect defects in welds.

To suppress structure noise in weld, formerly developed frequency diversity technique has been applied. Unfortunately, no improvement has been observed after processing the ultrasonic data using noncoherent detector (NCD). A novel technique based on the concept of spatial diversity has been proposed for the suppression of noise in the weld zone. The spatial diversity is realized by using a set of beams steered at different angles by the array. The preliminary tests have shown some potential for the noise suppression, but more effort is needed to evaluate it.

CONTENTS

1 Beam-forming and modeling tools

1.1 Introduction

Our previous work has shown that ultrasonic array technique is an effective means to inspect copper canisters [1,2]. Experimentally we used the ALLIN ultrasonic array system with a 64 element array to make laboratory inspection of copper blocks and copper canisters. Theoretically we had simulated ultrasonic fields radiated by linear arrays into immersed solids in both the time-harmonic and the transient case [1], and those radiated by phased arrays, tilt linear arrays, and concave arrays [2] in the time-harmonic case.

The present work is intended to fulfill the two tasks: development of beam-forming and modeling tools, and verification of modeling tools. Beam-forming is realized by ultrasonic array systems. The tools for beam-forming are intended for designing angle (steered) and/or focused beams that are best suitable for various situations encountered in inspection of copper canisters. The modeling tools are intended to simulate fields radiated by arrays into fluids and solids, and are verified theoretically and experimentally for some relevant cases.

In inspection of the regions close to canisters outer walls, steered beams are to be utilized and are supposed to be focused along the line directed at the steering angle. A method of designing such focused and steered beams in immersed solids is presented based on geometrical acoustics. To implement the beam-forming, relevant factors, like apodization, delays for the transmission and the reception of signals and their combination, need to be considered in designing beams suitable for desired inspection circumstances. Presently, the beam designs are only related to delays but not to apodization. Inspection of the regions close to canisters outer walls using steered beams will be presented in the following chapter.

The ALLIN array consists of rectangular elements which are linearly aligned in one (x) direction and cylindrically curved in the other (y) direction. Therefore, in the x-z plane the array can focus beams electronically, and the focal zone of a focused field can be positioned at specified depth by using a set of delay times obtained according to a certain focusing law; and in the y-z plane the array can focus beams geometrically, and the focal position is fixed.

In the previous work, the simulation of ultrasonic fields in fluids and in immersed solids were carried out based on the angular spectrum approach (ASA). The ASA is usually based on 2D spatial Fourier-transform. It is because the 2D spatial Fourier transform is implemented in a (x-y) plane so that the ASA is restricted to dealing with the radiation of *planar* sources [1,2]. Therefore, the elements of linear and phased arrays studied in the previous work [1,2] were assumed planar, and thus the ASA applied to the case. In [2] we studied a concave array, a curved source, whose elements were cylindrically aligned and curved in a (x-z) plane. For this type of array, the ASA does not apply directly. Since the ASA is a very good candidate for calculating the fields in immersed solids and

layered media, we developed a method that indirectly used the ASA to the curved transducers [2]. The method first calculated an initial field in a plane in front of the curved source by means of some other way which is not limited to the case of planar sources [3] and then considered the initial field as a secondary source that was planar. For the secondary source which is planar, the ASA applied, that is, from the initial field, we performed the 2D FFT and then obtained the angular spectrum of the initial field, which was equivalent to the curved source's angular spectrum at the position of the initial field. This method is here named indirect ASA. Although the indirect ASA is applicable to an arbitrarily shaped source and to the ALLIN array, the calculation of an initial field appeared to be very time-consuming even in the time-harmonic case. To reduce the computational time, we extend the ASA to directly solve the radiation of curved sources.

Fields radiated by the array of this type into fluids and immersed solids are investigated in the present work both theoretically and experimentally.

For precise measurement and simulation of fields from the array, the electronic and acoustic pulses and the delay times of the ALLIN system are first measured. The errors of delay times both for transmission and reception are then determined and analyzed from the measurements. The measured acoustic pulses and the true delay times are finally used as input to the array elements for the modeling of fields.

The acoustic fields radiated by the array into water are measured by using a point-like scatterer, and those in a copper block are done by using a set of side-drilled holes located at different depths in the block.

1.2 Development of beam-forming tools

To inspect the regions close to canisters outer walls, steered beams are to be employed that are supposed to be focused along the line directed at the desired angle. A method of designing such steered, focused beams in immersed solids is presented in this subsection. The method is based on geometrical acoustics.

Consider a phased array consisting of N' elements with size $2a \times 2b$ and spacing d, located in a fluid at plane $z = 0$ (Fig. 1.1). Here N' is assumed to be an even integer. Suppose the array performing beam steering by an angle α in a homogeneous fluid (e.g. water) and focused at point F on the beam axis. Now a solid is placed close to the array as shown in Fig. 1.1, the focal point of longitudinal wave (shear wave is not of present interest) in the solid will be blurred and shifted to a location F'. This is a well known refraction phenomenon which results in geometrical distortion of images in the solid. To reduce this geometrical distortion, we desire such a beam that is steered at angle α and still focused at point F as if there were no refraction at the interface. Such a solution is very desirable from the practical point of view as it can simplify imaging of targets detected in the immersed solid.

To obtain this steered, focused beam, we will take two steps to figure out the delays. Firstly, the beam is steered by angle α by applying the following delay time sequence to the voltage pulses to the array elements [2],

$$\tau_{si} = (i - 1/2)d \sin\alpha / c, \tag{1.1}$$

where i = -N'/2+1, ..., 0, 1, ... N'/2. The array that steers a beam by α is virtually rotated from the physical array by α and has the effective aperture length $A' = N'd\cos\alpha$ and the effective spacing $d' = d\cos\alpha$. This is shown in Fig. 1.2(a). In sequel, the virtually rotated array is called virtual array having the effective aperture length A' and the effective spacing d'. Secondly, we base ourselves on this virtual array, set the focal point at position F, and calculate the delay times for the focus, τ_{fi}. The delay time τ_{fi} for the ith element of the *virtual array* is calculated based on geometrical acoustics in such a way that all acoustic pulses coming from the centers of the elements should simultaneously arrive at the desired focal position (see Fig. 1.2(b)).

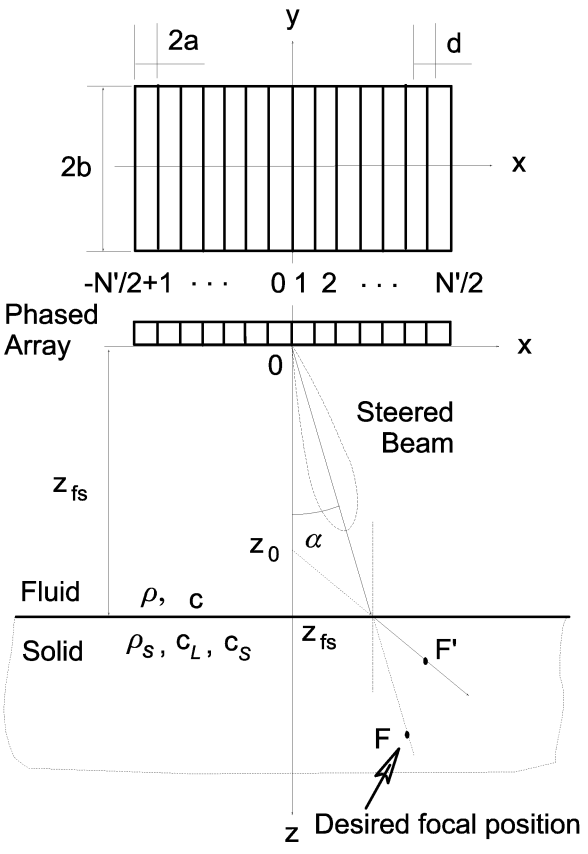

Fig. 1.1. Geometry of the phased array generating a steered, focused beam in a solid.

Referring to Fig. 1.2(b), we assume that the distance from the virtual array's center to the fluid/solid interface is H_w and the distance from the fluid/solid interface to the focal point is H_s. The focal length is $H'_w + H'_s$, where $H'_w = H_w / \cos\alpha$ and $H'_s = H_s / \cos\alpha$. The path of an acoustic ray propagating from the point on the array surface to the focal point F is unique and bent at the

fluid/solid interface. The path length of the ray is assumed to be L_{wx} in fluid and L_{sx} in the immersed solid. At the leftmost end of the virtual array, L_{wx} and L_{sx} become L_{wl} and L_{sl}, respectively, and at the rightmost end, L_{wx} and L_{sx} becomes L_{wr} and L_{sr}, respectively. The incident and refractive angle of the ray must meet the Snell law, i.e., $\sin\theta_{wx}/C_w = \sin\theta_{sx}/C_s$.

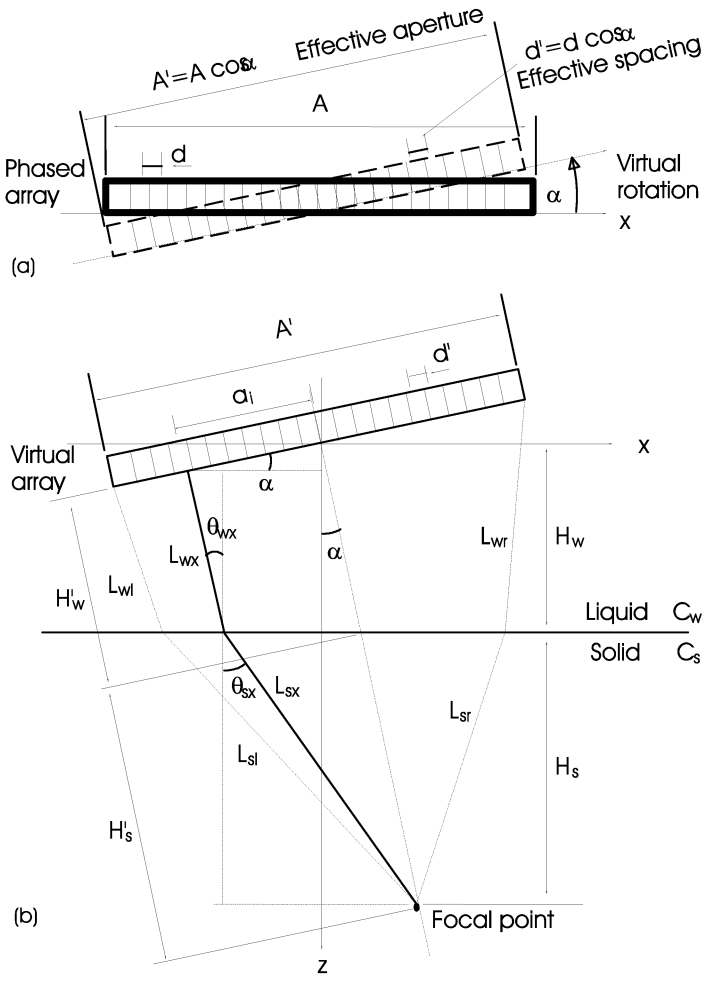

Fig. 1.2. Geometry and notation for the calculation of delays used for the phased array to steer and focus a beam in an immersed solid.

From the condition that all acoustic pulses coming from the centers of the virtual array elements should simultaneously arrive at the desired focal position, we get,

$$\tau_{fi} + \frac{L_{wx}}{C_w} + \frac{L_{sx}}{C_s} = T_c, \tag{1.2}$$

where T_c is constant. From Fig. 1.2(b), we can easily find

$$L_{wx} = (H_w - a_i \cos\alpha)/\cos\theta_{wx}\ , \tag{1.3a}$$

$$L_{sx} = H_s/\cos\theta_{sx}\ , \tag{1.3b}$$

where a_i is the distance of the point off the center of the array (see Fig. 1.2(a)).

In the case shown in Fig. 1.2, the time of flight of the ray emitting by the element on the rightmost end of the array is the longest, and thus we can let the constant T_c to be

$$T_c = \frac{L_{wr}}{C_w} + \frac{L_{sr}}{C_s}. \tag{1.4}$$

Inserting Eq. (1.4) into Eq. (1.2), we have

$$\tau_{fi} = \frac{L_{wr} - L_{wx}}{C_w} + \frac{L_{sr} - L_{sx}}{C_s} = \frac{1}{C_w}\left(\frac{H_w - A'\cos\alpha/2}{\cos\theta_{wr}} - \frac{H_w - a_i\cos\alpha}{\cos\theta_{wx}}\right) + \frac{H_s}{C_s}\left(\frac{1}{\cos\theta_{sr}} - \frac{1}{\cos\theta_{sx}}\right). \tag{1.5}$$

Combining Eq. (1.2) and (1.5), we still can not determine the delays for focusing because determining both θ_{wx} and θ_{ws} we need one more condition. From Fig. 1.2(b), we can find another equation, which relates a_i with the position of the focal point in the following manner,

$$a_i\cos\alpha = (H_w - a_i\sin\alpha)\tan\theta_{wx} + H_s\tan\theta_{sx} - (H_w + H_s)\tan\alpha, \tag{1.6a}$$

or

$$\tan\theta_{sx} = \frac{a_i(\cos\alpha + \sin\alpha\tan\theta_{wx}) - H_w\tan\theta_{wx} + (H_w + H_s)\tan\alpha}{H_s}. \tag{1.6b}$$

In combination of Eqs. (1.2) and (1.6), we can solve out θ_{wx} and θ_{sx}, and further, figure out the delays for focus, τ_{fi}, in Eq. (1.5). Finally, the total delay times τ_i applied to the *i*th element of the array (not the virtual array!) for both steering and focusing the desired beam is obtained simply by summing the delay times for steering and focusing, i.e.,

$$\tau_i = \tau_{si} + \tau_{fi}. \tag{1.7}$$

It should be pointed out that the delays obtained form Eq. (1.7) may be negative or all greater than zero. In practice, however, the delays usually should be all positive. Thus in the following application all the delays shall be subtracted by their minimal value so that they become equal to or greater than zeros. Obviously, the focusing law determined by Eq. (1.5) in the immersion case is no longer cylindrical as in the case of a homogeneous medium, and the focusing is called optimal focusing. Below we present several examples of steered, focused beams. The phased array used for generating these beams has the following parameters: N' = 64, d = 0.5 mm, $2a$ = 0.5 mm, and $2b$ = 12 mm. The sound speeds used for calculations are c = 1500 *m/s* in water, and c_l = 4660 m/s (longitudinal wave) in copper, respectively. Thus, c_l/c = 3.1. The water layer is 30 mm thick, and the focal point is located at 60 mm from beneath the interface, i.e., H_w =30 mm and H_s =60 mm. The beams steered by α= 0° ,

1° 3° , and 5° , respectively. When the phased array radiates the beams into water without the solid in it, the focusing is cylindrical and the focal point is equivalently located at z = 30 mm + 186.4 mm, where 186.4 mm = (60 mm)$\times$(c_l/c). The delays for optimal focusing (solid curves) and cylindrical focusing (dotted curves) are comparatively in Fig. 1.3.

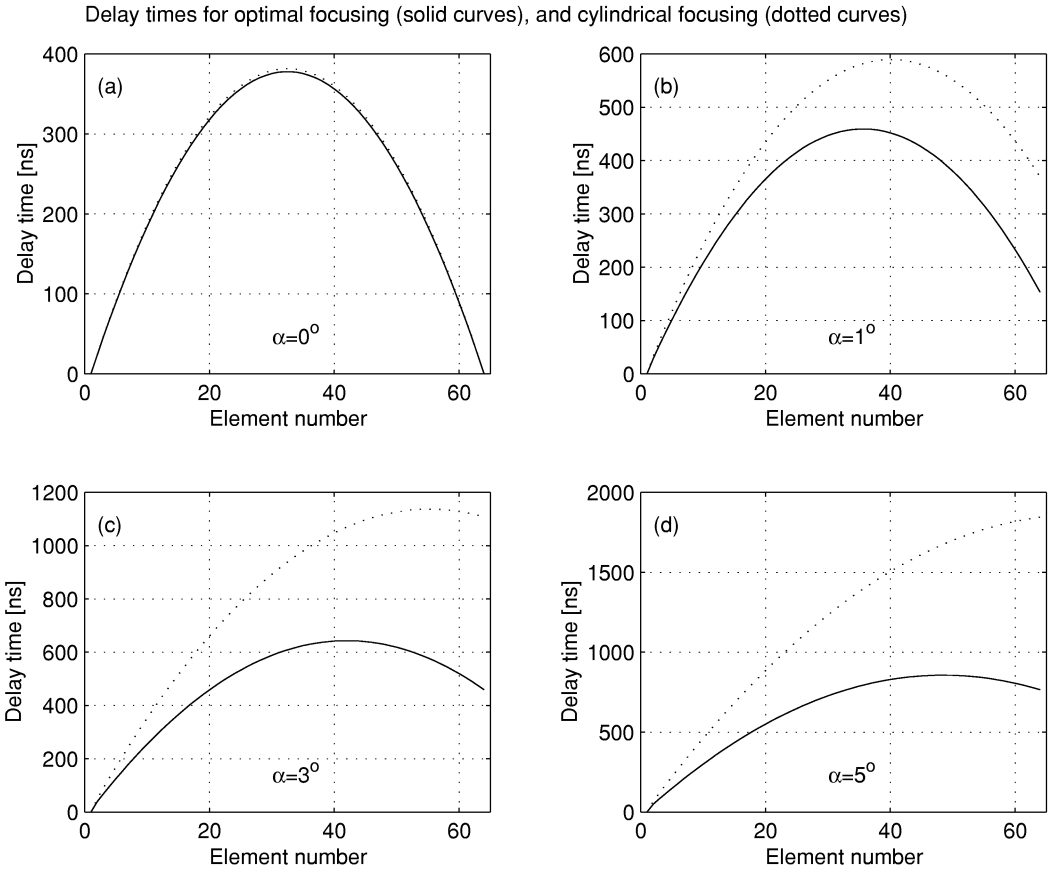

Fig. 1.3. Delays used for generating steered beams being optimal focused in copper immersed in water (solid curves) and comparison with those for cylindrically focused beams in water (dotted curves). The beams are steered by (a) $\alpha = 0^\circ$, (b) $\alpha = 1^\circ$, (c) $\alpha = 3^\circ$, and (d) $\alpha = 5^\circ$, respectively.

From Fig. 1.3, we can see that in the normal incident case ($\alpha = 0^\circ$) both types of focusing are very close, and when the beams are steered, the larger the steering angle α the more they differ. We can conclude that in the normal incident case the cylindrical focusing is a good approximation of the optimal focusing, otherwise not.

1.3 Development and verification of modeling tools

1.3.1 Verification of the modeling tool for simulating elastic fields from planar arrays

A modeling tool for simulating ultrasonic transient fields radiated by planar linear arrays was developed almost two years ago. The fields can be acoustic ones in fluids and elastic ones in immersed solids [1]. The tool was based on the ASA and verified in the case of acoustic fields by comparison with the spatial impulse response method [1]. But the verification in the case of elastic fields had not been done yet at that time. Recently, we verified the modeling tool by comparing with PASS, a commercial PC software developed by Dr. D. Cassereau in Laboratoire Ondes et Acoustique, Universite Paris VII, France, and distributed by R/D Tech, Canada. The PASS is based on the ray-tracing method. The two tools are both implemented on PC and both are efficient in computation.

The calculations made by the two modeling tools were based on the following specifications of the array, the pulse excitation of normal velocity, and numerical parameters. The calculated results are given in terms of particle velocity with *x*-, *y*- and *z*-components.

The linear array used in the simulation consisted of 32 planar and rectangular elements separated with d=1 mm (refer to Fig. 1.1). The dimension of the elements is $2a \times 2b$=1mm × 22mm, which implies no gap between the adjacent elements. The array was positioned in the *x*-*y* plane at z = 0 and centers at the origin of the coordinates. The solid medium in which the fields were simulated is a copper block with a flat surface immersed in water. The physical parameters of the copper block are $\rho_s = 8960$ kg/m^3, c_l = 4660 m/s and c_t = 2260 m/s, and those assumed for water are $\rho = 1000$ kg/m^3 and c = 1500 m/s and the thickness of water layer is 20 mm.

The pulse excitation of the normal velocity on each array element without time-delay is taken as a sinusoidal modulated signal with Rayleigh-shaped envelope, i.e., $v(t) = A_e t e^{-B_e t^2} \sin\left(2\pi f_0 t + C_e\right)$ (for $t \geq 0$). The values of the parameters in $v(t)$ used in the paper are the central frequency f_0 = 3 MHz, B_e = 10, $C_e = 3\pi/4$ and $A_e = 1/\max[|te^{-B_e t^2} \sin(2\pi f_0 t + C_e)|]$. The temporal sampling frequency is 76.8 MHz and the frequency range used covers from 0 to 10 MHz, which is accurate enough to represent the spectrum of $v(t)$. Note that the magnitude of $v(t)$ is the envelope function $A_e t e^{-B_e t^2}$, whose peak value is larger than unity in the present case.

The results calculated by our modeling tool (solid curves) and PASS (dotted curves) are comparatively shown in Figs. 1.4 and 1.5. Fig. 1.4 shows the *z*-components of particle velocity on the axis (x = 0, y = 0). The *x*- and *y*-components in this on-axis case are zeros due to the symmetry of the source with respect to the *x* and *y* axes. Fig. 1.5(a)-(f) shows the *z*-components of particle velocity off the axis (x = 0, y = 0), and Fig. 1.5(a')-(f') shows the *x*-components of particle velocity off the axis (x = 0, y = 0). The *y*-components in this off-axis case are zeros due to the symmetry of the source with respect to the *y* axes. Note that the scale used in Fig. 1.5(a')-(f') is ten times smaller than the one used in Fig. 1.5(a)-(f). This means that the *x*-components are much smaller than the *z*-components.

From the comparison in the figures we can see that very close to the interface, the results from two modeling tools are slightly different (c.f. Figs. 1.4(a), 1.5(a), and 1.5(a') in which z = 21 mm, and 1.5(b') in which z = 52 mm), and farther away from the interface, the respective results (c.f. the remaining results) are almost in perfect agreement.

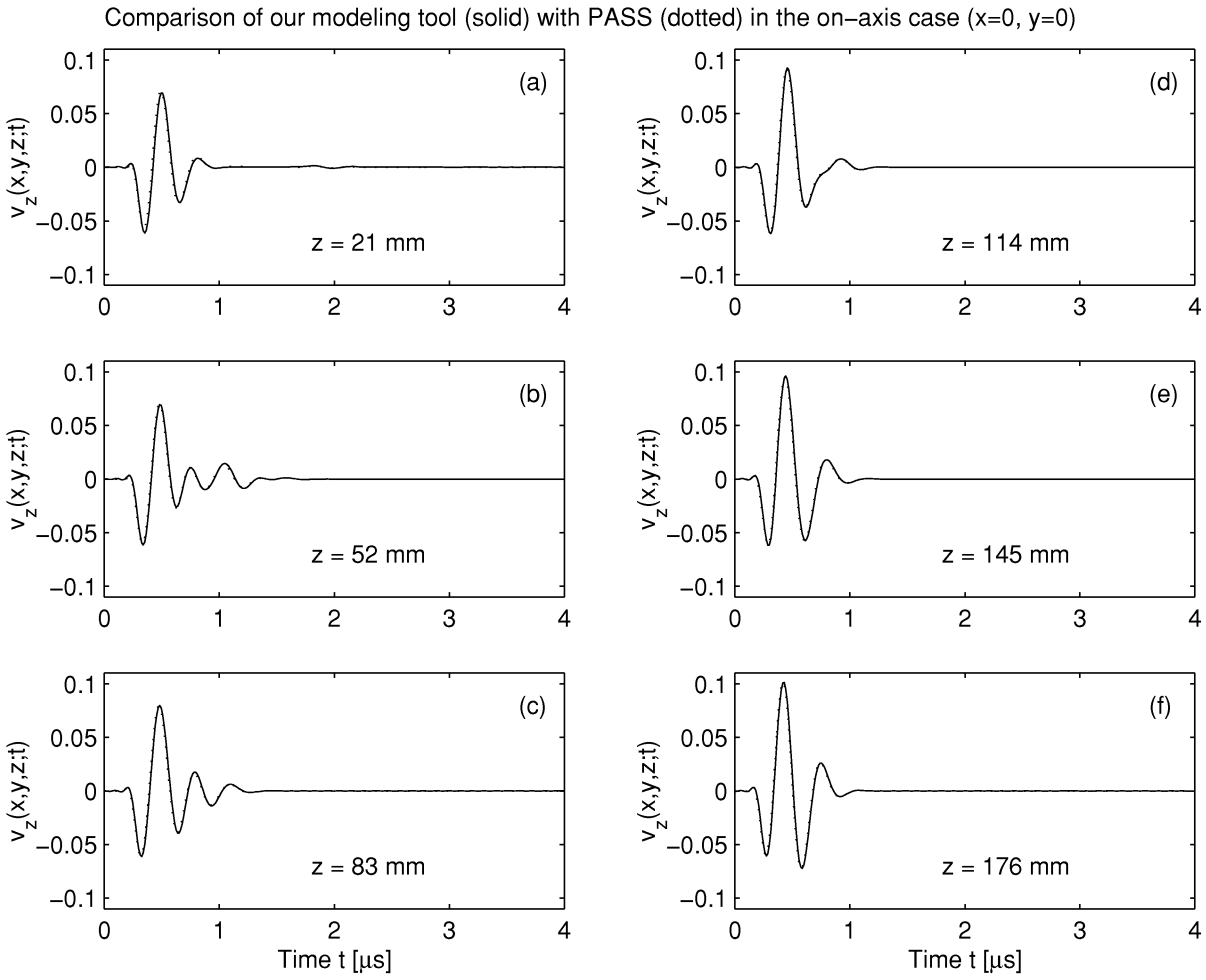

Fig. 1.4. *z*-component of particle velocity on the axis (x=0, y=0) at (a) *z* = 21 mm, (b) *z* = 52 mm, (c) *z* = 83 mm, (d) *z* = 114 mm, (e) *z* = 145 mm, and (f) *z* = 176 mm, respectively.

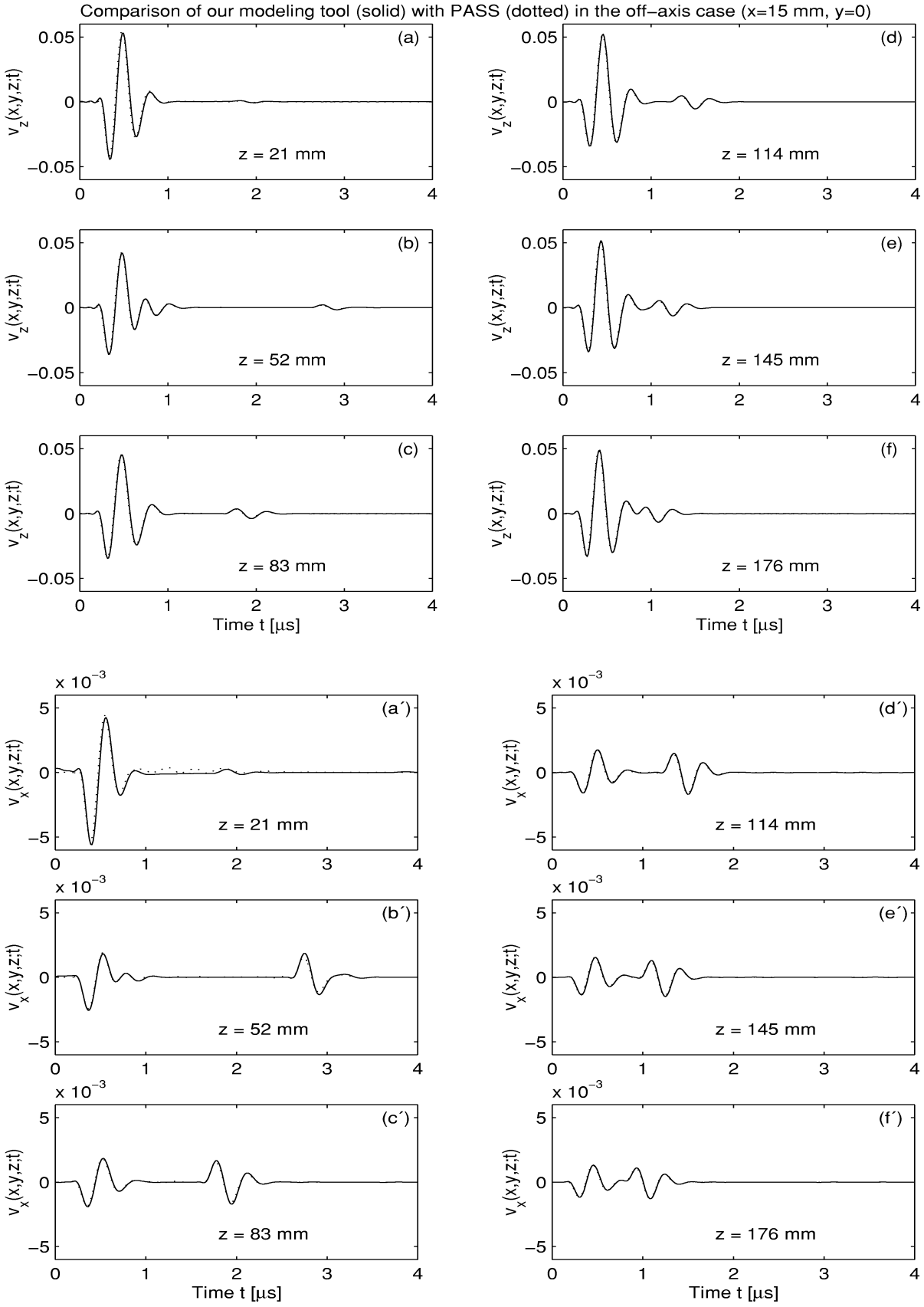

Fig. 1.5. *z*- and *y*-component of particle velocity off the axis (*x*=15mm, *y*=0) at (a) & (a') *z* = 21mm, (b) & (b') *z* = 52mm, (c) & (c') *z* = 83mm, (d) & (d') *z* = 114mm, (e) & (e') *z* = 145mm, and (f) & (f') *z* = 176mm, respectively.

1.3.2 Development and verification of the modeling tool for simulating focused acoustic fields from curved arrays

Focused ultrasonic fields are commonly used in NDT and medical imaging because they yield better spatial resolution and enhance the system's signal-to-noise ratio. A focused ultrasonic field can be achieved by an array performing electronic focusing [1-3,5] and by a curved source [6-25] or a planar source with a lens attached in front [26-38] performing geometrical focusing. The electronic focusing by arrays has been dealt with in details in our previous work [1,2]. In the present work, we will study fields geometrically focused by curved sources.

Various methods of calculating geometrically focused fields can be found in literature [2, 5-25, 30-38]. However, most of the previous researches were concentrated on acoustical fields focused by spherically focusing transducers that were axisymmetrical. The considered fields were axisymmetrical and easily handled compared to the non-axisymmetrical case like the ALLIN array we have been using. Arrays with cylindrically curved face or with cylindrical lens have been commonly used in NDT and medical imaging. Nevertheless, the focused elastic fields in the solids from such arrays have seldom been analyzed theoretically although focused fields from geometrically focusing transducers have been employed in NDT of solid materials for a long time.

As has been mentioned in Sec. 1.1, we developed a method for calculating elastic fields radiated by concave arrays into immersed solids [2], which is applicable to the ALLIN array after introducing small modification. However, this method requires calculating an initial field, which is very time-consuming before the ASA is applied. To save computational time, we will get rid of the intermediate step - the calculation of an initial field, and extend the ASA to directly solve the radiation of curved sources.

1.3.2.1 General consideration

A curved transducer having a rigid baffle and radiating acoustic fields into lossless fluids is considered here. It is well known that a sound field from a baffled planar piston source in a fluid can be rigorously depicted by the Rayleigh integral [39]. For a curved source the Rayleigh integral can approximately represent the radiation of the curved source under certain conditions [7-10]. Following O'Neil [19], the velocity potential can be approximately expressed by the Rayleigh integral if the normal velocity of the source on the curved surface S is represented by $\tilde{v}_n(\mathbf{r})$ at frequency ω,

$$\phi(\mathbf{r}) = -\frac{1}{2\pi}\iint_S \tilde{v}_n(\mathbf{r}')\frac{\exp(jkr_s)}{r_s}dS \tag{1.8}$$

where $r_s = |\mathbf{r} - \mathbf{r}'|$ is the distance from source point $\mathbf{r}'$ on surface S to field point $\mathbf{r}$ in the medium. Eq. (1.8) treats each surface element dS as a point source of strictly hemispherical waves, and in the

limiting case where S is a plane radiator with an infinite baffled plane, the equation is rigorously correct. If S is curved, waves radiated from any part of the curved surface are diffracted by other parts of this surface, but the integral in Eq. (1.8) neglects this fact. When the surface S is only slightly curved, this secondary diffraction becomes relatively unimportant [7]. The resultant effects due to the secondary disturbances which originate at different parts of S will be further reduced by phase differences if the extent of S is large relative to the wave length. Also, with this restriction on the dimension, most of the energy will be radiated in a central beam, which will be affected very little by the presence or the absence of a baffle around the radiator. Hence, if the diameter or breadth of a slightly curved source surface S is large compared with the wavelength, the velocity potential at points in or near the main beam will be represented approximately by the integral in Eq. (1.8). This is often called O'Neil theory that has been proven to be a good basis for evaluating focused transducers [9, 10, 16, 25, 12, 13, 15]. From the relation of pressure with velocity potential, $\tilde{p}(r) = -\rho\,\partial\phi(r)/\partial t = jk\rho c\phi(r)$ where ρ is the density, c is the sound velocity, and $k = \omega/c$ is the wave number, one obtains the Rayleigh integral in terms of pressure in the following manner,

$$\tilde{p}(\mathbf{r}) = -\frac{jk\rho c}{2\pi}\iint_S \tilde{v}_n(\mathbf{r}')\frac{\exp(jkr_s)}{r_s}dS\,. \tag{1.9}$$

Two angular spectrum approaches, the extended ASA and the indirect ASA, are derived from this Rayleigh integral.

Consider a source with surface S that is represented by $z = f(x,y)$ under the Cartesian coordinates. Assuming that $z = f(x,y)$ is continuous and has the first order derivatives, the elementary surface dS can be expressed by $dS = dx'dy'/\cos\theta_z$, where $\cos\theta_z$ is the direction cosine of the normal with respect to the z-axis. $\cos\theta_z$ can be obtained from

$$\cos\theta_z = \frac{1}{\sqrt{\left(f_x(x,y)\right)^2 + \left(f_y(x,y)\right)^2 + 1}}, \tag{1.10}$$

where $f_x(x,y)$ and $f_y(x,y)$ are the partial derivatives with respect to x and y, respectively. From Eqs. (1.9) and (1.10), the pressure in the Cartesian coordinates can be easily derived as

$$\begin{aligned}\tilde{p}(x,y,z) &= -\frac{jk\rho c}{2\pi}\iint_{S_{xy}} \tilde{v}_n\left(x',y',f(x',y')\right)\frac{\exp(jkr_s)}{r_s}\frac{dx'dy'}{\cos\theta_z} \\ &= -\frac{jk\rho c}{2\pi}\iint_{S_{xy}} \tilde{v}_z\left(x',y',f(x',y')\right)\frac{\exp(jkr_s)}{r_s}dx'dy',\end{aligned} \tag{1.11}$$

where S_{xy} is the area of the projection of the surface S onto the x-y plane, $\tilde{v}_z = \tilde{v}_n/\cos\theta_z$, and $r_s = \sqrt{(x-x')^2 + (y-y')^2 + \left[z - f(x',y')\right]^2}$.

In the case of a planar piston source, its angular spectrum can be obtained by applying the convolution theorem to the Rayleigh integral [41] and it is given by a 2-D spatial Fourier transform of the normal velocity on the source surface [40]. For a planar piston source located in the $z=z_0$ plane, its angular spectrum is denoted by $V(k_x,k_y;z=z_0)$. For an acoustic field from the planar source propagating forward in the +z direction to a plane at $z_1(\geq z_0)$, the angular spectrum of the field can be derived from the relation [41]

$$V(k_x,k_y;z=z_1)=V(k_x,k_y;z=z_0)\exp\left(j(z_1-z_0)k_z\right), \tag{1.12}$$

where $k_x=kn_x$, $k_y=kn_y$, $k_z=\sqrt{k^2-k_x^2-k_y^2}=k\sqrt{1-n_x^2-n_y^2}$ are the spatial frequencies in the x-, y- and z-directions in the medium, respectively. However, the above relation does not apply to a curved source. Now we divide the surface S of the curved source into a set of such small elementary sources with surface δS that each of them can be approximated by a plane. Then we obtain the angular spectrum of the whole source by the superposition of the angular spectra of elementary sources. Supposing that δS_{xy} is the projection of δS onto the x-y plane, the angular spectrum of the small elementary source on surface S at (x', y', z') where $z'=f(x',y')$ can be approximated by

$$\delta V(k_x,k_y;z')=\iint_{\delta S_{xy}}\tilde{v}_z\left(x',y',z'\right)\exp\left[-j(x'k_x+y'k_y)\right]dx'dy'\approx\tilde{v}_z\left(x',y',z'\right)\exp\left[-j(x'k_x+y'k_y)\right]\delta S_{xy}.$$

Thus, at the plane $z=z_1$ ($\geq\max[f(x',y')]$) the angular spectrum of the whole source can be obtained from superposition of the spectra of all elementary sources in the following manner,

$$\begin{aligned}V(k_x,k_y;z=z_1)&=\lim_{\delta S_{xy}\to 0}\sum_{S_{xy}}\delta V(k_x,k_y;z')\exp\left(j(z_1-z')k_z\right)\\&=\iint_{S_{xy}}\tilde{v}_z\left(x',y',f(x',y')\right)\exp\left[-j(x'k_x+y'k_y)\right]\exp\left[j\left(z_1-f(x',y')\right)k_z\right]dx'dy'\end{aligned} \tag{1.13}$$

where the condition $z_1\geq\max[f(x',y')]$ must be met in order to ensure that $V(k_x,k_y;z=z_1)$ is always finite for all k_x and k_y. Eq. (1.13) is the final form for the angular spectrum of a curved source and is derived, based on the Rayleigh integral of curved surface (the O'Neil's theory) and the ASA in the case of planar sources, without any approximation. Obviously, the angular spectrum of the curved source is not of the form of the 2-D spatial Fourier transform. Since $k_z=\sqrt{k^2-k_x^2-k_y^2}=k\sqrt{1-n_x^2-n_y^2}$, evanescent waves show up when $k_x^2+k_y^2>k^2$ or $n_x^2+n_y^2>1$. When z_1 is chosen to be so large that $z_1\geq\max[f(x',y')]$ plus a few wavelengths, e.g., $z_1\geq\max[f(x',y')]+2\lambda$, the evanescent waves are strongly attenuated and thus can be neglected without loss of accuracy [40]. Therefore, $V(k_x,k_y;z=z_1)$ in the range of $k_x^2+k_y^2\leq k^2$ is usually used for synthesizing the acoustic field. In general, the double integral in Eq. (1.13) is very difficult to directly solve. But in some special cases, the integral can be simplified to a significant extent. One of the cases is linear arrays with cylindrically curved surfaces, which will be studied in the following section.

1.3.2.2 Fields from an array with a cylindrically concave surface

The ultrasonic array that we have used for the inspection of copper canisters is illustrated in Fig. 1.6. It has a cylindrical concave surface performing geometrical focusing in the *y*-*z* plane. Calculation of the fields from this type of array is presented in this section.

Referring to Fig. 1.6, we assume that the array has *N'* elements and its surface is cylindrically concave and expressed by the following equation,

$$y^2 + (z-R)^2 = R^2, \text{ or } z = R - \sqrt{R^2 - y^2}, \qquad \{x_i - a \le x \le x_i + a, \quad -b \le y \le b\} \tag{1.14}$$

where R is the radius of the curvature, $2a$ and $2b$ define the width and length of each element, respectively, $x_i = (i - 1/2)d$ is the position of the center of the ith element on the x axis, i = -N'/2+1, ..., 0, 1, 2, ... N'/2, and $z = e$ for $y = \pm b$. The direction cosine of the normal of the array surface with respect to the z-axis is

$$\cos\theta_z = \sqrt{R^2 - y^2} \Big/ R. \tag{1.15}$$

Consider the array with all the elements having uniform normal velocity distribution on the surface. For the ith element, the normal velocity excitation at frequency ω is supposed to be

$$\tilde{v}_{ni}(x, y, z; \omega) = \tilde{v}_i(\omega) \exp(j\omega\tau_i), \tag{1.16}$$

where $\tilde{v}_i$ is the complex amplitude; and τ_i is the delay time, which, in the time-harmonic case, creates phase shift $\omega\tau_i$ for beam steering and focusing [2].

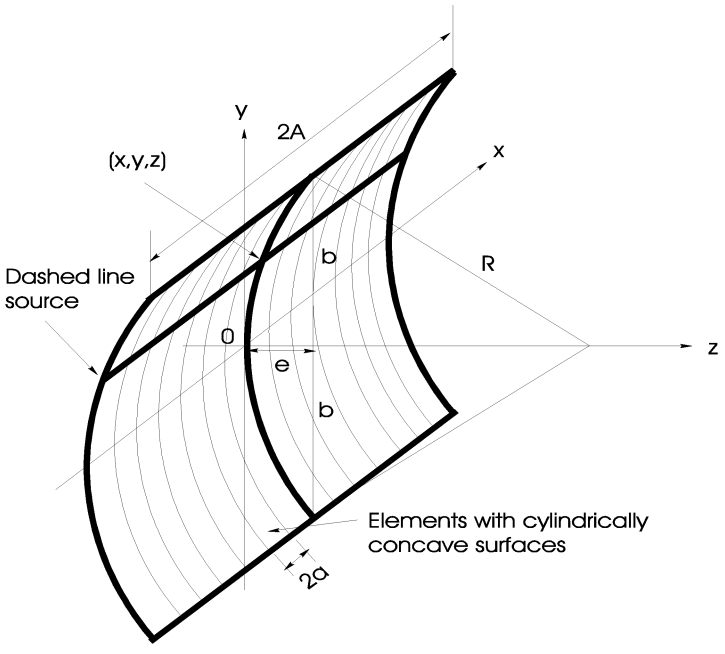

Fig. 1.6. Geometry and notation of the array with cylindrically concave surface.

Inserting Eqs. (1.14) - (1.16) into Eq. (1.13), we obtain the angular spectrum for the *i*th element of the array centering at $(x,\ y,\ z)=\{(i\text{-}1/2)d,0,0\}$ $\left\{(i-1/2)d-a\le x\le(i-1/2)d+a,\ \ -b\le y\le b\right\}$ in the following manner,

$$V_i(k_x,k_y;z=z_1)=\tilde{v}_i(\omega)\exp(j\omega\tau_i)\int_{(i-1/2)d-a}^{(i-1/2)d+a}\exp(-jxk_x)dx\int_{-b}^{b}\frac{\exp\left[-j\left(yk_y+(R-\sqrt{R^2-y^2}-z_1)k_z\right)\right]}{\sqrt{R^2-y^2}/R}dy$$

$$=\tilde{v}_i(\omega)\exp\left[j\omega\tau_i-j(i-1/2)dk_x\right]2a\,\mathrm{sinc}(ak_x)\int_0^b\frac{2R\cos(yk_y)\exp\left(j(z_1-R+\sqrt{R^2-y^2})k_z\right)}{\sqrt{R^2-y^2}}dy\,.$$

$$(z_1\ge e)\qquad(1.17)$$

Usually, $R>>b$ (e.g., R=190 mm, b=16.75 mm [3]), and thus $R>>y$. Using the Taylor series expansion, we have $R-\sqrt{R^2-y^2}\approx y^2/(2R)$. That is the cylindrically concave surface $z=\ R-\sqrt{R^2-y^2}$ is approximated by a parabolic cylinder $z=\ y^2/(2R)$. Therefore, Eq. (1.17) can reduce to

$$V_i(k_x,k_y;z=z_1)=\tilde{v}_i(\omega)\exp\left[j\omega\tau_i-j(i-1/2)dk_x\right]2a\,\mathrm{sinc}(ak_x)\int_0^b\frac{2R\cos(yk_y)\exp\left[jk_z\left(z_1-y^2/(2R)\right)\right]}{\sqrt{R^2-y^2}}dy\,,$$

$$(z_1\ge e)\qquad(1.17a)$$

From the angular spectrum in Eq. (1.17), we can obtain the angular spectrum of the array as follows,

$$V(k_x,k_y;z=z_1)=\sum_{i=-N'/2+1}^{N'/2}V_i(k_x,k_y;z=z_1)\,.\qquad(1.18)$$

Furthermore, the pressure field from the array can be synthesized from the angular spectrum of plane waves in Eq. (1.18),

$$\tilde{p}(x,y,z)=k\rho c\int_{-\infty}^{\infty}\int_{-\infty}^{\infty}V\left(k_x,k_y,z=z_1\right)\frac{\exp\left[j\left(xk_x+yk_y+(z-z_1)k_z\right)\right]}{k_z}dk_xdk_y\ ,\ (z\ge z_1).\qquad(1.19)$$

In the transient case, the pulse normal velocity of the *i*th element is represented by $v_{ni}(x,y,z;t)$ and its temporal Fourier transform is $\tilde{v}_{ni}(x,y,z;\omega)$ which are of the same form as in Eq. (1.16). The transient pressure field can, thus, be obtained by the inverse Fourier transform, that is, $p(x,y,z;t)=(1/2\pi)\int_{-\infty}^{\infty}\tilde{p}(x,y,z)\exp(-j\omega t)d\omega$.

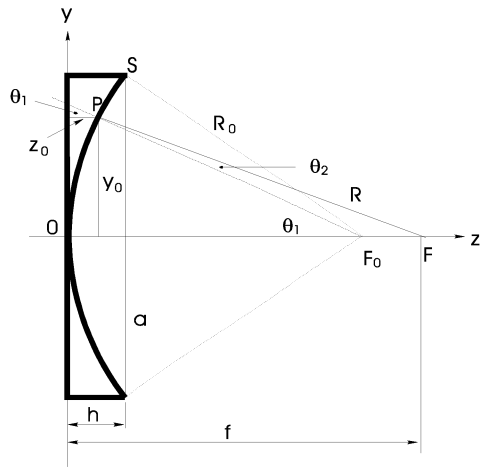

Fig. 1.7. Geometry and notation of the array with plano-concave lens.

A planar array with a plano-concave lens is also commonly used. Treatment of this type of array is similar to a cylindrically concave array. Here we give a brief presentation. A plano-concave lens is assumed to have radius R and sound speed c_h (see Fig. 1.7), and the lens can be seen as a spatial delay device. The angular spectrum can be obtained with the same procedure,

$$V(k_x, k_y; z = z_1) = \iint_S \tilde{v}_z\big(x, y, f(x,y)\big) \exp\big[-j(xk_x + yk_y)\big] \exp\Big[j\big(z_1 - f(x,y)k_{zh}\big)\Big] dxdy \,, \tag{1.20}$$

where $k_{zh} = k_z(c/c_h)$.

Elastic fields in immersed solids from the array in Fig. 1.6 can be calculated based on Eq. (1.13) using the procedure presented in [2].

1.3.2.3 The difference between the cylindrically concave surface and the parabolic surface

In the sake of simplification, the cylindrically concave surface $z= R-\sqrt{R^2-y^2}$ was approximated by the parabolic cylinder $z= y^2/(2R)$ in Eq. (1.17a). Now we shall evaluate the approximation. Take as an example the array that we have used in our experiments. It has a cylindrically concave surface with the radius of curvature R = 190 mm and the length of $2b$= 33.5 mm [2]. The difference between $z= R-\sqrt{R^2-y^2}$ and $z= y^2/(2R)$ is shown in Fig. 1.8, where Err = $\left(R-\sqrt{R^2-y^2} - y^2/(2R)\right)\Big/\left(R-\sqrt{R^2-y^2}\right)$ (%) and Err = 0 is defined for y = 0. The figure shows that the difference is very small, less than 0.2%, over the whole range of y = {-b, b}. Therefore, the cylindrically concave surface can be very well approximated by the parabolic cylinder in our case.

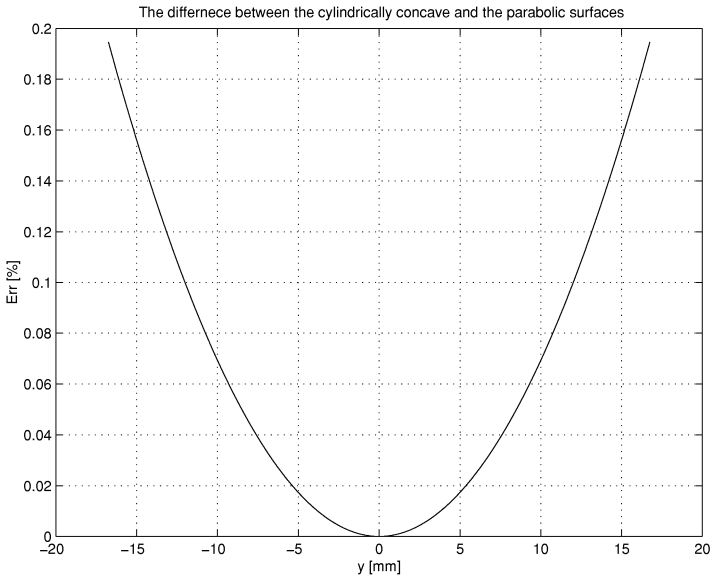

Fig. 1.8. Comparison of the cylindrically concave surface and the parabolic cylinder for R=190mm, and $2b$=33.5 mm.

1.3.2.4 Comparison of the angular spectra from the extended ASA and the indirect ASA

In Sec. 1.3.2.2, we have established the extended ASA with some approximation, and in Sec. 1.3.2.3, we have shown that the approximation only induces a very small error for gently focused arrays. In this section, we will verify the extended ASA by comparing the results obtained from the extended ASA with those obtained from the indirect ASA developed in [2].

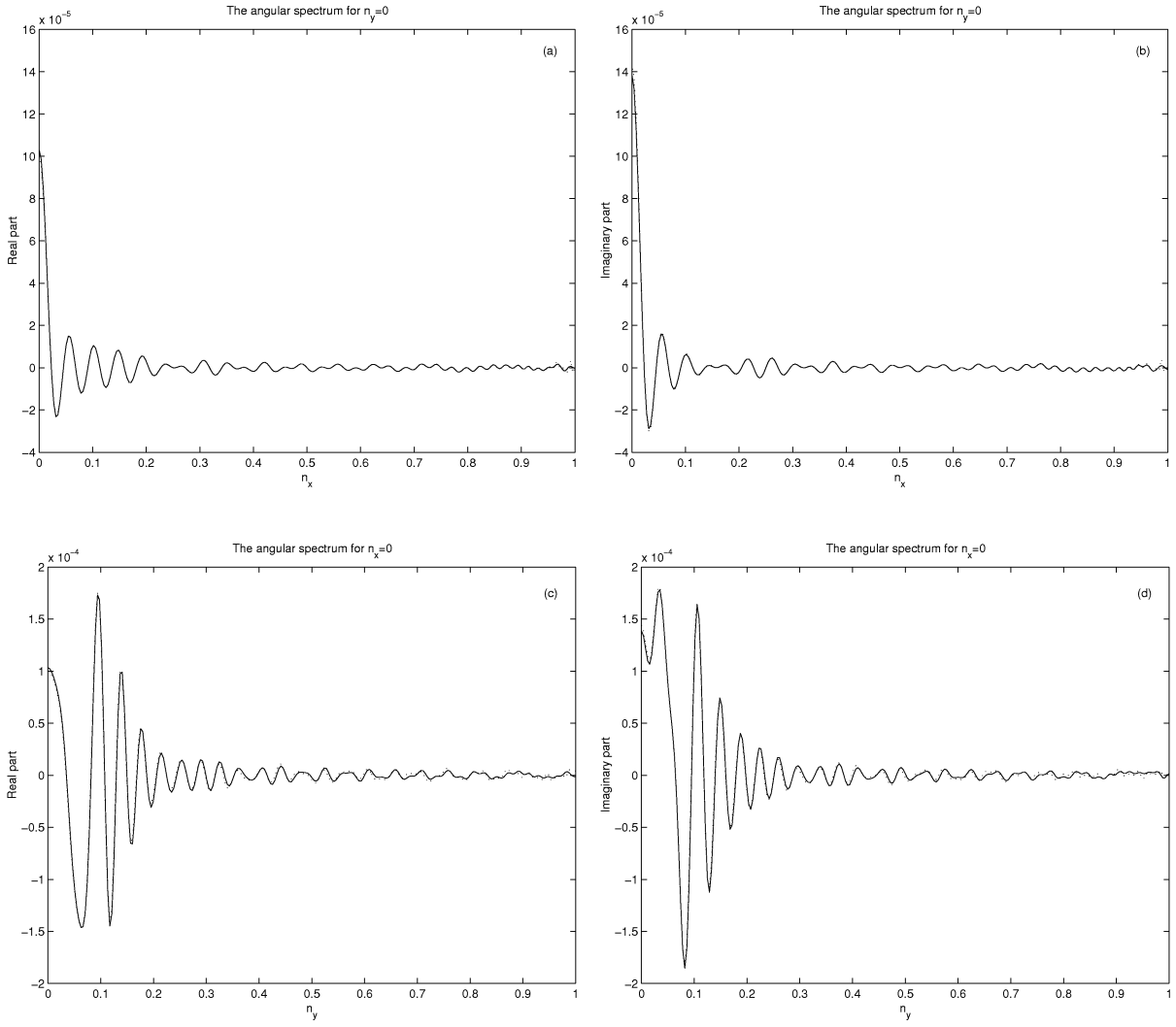

Fig. 1.9. Comparison of the angular spectra from the extended ASA (dotted line) and the indirect ASA (solid line). (a) The real and (b) the imaginary part on the *x*-axis; (c) the real and (d) the imaginary part on the *y*-axis.

In [2], we calculated an initial field from a concave array which is equivalent to the array shown in Fig. 1.6 with $2A$ = 22 mm, $2b$ = 30 mm and R = 100 mm, and has no gaps between the adjacent elements. The initial field (see Fig. 3.19 in [2]) was calculated in the plane at $z = e$ + 5mm, where $e = R - \sqrt{R^2 - b^2}$ = 1.13 mm. Based on the initial field and performing the 2D spatial FFT, we obtain the angular spectrum of the array in the plane at $z = e$ + 5mm. From the extended ASA, we use Eqs. (1.17a) and (1.18) to obtain the angular spectrum for $z_1 = e$ + 5mm. The results of the angular spectrum on the n_x - and n_y -axes from the indirect ASA (solid curves) and the extended ASA (dotted

curves) are compared in Fig. 1.9. The comparison shows that the results from the two methods are in a excellent agreement.

From this comparison it is concluded that the ASA can be extended to directly solve the fields from curved sources based on Eq. (1.13). In the case of a linear array with a cylindrically concave surface, Eq. (1.13) reduces to Eq. (1.17), or to Eq. (1.17a) when the parabolic approximation is introduced.

1.3.2.5 Calibration of the ALLIN ultrasonic array system

A focused and/or steered field generated by an array system is determined by different factors which are dependent on the array geometry and design, and on the electronic system. When the array geometry and design are given, the main factors mostly affecting the field are pulse excitations (shape and amplitude), transmission and reception delays applied to the array elements, and the excitations' uniformity. For example, delay errors may cause the focal zone of a focused field to deviate from the specified position, or a steered field to deviate from the specified direction. Therefore, these main factors should be examined and calibrated in order to generate a desired field. In this section, we present the measurements and calibration of the ALLIN system.

A. Specification of the array [3]

The array coming with the ultrasonic array system ALLIN consists of 64 strip-like elements, linearly-aligned in the x-direction and cylindrically curved in y-direction with the radius of curvature of 190 mm (see Fig. 1.6). Therefore, in the x-z plane the array can focus beams electronically, and the focal zone of a focused field can be positioned at specified depth by using a set of delay times obtained according to a certain focusing law; and in the y-z plane the array can focus beams geometrically, and the focal position is fixed around 190 mm away from the array because the radius of curvature is 190 mm [3]. The spacing between the centers of the adjacent elements is 1 mm, and the gap between the adjacent elements is 0.1 mm. This means that the width of each element is $2a$=0.9 mm. The length of each element is $2b$ = 33.5 mm. The nominal frequency is 3 MHz.

B. Electrical pulse excitations and transmission time delays of the ALLIN system

Electrical pulse excitations

The pulse excitations to the array were measured by means of TEKTRONIX digital real time oscilloscope TDS 210. The electric pulses from the ALLN system acquired at the first element of the array are shown in Fig. 1.10, where (a) and (b) are the pulses when the ALLIN output is disconnected and connected with the array, respectively. The pulses are negative spikes. A comparison of (a) and (b) shows that the pulse spike becomes smaller in amplitude and much wider in width when the array is connected. The measurements of the pulse excitations to other array elements have shown that the pulse to each array element is somewhat different from the pulses to the others.

Measurements of transmission time delays

When the array performs an electronic focusing in the *x*-*z* plane, the pulse excitations to the array elements need to be time delayed appropriately to the required focal position. Accurate delays are very important to good focusing and accurate beam-steering. Therefore, it is necessary to check the delays and see how the actual delay times differ from the expected.

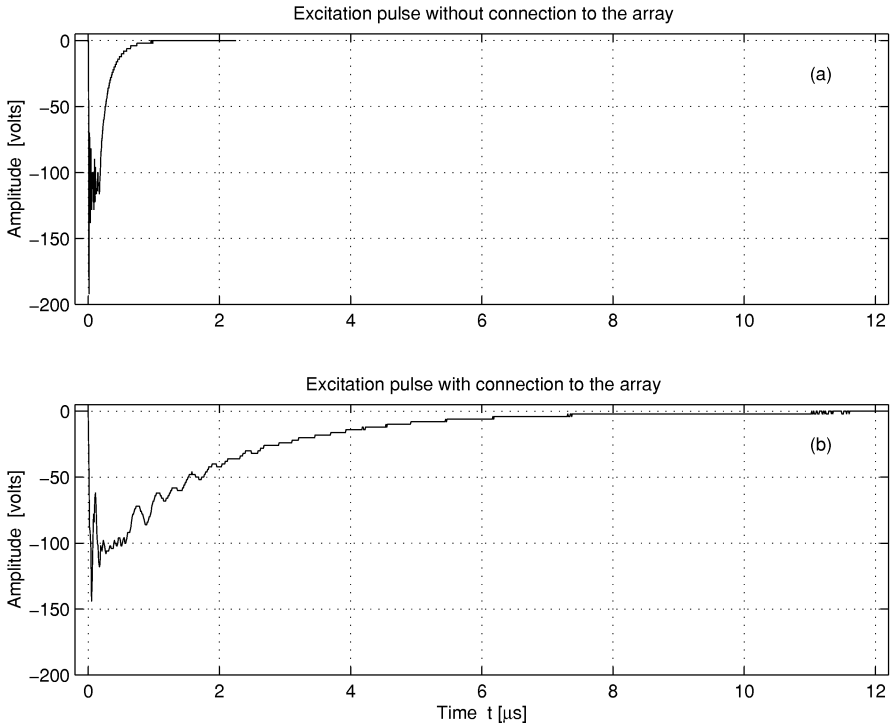

Fig. 1.10. Excitation pulses (a) without connection to the array, and (b) with connection to the array.

In the ALLIN system the delays for the transmission and the reception are separately controlled by two electronic modules [4]. The transmission delay times can vary from 0 to 8000 ns with 1 ns step. The reception delay times are not so fine in step and so large in range as the transmission ones; the size of step can be 5, 7.5, 10, 12.5 17.5, 25, 50 or 100 ns depending on the reception focusing board used. The delay times range from 0 to 39 x step. In our case, the reception focusing board is of 4 MHz frequency, which gives the step size of 25 ns [4] and the range of 975 ns. The methods of measuring the transmission and reception delays are different.

The transmission delay times were measured with the TEKTRONIX digital oscilloscope. The pulse to the first active element was used as the extern trigger to all the measurements, and the pulses to all the active elements were measured and recorded with the digital oscilloscope. By comparing the first recorded pulse to the rest, we obtained the actual delay times corresponding to the expected.

Here we present an example where 16 elements were used to make up the aperture and to focus a sound beam at z=170 mm in water. The actual delay times corresponding to the calculated (expected) delay times τ_c were measured in two cases, when the array was disconnected and connected. They are denoted by τ_m and τ_{ma}, respectively. The three different sets of delay times are listed in Table 1.1.

Table 1.1. Expected and measured delay times of transmission pulses in the case where a beam is supposed to be focused at 170 mm in water. All values are in nanosecond (ns).

Channel #	1	2	3	4	5	6	7	8	9	10	11	12	13	14	15	16
τ_c	0	28	52	72	88	100	108	112	112	108	100	88	72	52	28	0
τ_m	0	41	65	81	93	109	116	116	129	124	114	104	92	72	39	16
τ_{ma}	0	32	56	72	83	100	108	108	119	116	107	96	82	62	30	10

From the table, we learn that the measured delay times in two cases are quite different, and those in the second case when the array was connected are closer to the calculated. This also reveals that the time delays of an electric output are affected by its load.

The above measurement results demonstrate that the actual pulses to different array elements differ in shape and their delay times deviate from the expected. This factor which makes an actual beam deviate from the expected one should be taken into account in measurements.

C. Pulse echoes from small scatterers and reception time delays of the ALLIN system

Pulse echoes from small scatterers

When an ultrasonic transducer is used in a pulse echo mode, a rigid point-like scatterer can be used to measure the transmission/reception field of the transducer [42]. In practice, this rigid point-like scatterer is not available and small scatterers are used instead [43]. For calculation of a field radiated by a transducer, the velocity pulse excitation on the surface of the transducer needs to be known. This velocity pulse excitation can be determined by deconvolving the measured echoes from a small scatterer with the impulse response function of the ALLIN array, which will be dealt with in 1.3.2.6C.

In our experiments, a 16-element aperture was used to radiate a pulse field. The small scatterers used were two small carbide drilling bits which were flat-end cylinders with diameter of 0.3 mm and 0.5 mm. The pulse-echoes from the 0.3 mm and 0.5 mm scatterers were measured when the scatterers were located at different distances i.e., z = 10, 16 and 20 mm (see the dotted curves in Fig. 1.11). To reduce electronic noise, all the measured results were obtained after averaging 40 waveforms.

To facilitate the theoretical simulation of the fields from the array and determine the velocity distribution on the active surface of the array, an analytical function modeling the measured pulse echoes has been worked out in the form of a sinusoidal modulated signal,

$$s(t) = A_e t^m \exp(-B_e t^n) \sin(2\pi f_0 + \varphi_e), \tag{1.21}$$

where f_0 is the central frequency of the signal, and φ_e is the phase, and A_e, B_e, m and n determine the shape of the envelope. When m=1 and n=2, the envelope of $s(t)$ becomes Rayleigh-shaped. A_e can be easily found by the relation $\max[s(t)] = \max[\text{measured pulse echo}]$, but B_e, m and n may be determined by trial and error. Here we call $s(t)$ *simulated signal*.

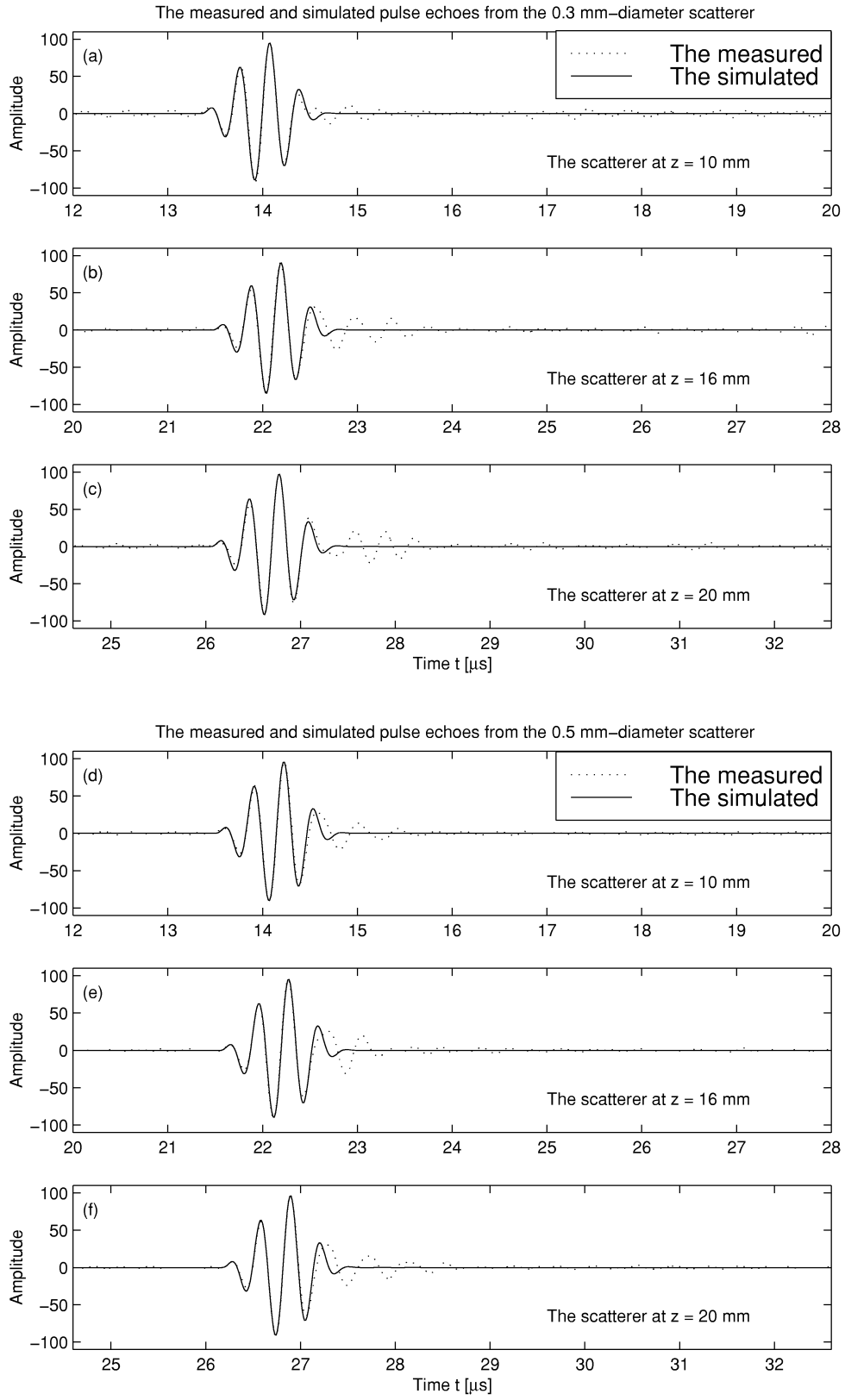

Fig. 1.11. Pulse echoes from the flat-ended cylindrical scatterers of diameters 0.3 mm and 0.5 mm at z=10, 16 and 20 mm on the array axis. (a) - (c) The echoes from the 0.3 mm-diameter scatterer, and (d) - (g) the echoes from the 0.5 mm-diameter scatterer.

To fit the simulated signal to the measured ones in Fig. 1.11, we estimated f_0=3.1 MHz, φ_e=0 radian, B_e=1.4, m=1.5 and n=4 which gave the simulated signals the best fitting for all six measurements (see the solid curves in Fig. 1.11). Note that A_e are different for all the measurements (since the six measured echoes differed in amplitude).

From Fig. 1.11, we can see that the simulated signals fit the measured ones very well except the narrow portions at the tail ends. By close observing these portions, we can find that they vary with the size and location of the scatterers, and may arise from the backscattering from the array backing, and thus they might not fit in the part of the pulse excitation. The above results show that Eq. (1.21) is a good model for pulse echo signals from the array.

Measurements of reception time delays

To measure the reception delays, we have established an experimental method which is simple but very effective. The method is implemented in the following procedure: first, configure the ALLIN system to separately acquire the signals received by the individual elements which are used together to constitute an aperture for the transmission, then locate a small scatterer on the aperture axis at a certain distance to the array, and then observe the output signals from all the individual elements. The output signals are displayed in B-mode, forming a profile of the fronts of the echoes from the small scatterer. By evaluating the echoes' fronts, we can determine the delay times of the received signals in the reception channels and thus the deviations of the actual delay times from the expected.

In the experiments for measuring the reception delays, 16 elements in the middle of the array, specifically, elements 25-40, were used as the active aperture to send a pulse, and a flat-end cylinder with diameter of 0.5 mm was used as the small scatterer and located on the axis of the aperture at distance of 190 mm to the array. The echoes received by the 16 elements were measured and recorded separately by the ALLIN system in the above-mentioned procedure. The delay times used in the measurements are listed in table 1.2. The 16 channels correspond to the active elements 25-40 of the array, respectively. Here we present three measurements.

Table 1.2. Expected and measured delay times in the measurements. All values are in nanosecond (ns).

Channel #	1	2	3	4	5	6	7	8	9	10	11	12	13	14	15	16
Foc000	0	0	0	0	0	0	0	0	0	0	0	0	0	0	0	0
Foc190T	0	26	46	64	78	90	96	100	100	96	90	78	64	46	26	0
Foc190R	0	66	114	160	194	224	240	250	250	240	224	194	160	114	66	0
Measured	0	30	50	70	90	100	110	110	110	110	100	90	70	50	30	0

In the first measurement, Foc190T was used for the transmission and Foc000 for the reception, the echoes received by the 16 elements were recorded at sampling frequency 100 MHz. The result is shown in Fig. 1.12(a), from which it can be seen that the fronts of the echoes received by the 16

elements form an arch convex toward the left. Based on the data in Fig. 1.12(a) and using the echo received by the first channel as a reference, we shifted the echoes received by the 2nd to 16th channels to the same time instant as the reference echo, after being shifted, all the 16 echoes were aligned almost on a vertical straight line. In this way, we found the time delays which, if they could be supplied by the ALLIN electronic system, would give the largest output after the echoes were superimposed through the electronic module, multiplexer, in the ALLIN system. The measured delay times are listed in 'Measured' row in table 1.2. Note that the measurement error could be ±10 ns because of the 100 MHz sampling frequency. Comparing the delay times in Foc190T with those in the 'Measured', we can see a little difference between them.

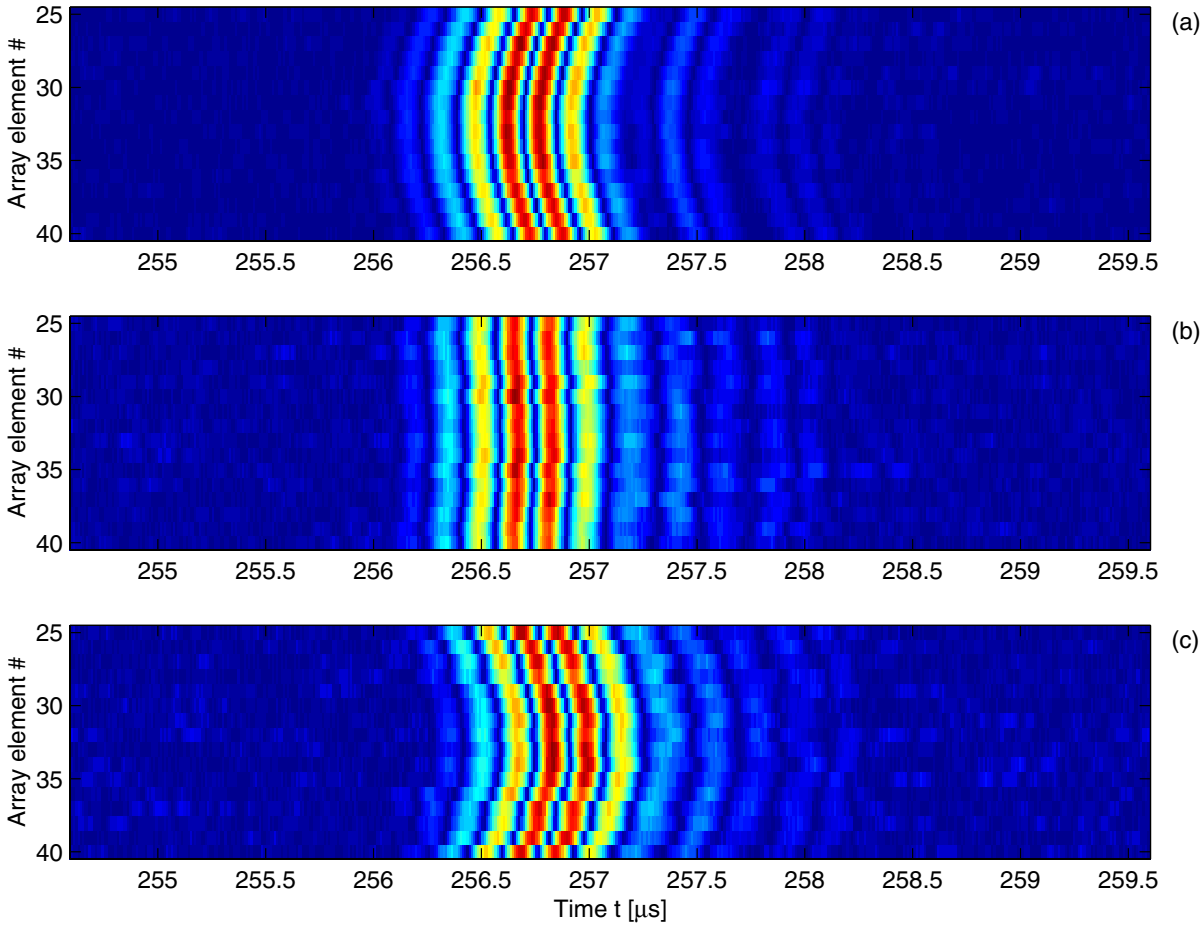

Fig. 1.12. Pulse echoes received by the 16 elements when the flat-ended cylindrical scatterer was located at z = 190 mm on the axis of the aperture made up of the 16-elements. (a) Foc190T was used for the transmission and Foc000 for the reception, (b) Foc190T was used for both the transmission and the reception, and (c) Foc190T for the transmission and Foc190R for the reception.

In the second measurement, Foc190T was used both for the transmission and the reception. What did we expect after the echoes to the 16 elements were time delayed according to Foc190T? The answer is that the 16 echoes should coincide in time, that is, they should be aligned on a straight line in the

image. The result in this case is illustrated in Fig. 1.12(b), from which we see the echoes' fronts almost along a straight line. This confirms that the delay times for the reception are quite accurate.
In the third measurement, Foc190T was used for the transmission and Foc190R for the reception. Foc190R was designed intentionally that over-delayed the pulse excitations. The result is shown in Fig. 1.12(c). From the figure, we can see that the fronts of the 16 echoes form a bow directed toward the right hand side because the focusing law, Foc190R, over-delayed the pulse excitations to the elements.
The above experiments have proven that the proposed experimental method is an effective means to evaluate the reception delays. Thus, this method can also be used to other applications like optimization of focusing and beam steering, and realization of the spatial averaging method for reducing grain noise.

1.3.2.6 Measurement and calculation of acoustic fields in water from the array

Acoustical fields radiated by the array into water were measured using a flat-end cylindrical scatterer with diameter of 0.5 mm. Obviously, the measured fields were those of transmission/reception (or pulse echo) mode. Because of the curved surface of the array in the y direction (see Fig. 1.6), geometrical focusing always exerts on the fields. In the x direction in which the elements are aligned linearly, the fields can be focused electronically or not. Below in this section, by non-focused and focused fields we mean those not focused and focused electronically.

A. Observation of focused transmission fields

In Sec. 1.3.2.5, we presented the measurements of delay times for the transmission and the reception and, we learnt that the errors of delay times exist both in the transmission and the reception case. In the transmission case presented in Sec. 1.3.2.5B, only the delay times were measured, and now we are going to examine transmission fields.
Due to the inaccuracy of the actual delays in the ALLIN system, we should find out a practical way to minimize the delay errors. We used the method presented in 1.3.2.5C. For this purpose, the experimental setup used in the measurements was slightly different. 16 elements were used the aperture to send pulse fields with different focusing laws, the scatterer was located at z=190mm, and the 64 elements were used as 64 receivers. With this setup, we tested six different focusing laws, that is, the focal positions were expected to be at z=160, 190, 220, 250, 290, infinity (non-focusing). For each focusing law, the array was scanned along the y direction from -3 mm to 3 mm with step 0.5 mm. To illustrate the measurements, we present a typical result obtained with the focal position at z=190 mm in Fig. 1.13. In Fig. 1.13(a) the result is displayed in "B-mode" corresponding to the on-axis case. In Fig. 1.13(b) the result is shown in "C-mode" which is obtained by gating all echoes with the full time interval used in Fig. 1.13(a). The two presentations complement each other, showing the beam

cross sections in different directions. It should be pointed out that the result in Fig. 1.13(b) has been smoothed by using the low-pass filter to get rid of the measurement noise from the electronic system. In the same way, we obtained the results for all other focal positions. In Fig. 1.14, we show for comparison the on-axis results of C-mode at y=0 when the focal positions were at z=190mm (solid), 290mm (dashed-dotted), and infinity (non-focused, dotted). Fig. 1.14 shows that the strength of focused field is higher at the point close to the focal zone compared the non-focused one, and that the field focused at z=190 mm is stronger than the one focused at z=290mm. Similarly, the focused fields were measured for focal points at 160, 220, and 250 mm. The maximal values of the fields obtained by using the focusing laws for non-focusing and for focusing at 160, 190, 220, 250, and 290 mm are listed in table 1.3, respectively. Note that the gains used in the cases were the same, and the values in the table are given in color scale levels

Table 1.3. Maximal values of the fields obtained by using the focusing laws for non-focusing and for focusing at 160, 190, 220, 250, and 290 mm. All values are in color scale levels.

Focusing law:	Nonfocusing	Focusing at z=160 mm	z=190 mm	z=220 mm	z=250 mm	z=290 mm
Maximum:	86.3	98.2	98.5	97.5	98.2	96.1

The table 1.3 demonstrates that, when the same focusing law applied to both the transmission and the reception, the field strength is maximal. Since the receiving condition of the array was kept unchanged, these results show how the transmission fields change with the different focusing laws.

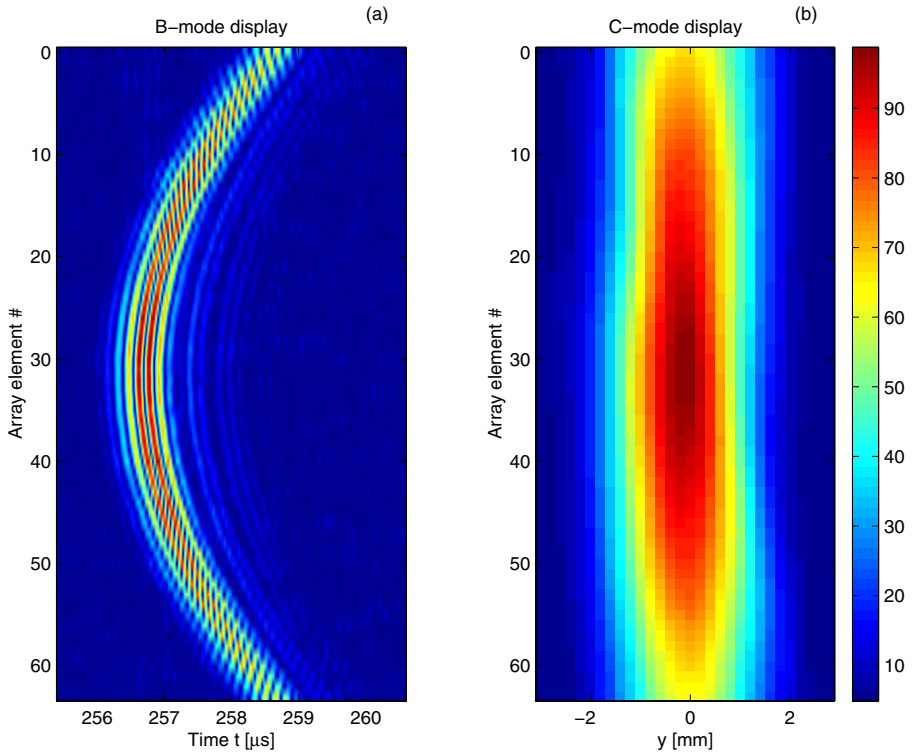

Fig. 1.13. Pulse echoes received by the 64 elements of the array when the flat-ended cylindrical scatterer was located at z = 190 mm on the axis of the aperture made up of elements 25-40, and Foc190T was used for the transmission. (a) Echoes displayed in B-mode, and (b) in C-mode.

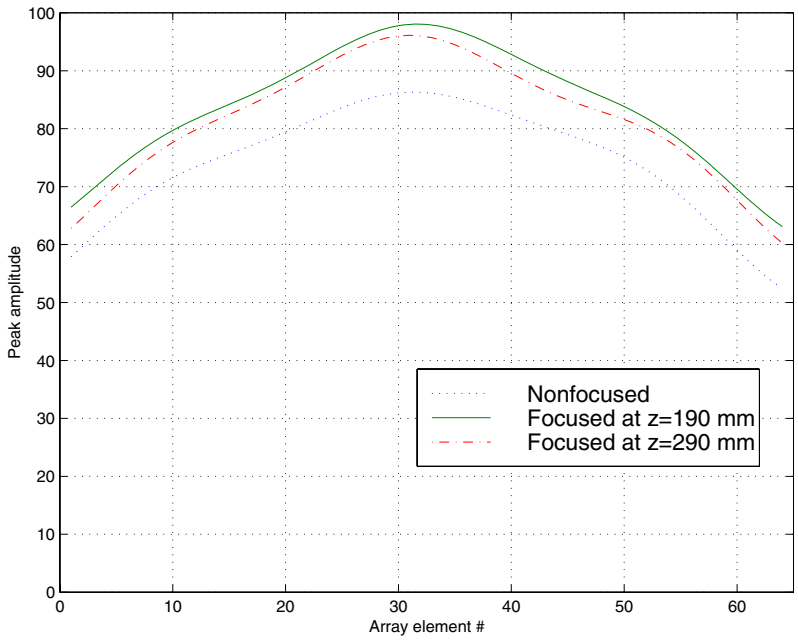

Fig. 1.14. Comparison of the peak amplitudes of echoes received by the 64 elements of the array when the flat-ended cylindrical scatterer was located at z = 190 mm on the axis of the aperture made up of elements 25-40, and the transmission fields were non-focused (the dotted) and focused at z= 190 mm (the solid) and z=290mm (the dashed-dotted).

B. Measurements of pulse echo fields from the array

The fields from the array with non-focusing and focusing were measured in transmission/reception (t/r) (or pulse echo) mode using the point-like scatterer. The measurements were done in the *x*-*z* and *x*-*y* planes by electronically scanning the array in the *x* direction and by mechanically scanning the array in the *z* and *y* directions, respectively. The mechanical scanning was performed by a mechanical scanning system consisting of two horizontal axes controlled by step-motors and one manual vertical axis.

In all the following experiments, 16 elements were used as the active aperture both for the transmission and the reception, and in the *x* direction, the array performed electronic scanning and gave 49 A-scans in one B-scan. All the measured results are displayed in terms of peak amplitude in relative units.

In the non-focusing case, we measured the fields in the *x*-*z* plane at *y*=0 (Fig. 1.15) by scanning the array from *z*=10 mm to 244 mm with step of 1mm, and the fields in the *x*-*y* plane at different depths, *z*=10, 130, 180, and 240 mm, respectively (Fig. 1.16), by scanning the array in the *y* direction.

In Fig. 1.15, we can see a peak around *z*=180 mm, which resulted from the geometrical focus due to the curved surface of the array with the radius of curvature 190mm.

In the focusing case, we used the focusing law, Foc190T, in the measurements. Since the field around the focal zone is of interest, the measurement in the *x*-*z* plane at *y*=0 (Fig. 1.17) was made by scanning the array from *z*=120 mm to 254 mm with step of 1mm, and the measurements in the *x*-*y* plane (Fig. 1.18) were done by scanning the array in the *y* direction at different depths, *z*=130, 180, and 240 mm, respectively.

Comparison of the non-focused (dashed) and the focused field (solid) is made in the illustrations of Fig. 1.19. The case on the array (*z*) axis (Fig. 1.19(a)) demonstrates that the focused field is largely strengthened over the range from 120 to 220 mm and reaches the maximum around *z*=170 mm. The cases along the lateral (*x* and *y*) axes (Figs. 1.19(b) - (g)) show that the beam widths of the focused field become narrower in the *x* direction in the displayed range, especially in the near field region (see Fig. 1.19(b)), but does not change much in the *y* direction since the geometrical focusing was fixed both for the electronically focused and non-focused fields. The - 3 dB beam widths of the non-focused and the focused fields in the *x* direction are 8.56 *vs* 3.83 mm at *z*=130 (Fig. 1.19(b)), 7.26 *vs* 4.93 at *z*=180 (Fig. 1.19(d)) and 7.78 *vs* 6.62 mm at *z*=240 (Fig. 1.19(f)), and the - 3 dB beam widths in the *y* direction are 7.47 *vs* 7.61 mm at *z*=130 (Fig. 1.19(c)), 2.70 *vs* 2.38 mm at *z*=180 (Fig. 1.19(e)) and 3.34 *vs* 3.28 mm at *z*=240 (Fig. 1.19(g)). Obviously, the beam is focused sharper in the near field than in the far field. This is in accordance with acoustics.

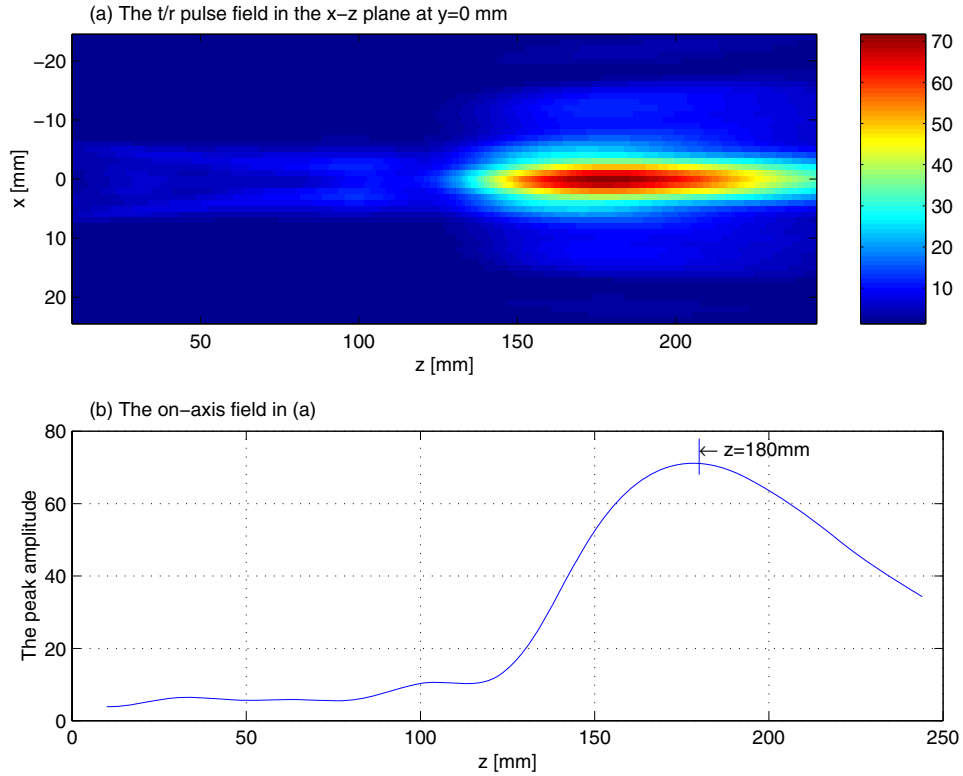

Fig. 1.15. The non-focused t/r pulse fields (peak amplitude) (a) in the *x*-*z* plane at *y*=0 and (b) on the array axis measured with the method in Sec. 1.3.2.5C. 16 elements were used as the transmission and reception aperture.

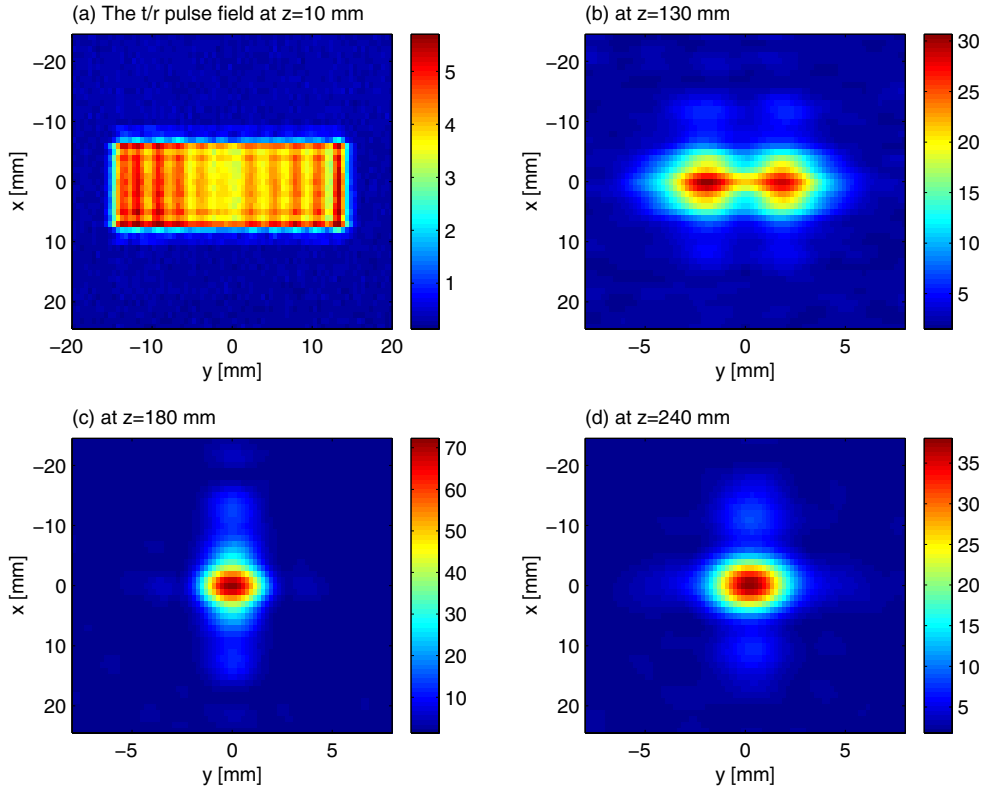

Fig. 1.16. The nonfocused t/r pulse fields (peak amplitude) in the *x*-*y* plane, at (a) z=10 mm, (b) 180 mm, (c) 230 mm and (d) 270 mm, measured with the method in Sec. 1.3.2.5C. 16 elements were used as the transmission and the reception aperture without focusing.

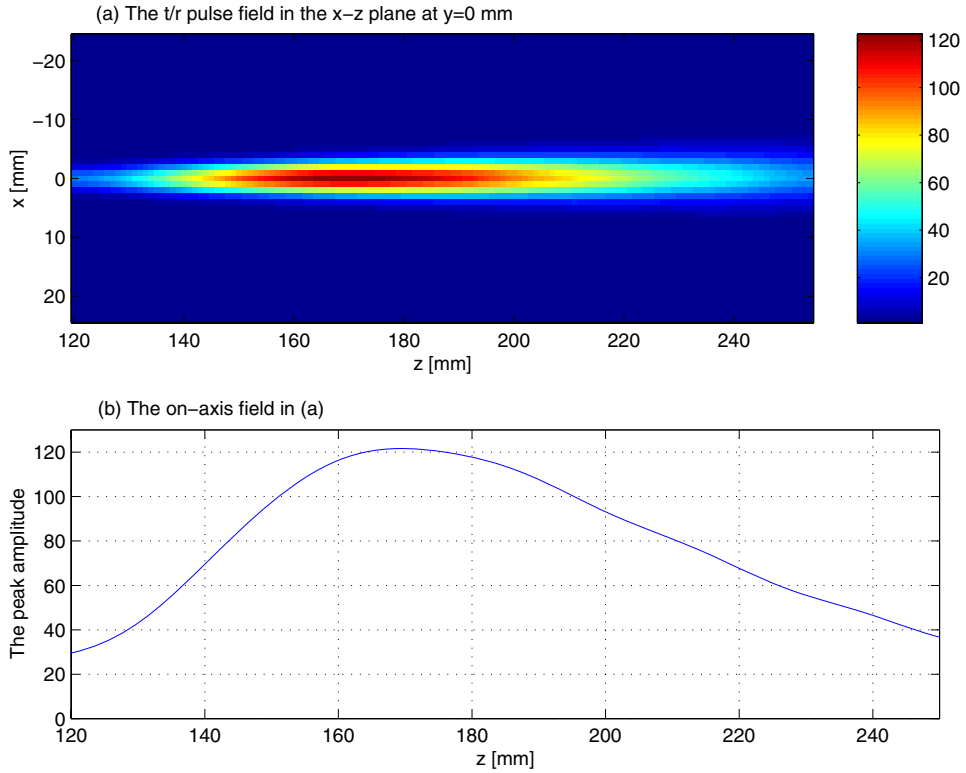

Fig. 1.17. The focused t/r pulse fields (peak amplitude) (a) in the *x*-*z* plane at *y*=0 and (b) on the array axis measured with the method in Sec. 1.3.2.5C. 16 elements were used as the transmission and reception aperture.

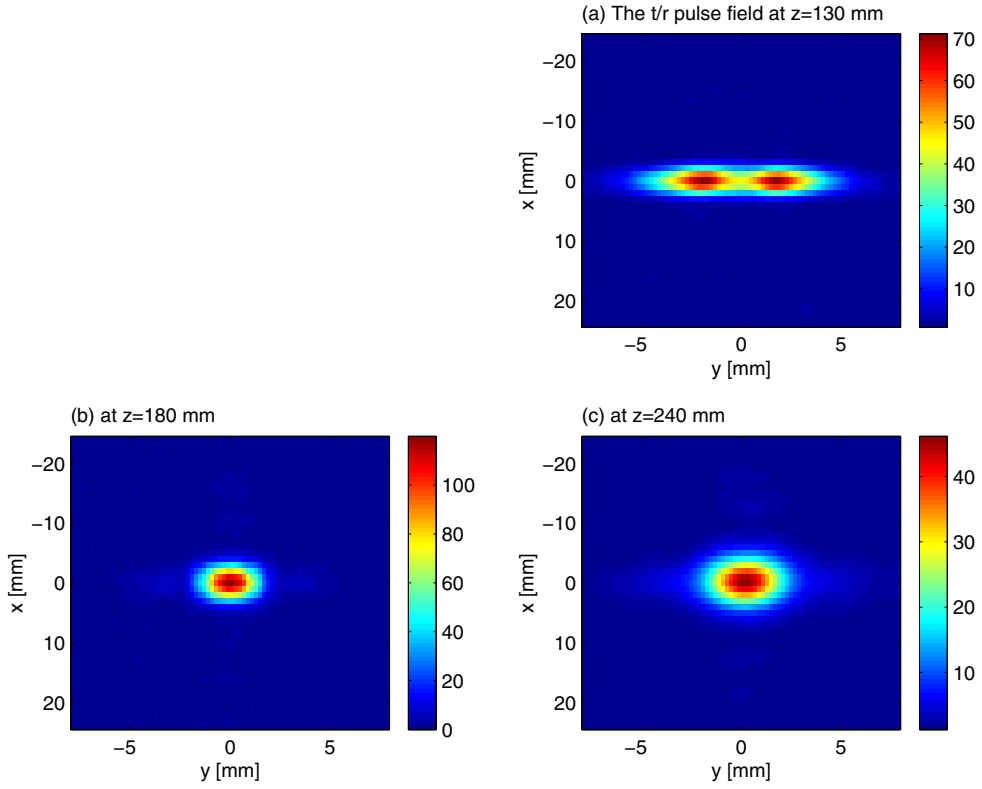

Fig. 1.18. The focused t/r pulse fields (peak amplitude) in the *x*-*y* plane, at (a) z=130 mm, (b) 180 mm, (c) 240 mm, measured with the method in Sec. 1.3.2.5C. 16 elements were used as the transmission aperture with focusing law Foc190T and the reception aperture with focusing law Foc190R.

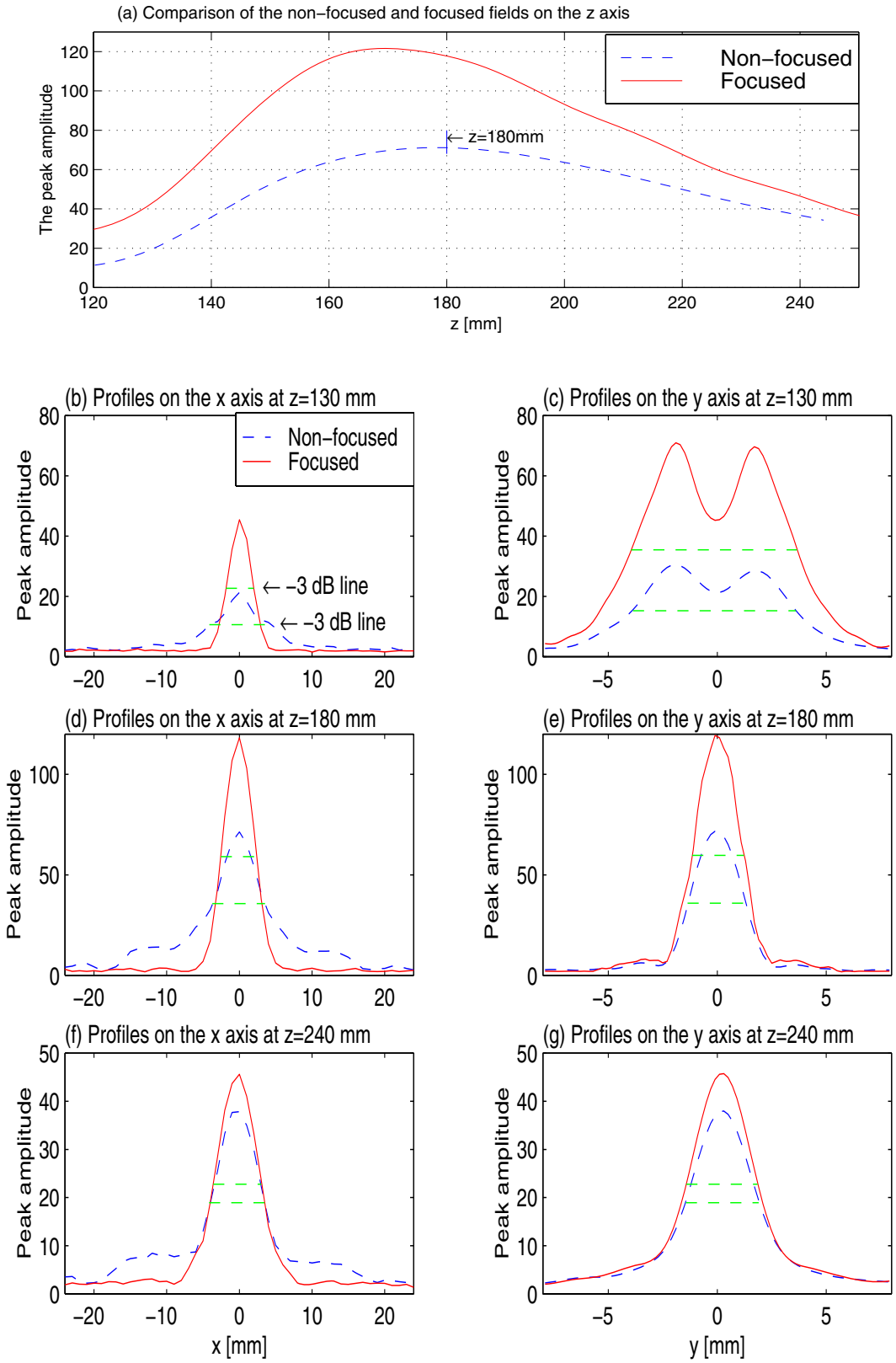

Fig. 1.19. Comparison of the non-focused (dotted curve) and focused (solid curve) t/r pulse fields (peak amplitude). (a) The fields in Figs. 1.15 & 1.17 on the z axis (the array axis), (b) & (c) the profiles in Figs. 1.16(b) & 1.18(a) on the x and y axis at z=130 mm, (d) & (e) the profiles in Figs. 1.16(c) & 1.18(b) on the x and y axis at z=180 mm, and (f) & (g) the profiles of Figs.1.16(d) & 1.18(c) on the x and y axis at z=240 mm.

C. Simulation of pulse echo fields and comparison with measurements

Based on the extended ASA presented in Sec. 1.3.2.2 and the optimal implementation of the ASA reported in [1,2,40], we have simulated the pulse echo fields radiated by the ALLIN array into water. To carry out the simulation, we first need to work out the pulse excitation of normal velocity on the array surface. The pulse excitation can not be obtained directly from measurement but it can be estimated by means of deconvolution from the measured echo from a point scatterer.

An output voltage measured from an ultrasonic system can expressed by [42-44]

$$E(t) = E_0 v_n(t) * h_t(\mathbf{r},t) * h_r(\mathbf{r},t)\,, \tag{1.22}$$

where $E(t)$, $h_t(\mathbf{r},t)$ and $h_r(\mathbf{r},t)$ are the measured output voltage, the transmission and reception spatial impulse function, respectively, and E_0 is constant. In Sec. 1.3.2.5C, we have obtained an analytical function simulating the measured pulse echoes (see Eq. (1.21)). $E(t)$ is replaced by the simulated signal in Eq. (1.21). The pulse excitation $v_n(t)$ is obtained by performing deconvolution of Eq. (1.12) using the simplified Wiener filter,

$$v_n(t) = \mathrm{IFFT}\left[V_n(\omega)\right] = \mathrm{IFFT}\left[\frac{H^*(\mathbf{r},\omega)}{\left|H(\mathbf{r},\omega)\right|^2 + q} S(\omega)\right], \tag{1.23}$$

where IFFT[.] means the inverse fast Fourier transform, $S(\omega)$ is the Fourier transform of the simulated pulse echo $s(t)$, and $H(\mathbf{r},\omega)$ is the Fourier transform of the spatial impulse response of the array and $H^*(\mathbf{r},\omega)$ is the conjugate of and $H(\mathbf{r},\omega)$. The normalized pulse excitation calculated from Eq. (1.23) and given $q = 0.001\max\left[\left|H(\mathbf{r},\omega)\right|^2\right]$ is shown in Fig. 1.20 with the simulated echo in Fig. 1.11.

Using the pulse excitation in Fig. 1.20, the pulse echo fields radiated by the ALLIN array were calculated. The nominal parameters of the array (see 1.3.2.5A) were used. The simulated results are compared with the measured ones on the axis at z = 20, 130, 180, and 240 mm (see Fig. 1.21). The comparison shows that the simulated and the measured results are in very good agreement. Furthermore, the non-focused and focused fields on the axis were calculated in terms of peak amplitude, and shown in Fig. 1.22(a) and (b) in solid curves, respectively, together with the corresponding measured fields in Figs. 1.15(b) and 1.17(b). The focusing law used in the calculation of the focused field was the same as the one used for the ALLIN array to have generated the focused field in Fig. 1.17. The comparison in Fig. 1.22 indicates that the simulated results are not in good agreement with the measured.

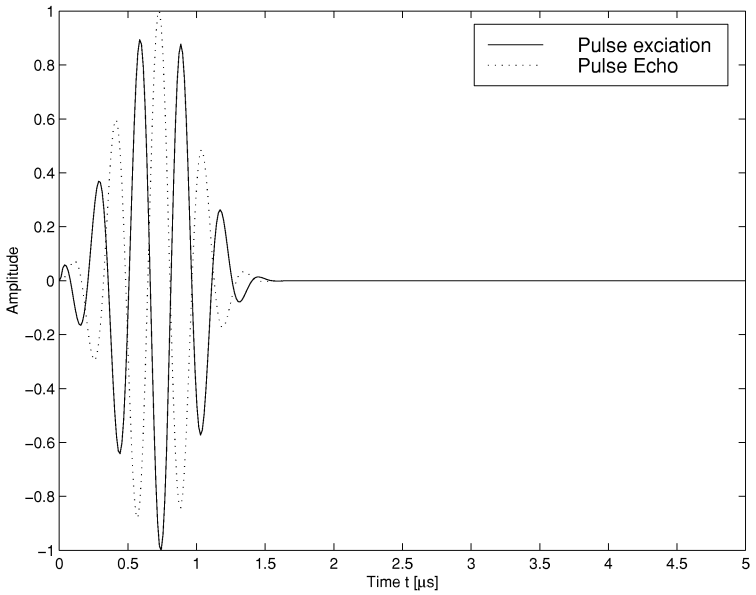

Fig. 1.20. Simulated pulse excitation (solid) obtained from the simulated pulse echo (dotted).

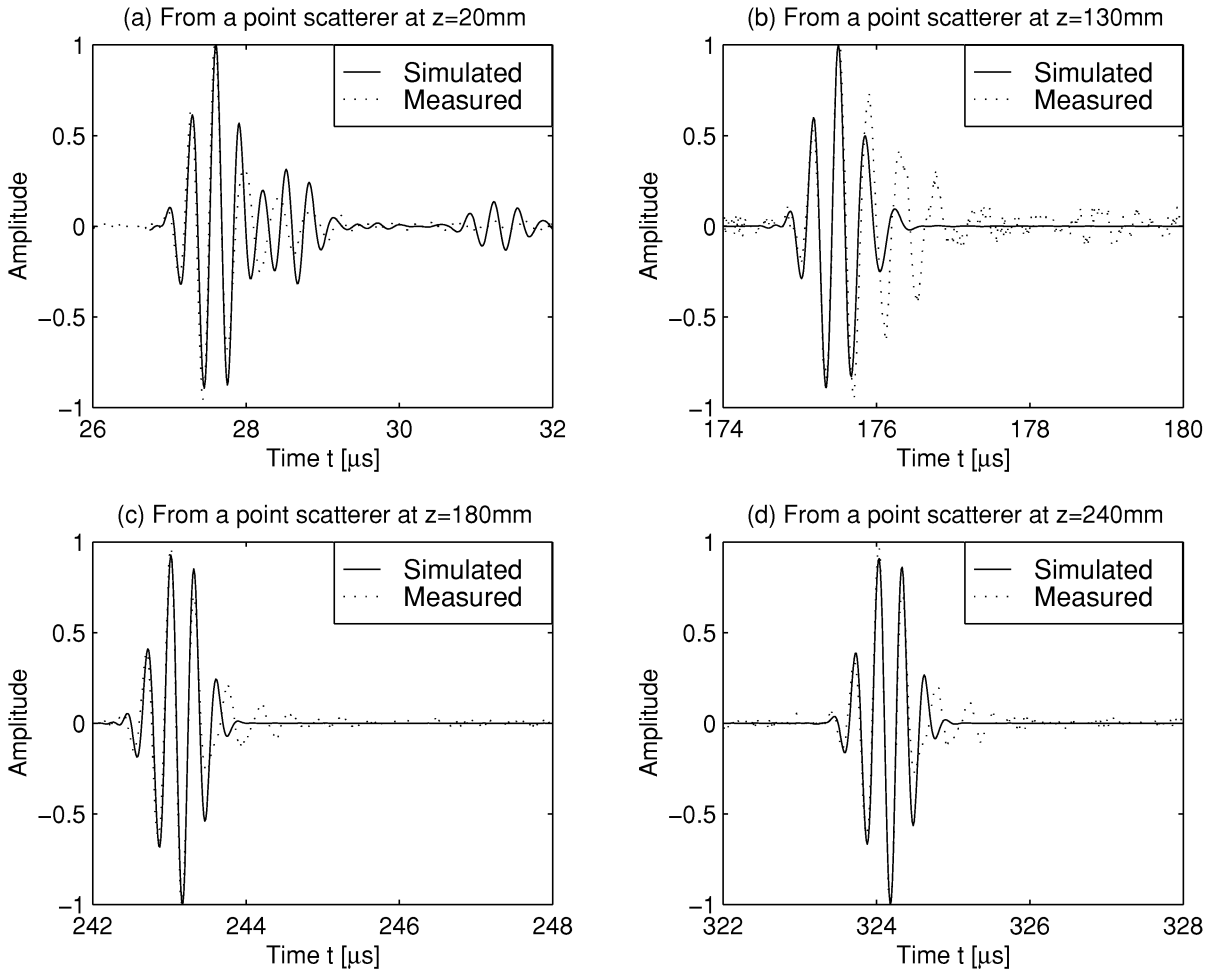

Fig. 1.21. Comparison of the simulated (solid) and measured (dotted) pulse echoes from a point scatterer located on the array axis at (a) z= 20mm, (b) z= 130mm, (c) z= 180mm, and (d) z= 240 mm, respectively, in the nonfocused fields from the ALLIN array.

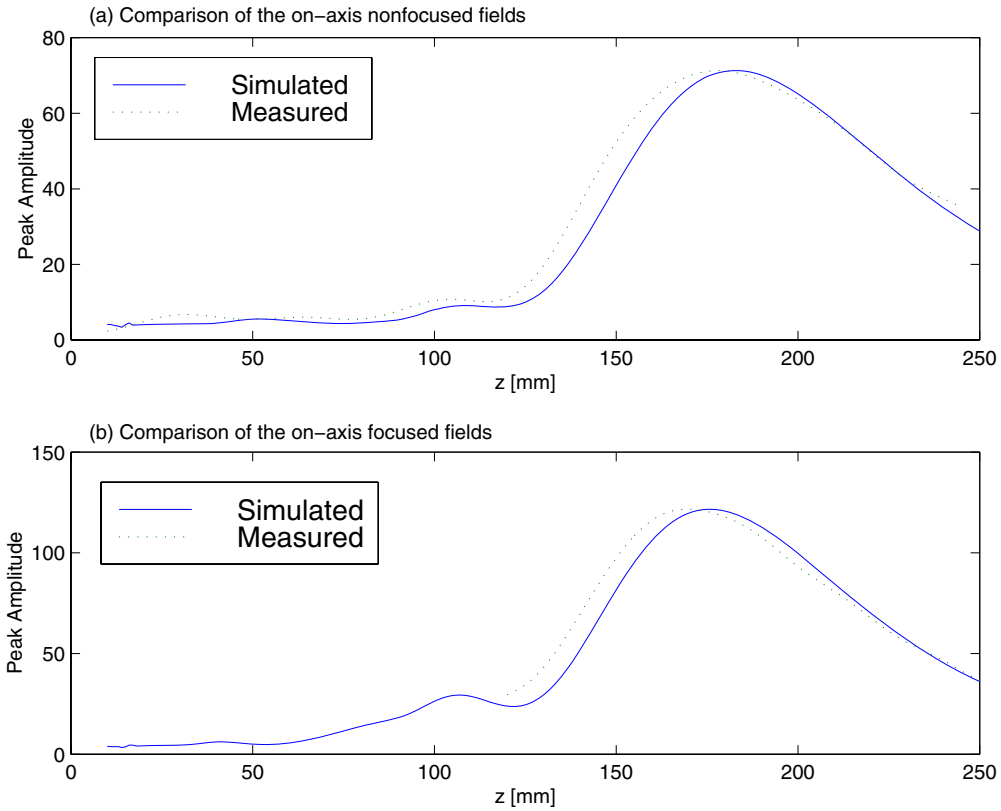

Fig. 1.22. Simulated nonfocused fields (solid) in terms of peak amplitude based the nominal parameters of the ALLIN array and comparison with measured ones (dotted).

From [12, 13, 15, 45-48] that dealt with characterization of spherically focused transducers and investigation of effective geometrical parameters for the focused transducers, we feel that it is not unusual that this disagreement happens to the cylindrically focused array because the nominal parameters, instead of effective parameters, were used in the calculation. Therefore, we made an effort to determine the effective parameters for the ALLIN array. The effective geometrical parameters found were effective radius of curvature, R, which was 187 mm, and effective length, $2b$, which was 31 mm. Using the effective parameters for the array, we calculated the nonfocused and focused fields in the x-z plane in terms of peak amplitude. The calculated results of the nonfocused and focused fields are shown in solid curves in Figs. 1.23 and 1.24, respectively, together with the corresponding measured results (in dotted curves). In both figures, (a) shows the simulated fields in the x-z plane in color scale levels, (b) shows the field on the axis, and (c) - (f) show the cross-axis fields at z = 20, 130, 180 and 240 mm, respectively. From the comparison in Figs. 1.23(b) - (f) and 1.24(b) - (f), as well as the comparison of Figs. 1.23(a) and 1.24(a) with Figs. 1.15(a) and 1.17(a), respectively, we see that the simulated fields and the measured are in a very good.

From the above work, we have validated the newly developed modeling tool for the ALLIN array, as well as for such a kind of transducers with cylindrically curved surfaces, and also demonstrated that effective geometrical parameters need be determined and used in the simulation to achieve good accuracy.

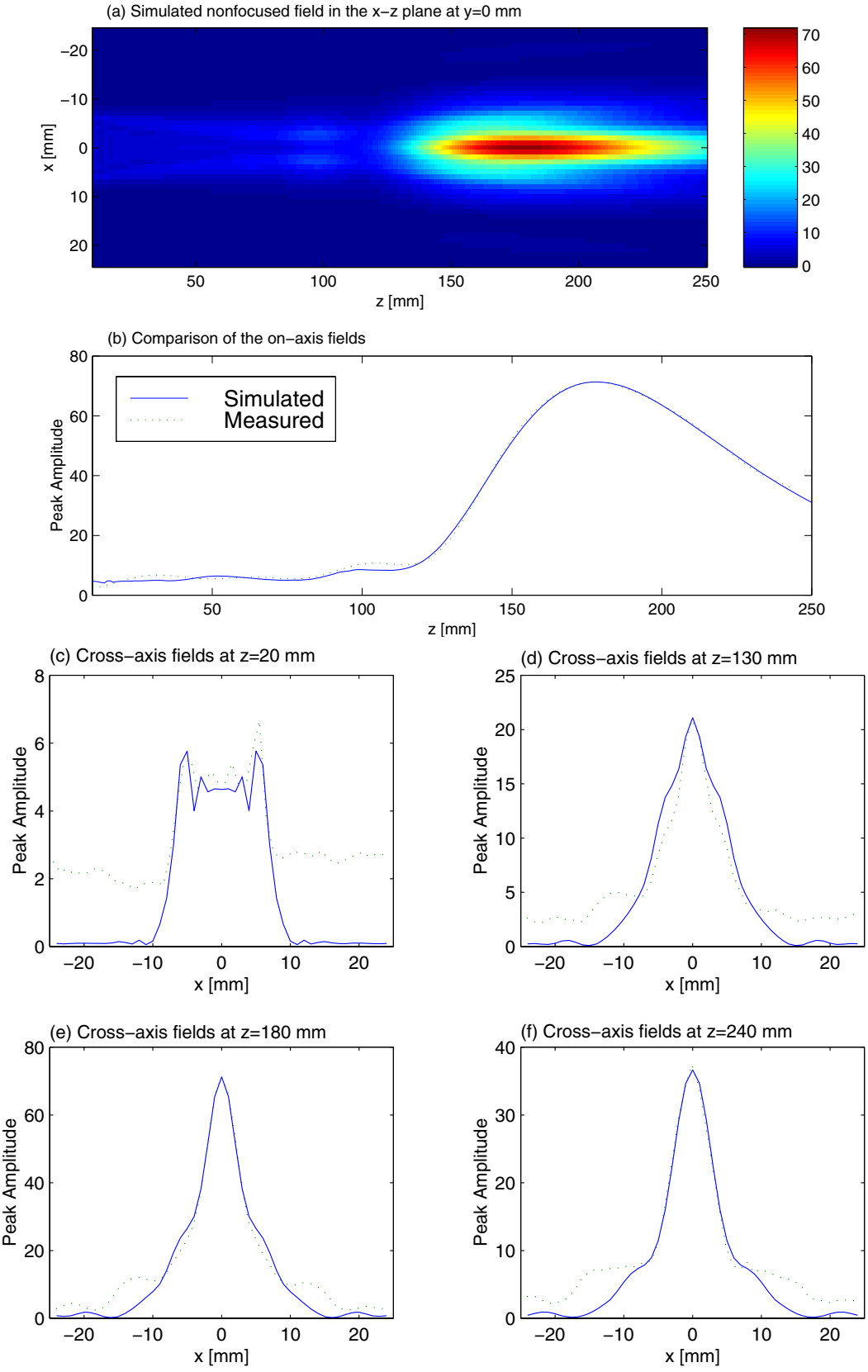

Fig. 1.23. Simulated nonfocused fields (solid) in terms of peak amplitude and comparison with measured ones (dotted). (a) Simulated field in the *x*-*z* plane at *y* = 0, (b) comparison of the on-axis fields, and (c) - (f) the profiles of the fields at *z*= 20, 130, 180, and 240 mm, respectively.

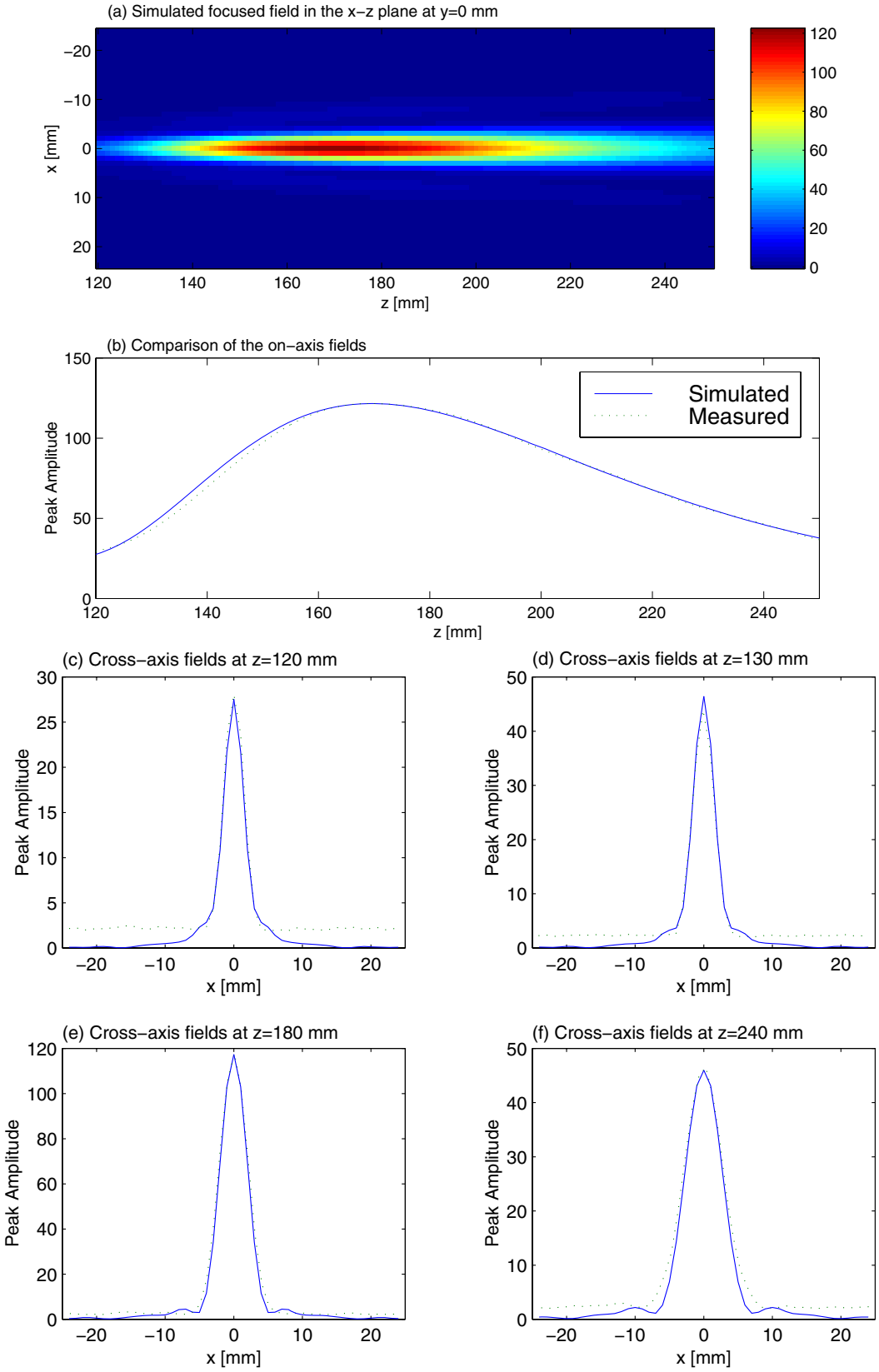

Fig. 1.24. Simulated focused fields (solid) in terms of peak amplitude and comparison with measured ones (dotted). (a) Simulated field in the *x*-*z* plane at $y = 0$, (b) comparison of the on-axis fields, and (c) - (f) the profiles of the fields at z= 120, 130, 180, and 240 mm, respectively.

1.4 Conclusions

Beam-forming and modeling tools have been developed for designing steered and/or focused beams and for simulating ultrasonic fields in fluids and solids. The modeling tools have been verified in theoretical and experimental ways.

The tool for beam-forming has been developed based on geometrical acoustics and has been used for designing angle (steered) and/or focused beams that are best suitable for various situations encountered in inspection of copper canisters immersed in water. These focused, steered beams are to be used for sizing defects and inspecting the regions close to canisters outer walls. This will be presented in the following chapter. Presently, the tool only utilizes delays to control beams. In the future work, apodization should be also explored.

The modeling tool for simulating elastic fields radiated by planar arrays into immersed solids has been verified by comparing with the results obtained from a commercial PC software PASS. The results from our modeling tool and the PASS have been shown to be in excellent agreement.

The modeling tool has been upgraded and now it can be applied not only to the planar arrays but also to the ALLIN array which has a cylindrically curved surface for focusing beams in the y direction. The theory underlying this upgraded modeling tool is the extended ASA which is not only applicable to planar sources but also to arbitrarily curved sources. The model tool has been verified experimentally for the ALLIN array.

To quantify the fields from the ALLIN array and to facilitate the comparison of simulated results with the measured ones, the ALLIN array system has been calibrated based on the existing functionality, and an analytical model has been established for simulating measured acoustic echo pulses. For the calibration, several experimental methods have been established for measuring the transmission and reception time delays, and measuring ultrasonic fields from the array. The measurements of fields in water were performed using a point-like scatterer.

To obtain pulse excitation of normal velocity on the array surface from measurements by deconvolving it with the impulse response of the array, a method has been developed for finding out the impulse response of an arbitrarily curved source. The method is the extended version of the conventional impulse response method which has, up to now, been restricted to treating planar sources and spherically or axisymmetrically curved sources.

The measured and the simulated fields in water for the ALLIN array have been compared and shown to be in excellent agreement. Characterization of the ALLIN array has been made using this model, and the effective specifications for the array have been found.

1.5 References

[1] T. Stepinski, and P. Wu, *Ultrasonic Inspection of Nuclear Copper Canisters*, SKB Projektrapport 97-01, December 1996.

[2] T. Stepinski, and P. Wu, *Ultrasonic Inspection of Nuclear Copper Canisters*, SKB Projektrapport 97-08, August 1997.

[3] *Measurement Report*, Imasonic, France, Oct. 1995.

[4] *ASTUS Configuration, Version 2.3, User Guide*, NDT Systems, France, July, 1995.

[5] C. Lee and P.J. Benkeser, "Computationally efficient sound field calculations for a circular array transducer," *IEEE Trans. Ultrason. Ferroelec. Freq. Contr.* vol. 39, pp. 43-47, 1992.

[6] A. O. Williams, "Acoustic intensity distribution from a 'piston' source. – II. The concave piston," *J Acoust. Soc. Am.,* vol. 17, pp. 219-227, 1946.

[7] H.T. O'Neil, "Theory of focusing radiators," *J Acoust. Soc. Am.,* vol. 21(5), pp. 516-526, 1949.

[8] A. Freeman, "Sound field of plane or gently curved pulsed radiators," *J Acoust. Soc. Am.,* vol. 48, pp. 221-228, 1969.

[9] A. Penttinen and M Luukkala, "The impulse response and pressure nearfield of a curved radiator," *J. Phys D, Appl. Phys.* vol. 9, pp. 1547-1557, 1976.

[10] M. Arditi, F.S. Foster, and J.M. Hunt, "Transient fields of concave annular arrays," *Ultrason. Imag.,* vol. 3, pp. 37-61, 1981.

[11] A. Weyns, "Radiation field calculation of pulsed ultrasonic transducers: Part 2: Spherical disc- and ring-shaped transducers," *Ultrasonics,* vol. 18, pp. 219-223, 1980.

[12] E.L. Madsen, M.M. Goodsitt, and J.A. Zagzebski, "Continuous waves generated by focused radiators," *J. Acoust. Soc. Am.*, Vol. 70, pp. 1508-1517, 1981.

[13] M.M. Goodsitt, E.L. Madsen, and J.A. Zagzebski, "Field patterns of pulsed, focused, ultrasonic radiators in attenuating and nonattenuating media," *J. Acoust. Soc. Am.*, Vol. 71, pp. 318-329, 1982.

[14] B.G. Lucas and T.G. Muir, "The field of a focusing source," *J. Acoust. Soc. Am.*, vol. 72, pp.1289-1296, 1982.

[15] W.N. Cobb, "Frequency domain method for the prediction of the ultrasonic field patterns of pulsed, focused radiators," *J. Acoust. Soc. Am.*, vol. 75, pp.72-79, 1984.

[16] M.A. Fink, and J.-F. Cardoso, "Diffraction effects in pulse-echo measurement," *IEEE Trans Sonics &Ultrason.*, vol. SU-31, pp. 313-329, 1984.

[17] I. Hasegawa, N. Inoue , and K. Matsuzawa, "A new theory for the radiation from a concave piston source," *J. Acoust. Soc. Am.*, Vol. 82, pp. 706-708, 1987.

[18] T.J. Hall, E.L. Madsen and J.A. Zagzebski, "A Taylor series expansion for time savings in accurate computation of focused ultrasound pressure fields ," *Ultrasonics*, Vol. 9, pp. 203-219, 1987.

[19] M.F. Hamilton, "Comparison of three transient solutions for the axial pressure in a focused sound beam," *J. Acoust. Soc. Am.*, Vol. 92, pp. 527-532, 1992.

[20] F. Coulouvrat, "Continuous field radiated by a geometrically focused transducer: Numerical investigation and comparison with an approximate model," *J. Acoust. Soc. Am.*, Vol. 94, pp. 1663-1657, 1993.

[21] X. Chen, K.Q. Schwarz, and K.J. Parker, "Radiation pattern of a focused transducer: A numerical convergent solution," *J. Acoust. Soc. Am.*, Vol. 94, pp. 2979-2991, 1993.

[22] C. Lee, and P.J. Benkeser, "A computationally efficient method for the calculation of the transient field of acoustic radiators," *J. Acoust. Soc. Am.*, Vol. 96, pp. 545-551, 1994.

[23] A.T. de Hoop, S. Zeroug, and S. Kostek, "Transient analysis of the transmitting properties of a focused acoustic transducer with an arbitrary rim," *J. Acoust. Soc. Am.*, Vol. 98, pp. 1767-1777, 1995.

[24] D. Cathignol, and P. Faure, "Acoustic fields of arbitrary plane or spherical transducers," in *Acoust. Imag.*, Vol. 22, Ed. P. Tortoli & Masptti. Plenum Press, New York, pp. 459-464, 1996.

[25] L.W. Schmerr, Jr., A. Sedov, and T.P. Lerch, "A boundary diffraction wave model for a spherically focused ultrasonic transducer," *J. Acoust. Soc. Am.*, Vol. 101, pp. 1269-1277, 199.

[26] D. Sette, "Ultrasonic lenses of plastic materilas," *J. Acoust. Soc. Am.*, Vol. 21, pp. 35-381, 1949.

[27] G.C. Knollman, J.L.S. Bellin, and J.L. Weaver, "Variable-focus liquid-filled hydroacoustic lens," *J. Acoust. Soc. Am.*, Vol. 49, pp. 253-261, 1971.

[28] T. Tarnoczy, "Sound focusing lenses and waveguides," *Ultrasonics*, pp. 115-127, 1965.

[29] J.T. McElroy, "Focused ultrasonic beams (nondestructive testing)," *Int. J. Nondestr. Test.*, Vol. 3, pp. 27-58, 1971.

[30] E.P. Papadakis, "Lens equation for focused transducers," *Int. J. Nondestr. Test.*, Vol. 4, pp. 195-198, 1972.

[31] D.L. Folds, "Focusing properties of solid ultrasonic cylindrical lenses," *J. Acoust. Soc. Am.*, Vol. 53, pp. 826-834, 1973.

[32] E. Cavanagh and B.D. Cook, "Lens in the nearfield of a circular transducer: Gaussian-Laguerre formulation," *J. Acoust. Soc. Am.*, Vol. 69, pp. 345-351, 1981.

[33] A. Penttinen and M. Luukkala, "Sound pressure near the focal area of an ultrasonic lens," *J. Phys.* D, *(Appl. Phys.)* vol. 9, pp. 1927-1936, 1976.

[34] U. Schlengermann, "Schallfeldausbildung bei ebenen ultraschallquellen mit fokussierenden linsen," *Acustica*, Vol. 30, pp. 291-400, 1974.

[35] U. Schlengermann, "The characterization of focussing ultrasonic transducers by means of single frequency analysis," *Mater.Evla.,* vol. 38, pp. 73-79, 1980.

[36] Y.J. Yoon, and P.J. Benkeser, "Sound field calculations for an ultrasonic linear phased array with a spherical liquid lens," *IEEE Trans. Ultrason. Ferroelec. Freq. Contr.* vol. 39, pp. 268-272, 1992.

[37] R.B. Thompson, and E.F. Lopes, "The effects of focusing and refraction on Gaussian ultrasonic beams," *J. Nondestr. Eval.*, vol. 4, pp. 107-123, 1984.

[38] R.B. Thompson, T.A. Gray, J.H. Rose, V.G. Kogan, and E.F. Lopes, "The radiation of elliptical and bicylindrically focused piston transducers," *J. Acoust. Soc. Am.*, vol. 82, pp. 1818-1828, 1987.

[39] G.R. Harris, "Review of transient field theory for a baffled piston," *J. Acoust. Soc. Am.*, vol. 70, pp. 10-20, 1981.

[40] P. Wu, R. Kazys and T. Stepinski, "Optimal selection of parameters for the angular pectrum approach to numerically evaluate acoustic fields," *J. Acoust. Soc. Am.,* **101**, pp. 125-134, (1997).

[41] J.W. Goodman, *Introduction to Fourier Optics*. McGraw-Hill Book Company, New York, Chap. 3, (1968).

[42] A. Lhemery, "Impulse-response method to predict echo-responses from targets of complex geometry. Part I: Theory," *J. Acoust. Soc. Am.* **90:** 2799-2807 (1991).

[43] A. Lhemery, "Impulse-response method to predict echo-responses from targets of complex geometry. Part II: Computer implementation and experimental validation," *J. Acoust. Soc. Am.* **95:** 1790-1800 (1994).

[44] J.P. Weight and A.J. Hayman, "Observations of the propagation of very short ultrasonic pulses and their reflection by small targets," *J. Acoust. Soc. Am.* **63:** 396-404 (1978).

[45] J. Adach, and R.C. Chivers, "Effective geometrical parameters for a spherical cap transducer," *Acustica*, Vol. 62, pp. 66-74, 1986.

[46] J. Adach, and R.C. Chivers, "A detailed investigation of effective geometrical parameters for weakly focussed ultrasonic transducers. Part I: optimisation of experimental procedures," *Acustica*, Vol. 70, pp. 12-22, 1990.

[47] J. Adach, and R.C. Chivers, "A detailed investigation of effective geometrical parameters for weakly focussed ultrasonic transducers. Part II: a systematic study including an absobing medium," *Acustica*, Vol. 70, pp. 135-145, 1990.

[48] T.P. Lerch, L.W. Schmerr, and A. Sedov, "Characterization of spherically focused transducers using an ultrasonic measurement model approach," *Res. Nondestr. Eval.*, Vol. 8, pp. 1-12, 1996.

2 Detection and resolution limits of ultrasonic inspection of copper canisters

2.1 Introduction

In ultrasonic inspection of welds in copper canisters, the ability to detect flaws and defects in the welds is limited by grain noise, and the regions close to the outer walls of the canisters are often difficult to reach by means of normal incident beams due to canisters' geometry.

To assess welds, we have to estimate defect sizes, but defect sizing is often limited by the resolution determined by beam diffraction. Therefore, the detection and resolution limits are investigated in the present work. The investigation is based on a series of experiments made on several copper blocks and canister segments by means of the ALLIN array system which provides us with the capacity of designing and realizing appropriate beams for the immersion inspections. The experiments were arranged in the following sequence:

(i) The first experiment is intended for designing optimal focusing laws for some specified cases. For example, in some cases we may need a good spatial resolution for defect sizing, but in the other we may require a beam which provides uniform B-mode imaging. In the experiment, two apertures consisting of 16 and 32 elements, respectively, were used. Various focusing laws for each of the apertures have been designed to focus beams at different depths in a copper block submerged in water. The copper block contained a set of holes side drilled at different depths. The focused beams radiated by the two apertures in the block have been evaluated. This enables us to select an optimal focusing law for generating a beam best suitable for a specified situation.

(ii) The second experiment is targeted at evaluating detection limit. Artificial defects, like side-drilled, flat- and round-bottom holes, located in the weld zone of a canister segment, have been inspected using beams that were formed by the apertures with optimal focusing laws designed in (i). From the analysis of images of the defects, detection limit has been assessed.

(iii) The third experiment is aimed at evaluation of detection limit for defects located close to the outer walls of inspected materials. Zones close to the outer wall of a copper block have been inspected using focused beams which were steered by various angles. The block contained five sets of flat-bottom holes, each set with a hole diameter different from the others.

(iv) The forth experiment was performed to investigate the detection limit in a more realistic situation. Two canister segments have been inspected which have side-drilled holes with various depths and sizes located in the weld zones. The beams used were focused and steered by various angles.

2.2 Experimental design of focused beams for immersion test

In Sec. 1.2, a beamforming tool has been developed for designing steered and/or focused beams used for immersion inspections. The beamforming tool is used and verified in the present work. In sequel, the focusing due to the beamforming is called electronic focusing, and the focusing due to the curvature of the array elements in the *y* direction is called geometrical focusing.

2.2.1 Copper block CU2 and experimental setup

A test block made of copper was designed for evaluating focusing laws obtained from the beamforming tool. The copper block, shown in Fig. 2.1, is 74x74x320 mm in dimension and has 18 side-drilled holes located at depths 4, 8, …, 72 mm in the block. All the holes have diameter of 1 mm, that is smaller than the wave length (1.53 mm) in copper at the array center frequency 3 MHz. The horizontal spacing of the adjacent holes is 15 mm. The first hole at 4 mm and the last at 72 mm contained drill bits that were broken and stuck in. Therefore, holes 2-17 are useful for the experiment.

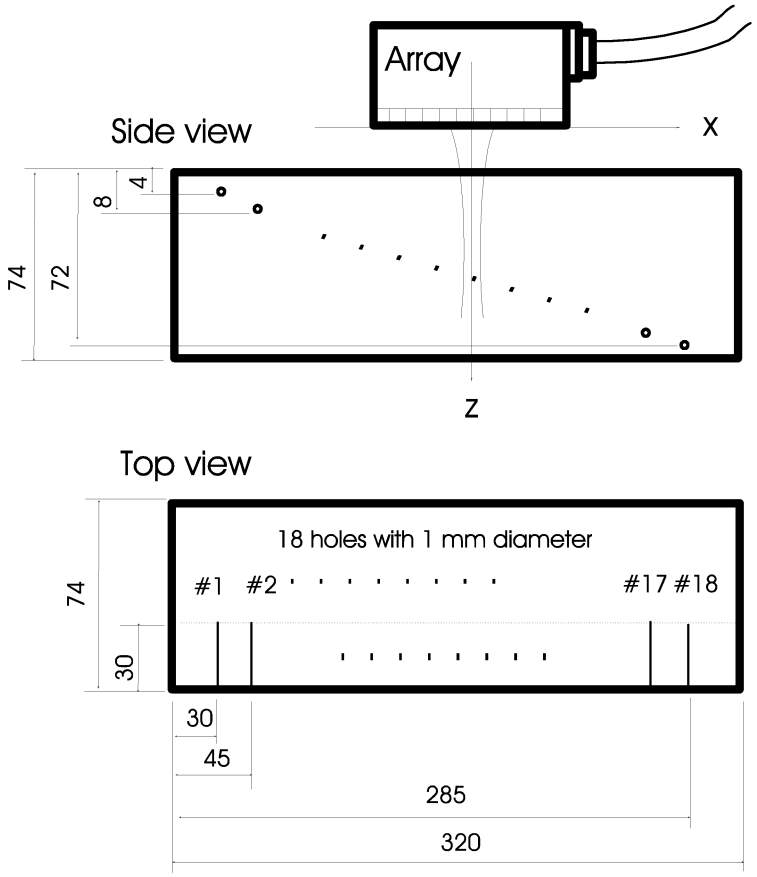

Fig. 2.1. Geometry of copper block CU2 and the array for measuring the ultrasonic fields in the block.

The block and the array both were put in water in the way as shown in Fig. 2.1. The water path from the array to the front surface of the block was 28 mm. To acquire such B-scan images including all holes, and to guarantee the best uniformity of the scanning beams, only one fixed aperture in the middle of the array was used in the measurements and the array was scanned mechanically (not electronically!) along the *x* direction from the left end of the block to the right end (see Fig. 2.1). Due

to the linear alignment of array elements in the *x* direction, the beams can be focused at various depths in the *x*-*z* plane. The aperture of two different sizes, specifically, consisting of 16 or 32 elements around the center of the array, was employed, respectively, in measurements. It means that the images were obtained using either the 16-element aperture or the 32-element aperture.

2.2.2 Measurements and discussions

For either of the 16-element and the 32-element aperture, a set of focusing laws were used which were designed to focus beams at 20, 32, 40, 52, 60, 72, 80 mm in the copper block, respectively. In sequel, the focusing laws are denoted Foc20E16, Foc32E16, …, Foc80E16, *etc*. for the 16-element aperture, and Foc20E32, Foc32E32, …, Foc80E32, *etc*. for the 32-element aperture. In the case of the 16-element aperture, one more focusing law was used which focused beam at 12 mm in the block, and the corresponding focusing law for the 32-element aperture could not be realized in the ALLIN system because some delay times in the focusing law were larger than 975 ns, which is the upper limit of delay time available for the reception. To illustrate experiments we present some of the measured results. The gains used in the measurements were always the same for either aperture, specifically, 8 dB for the 16-element aperture, and 3 dB for the 32-element aperture. Fig. 2.2 shows five B-scans which were obtained with the 16-element aperture using the focusing laws for focusing beams at 12, 20, 40, 60, and 80 mm, respectively. Fig. 2.3 shows four B-scans which were obtained with the 32-element aperture using the focusing laws for focusing beams at 20, 40, 60, and 80 mm, respectively. All the B-scans were displayed in terms of envelope which was obtained using Hilbert transform. Therefore, each peak (above the grain noise level) in the images corresponds to an echo from a side-drilled hole at a certain depth in the block. Each of the B-scans is displayed in the depth range of 9 - 73 mm in the block (in the *z* direction) and from 0 to 290 mm in the *x* direction. In each of the B-scans, only 15 holes, i.e., holes #3 - #17, are visible, because the hole # 2 at 8 mm was completely masked by the echo from the front surface. This indicates that depth from 0 - 8.5 mm in the block is the dead zone in the inspection. Each B-scan image is completed by the projections to the *y*- and *z*-axis, respectively, above and on the right hand side. The projections to the *y*- and *z*-axis facilitate the analysis of resolutions, lateral and axial, respectively. The amplitudes (A_{peak} in relative unit) and the -3 dB beam widths (BM, in mm) of the peaks in Figs. 2.2 and 2.3 were measured based on the projections to the *x*-axis and they are listed in tables 2.1 and 2.2, respectively. It should be pointed out that the values in columns A_{peak} and BM that could not be measured from the projections are left empty.

While making the analysis of focused beams, we should bear in mind the fact that the geometrical focusing due to the curvature of the array in the *y* direction always exists and that the widths of peaks in the *x*-axis projections and in the *z*-axis projections represent the beam widths (the lateral resolution) and the duration of the echoes (the axial resolution), respectively.

Comparison of the B-scans in sequence from (a) to (e) in Fig. 2.2 and from (a) to (b) in Fig. 2.3 (also refer to Tables 2.1 and 2.2) leads to the following conclusions:

(i) From the B-scan images we can see the desired focusing effect, which means that the positions of the focal zones moved downwards as the beams were focused deeper in the block, and also see that the deeper the beams are focused the larger the focal zones become; ####e.g., the focal zone is located around 12 - 20 mm for Foc12E16, 12 - 28 mm for Foc20E16, 16 - 32 mm for Foc40E16, 16 - 56 mm for Foc60E16 and 20 - 56 mm for Foc80E16, in the case of 16-element aperture, and 20 - 24 mm for Foc20E32, 32 - 48 mm for Foc40E32, 40 - 66 mm for Foc60E32 and 56 - 66 mm for Foc80E32 in the case 32-element aperture.

(ii) From the projections to the *x*-axis it can be seen that in the focal zone the beam widths of shallow focused beams are narrower and their amplitudes are larger than those of deeper focused beams; e.g., the narrowest beam width is about 2.27 mm for Foc12E16, 2.29 mm for Foc20E16, 3.05 mm for Foc40E16, 4.20 mm for Foc60E16, 4.58 mm for Foc80E16 in the case 16-element aperture, and 1.19 mm for Foc20E32, 2.25 mm for Foc40E32, 3.03 mm for Foc60E32 and 3.81 mm for Foc80E32 in the case 32-element aperture.

(iii) From the projections to the *z*-axis it can be seen that the axial resolutions, determined by the duration of pulse excitations, are almost the same in all cases.

In the case of the 16-element aperture, we see that the peaks at around 45 mm in depth reach local maximum. This is because the geometrical focusing remains quite strong. Whereas in the case of the 32-element aperture, the electronic focusing becomes stronger than in the former case. Therefore, that local maximum does not appear.

To examine how the aperture size impacts the focusing, we shall compare the results from the 16-element aperture shown in Fig. 2.2(b)-(e) and listed in table 2.1 with the corresponding ones from the 32-element aperture in Fig. 2.3(a)-(d) and listed in table 2.2. From the comparison, we can conclude

(i) that the larger the aperture, the sharper the focusing, namely the smaller the focal zone, because of the faster beam convergence to and the faster divergence off the focal point, e.g., the narrowest beam width is 2.29 mm for Foc20E16 *vs* 1.19 mm for Foc20E32, 3.05 mm for Foc40E16 *vs* 2.25 mm for Foc40E32, *etc*.

(ii) that the lager aperture give larger echo signal; the gains used was 8 dB for the 16-element aperture, and 3 dB for the 32-element aperture, to obtain the results in Figs. 2.2 and 2.3, respectively.

The results also show that the focusing in the near field region gives a sharper focal zone than the one in the far field region, and generates a focal zone at the position close to what expected from the focusing law, whereas the focal position for the far field focusing deviates from what expected, especially when an array has a curved surface used for focusing beams in elevation (the *y* direction). The conclusions made and the results obtained are all in agreement with the existing theory.

When conducting a inspection using an ultrasonic system, it is very helpful that we have knowledge about the behavior of beams as analyzed above. Thus, we can select beams best suitable for the

specified inspection. For example, the larger focal zone yields more uniform imaging (in comparison of Fig. 2.2(c) - (e) with Fig. 2.3(b) - (d)). Therefore, when a uniform imaging (especially in B-mode) is needed, the smaller aperture is better (of course the aperture must be large enough to maintain an acceptable lateral resolution). However, when sizing defects or acquire a C-scan gated in a short time interval, sharp focusing in the region of interest is demanded.

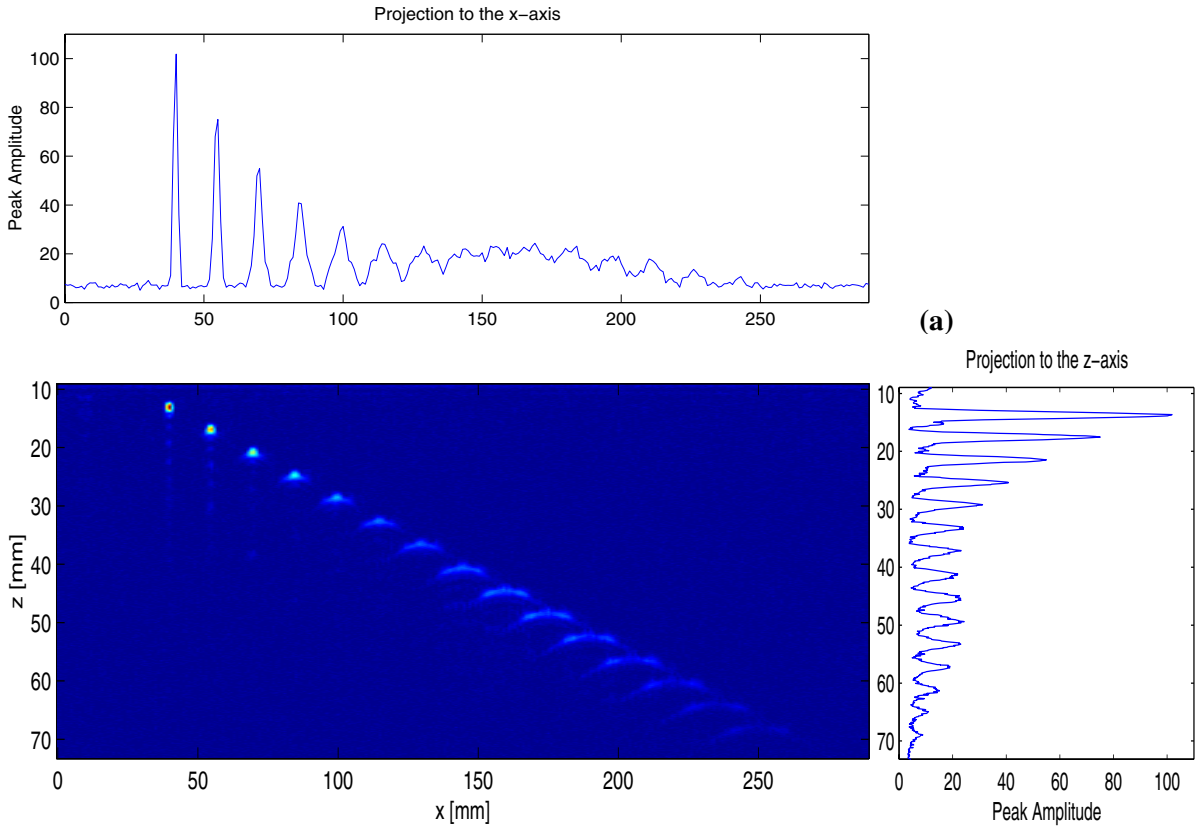

Fig. 2.2. The focused beams by the 16-element aperture into copper immersed in water. (a) - (e) the focal points are supposed to be located at 12, 20, 40, 60, and 80, respectively. The water path is 28 mm.

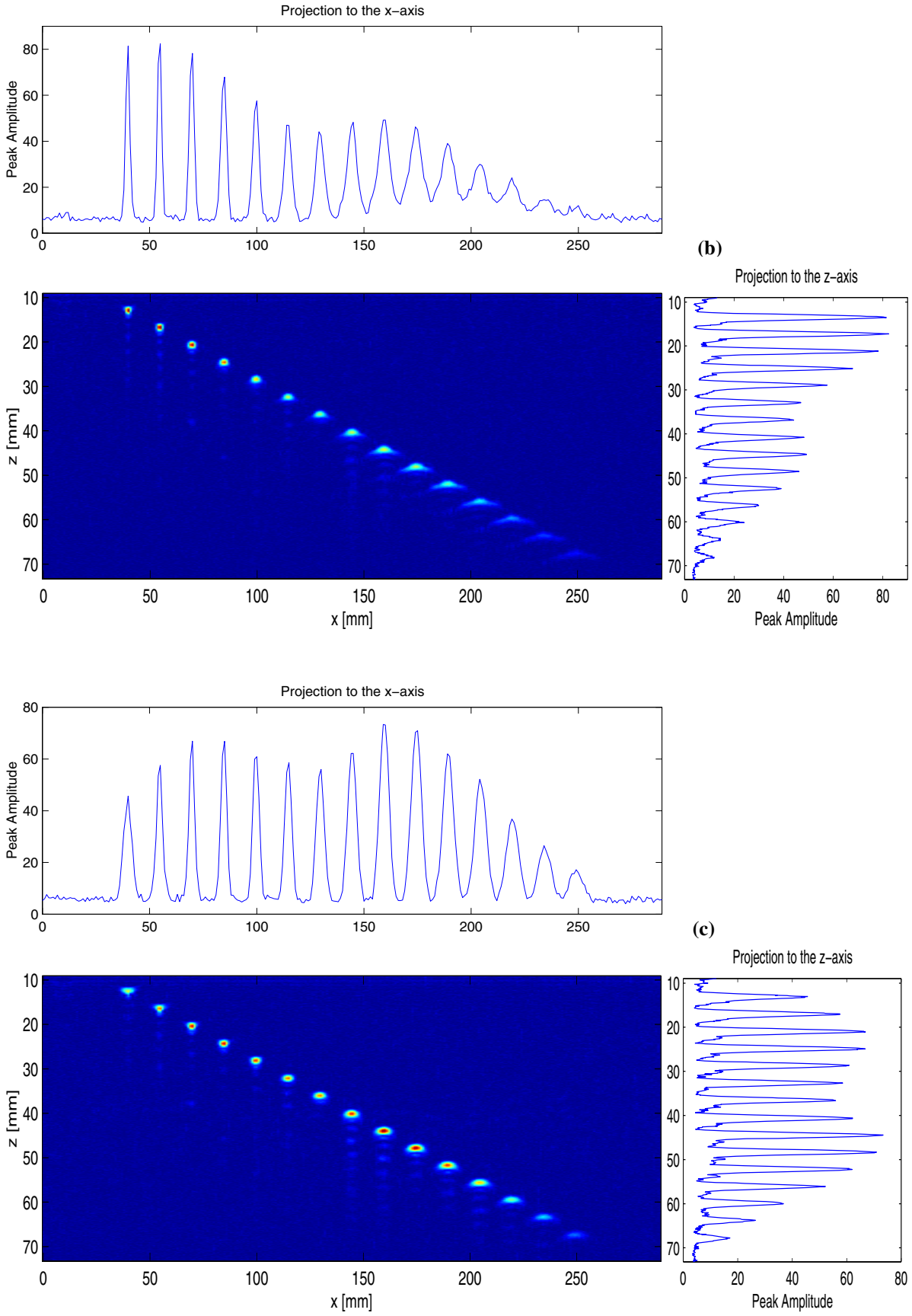

Fig. 2.2. The focused beams by the 16-element aperture into copper immersed in water. (a) - (e) the focal points are supposed to be located at 12, 20, 40, 60, and 80, respectively. The water path is 28 mm.

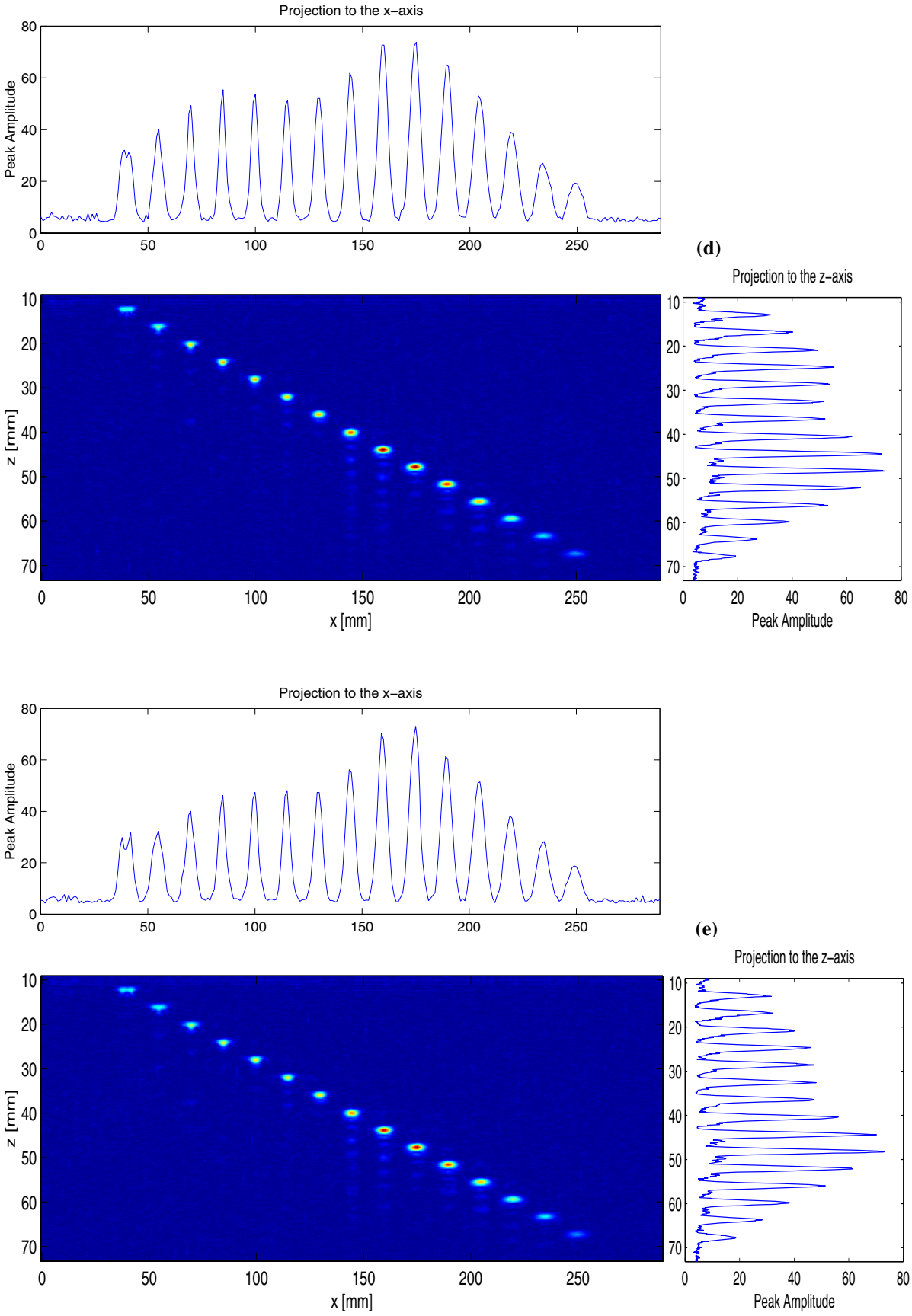

Fig. 2.2. The focused beams by the 16-element aperture into copper immersed in water. (a) - (e) the focal points are supposed to be located at 12, 20, 40, 60, and 80, respectively. The water path is 28 mm.

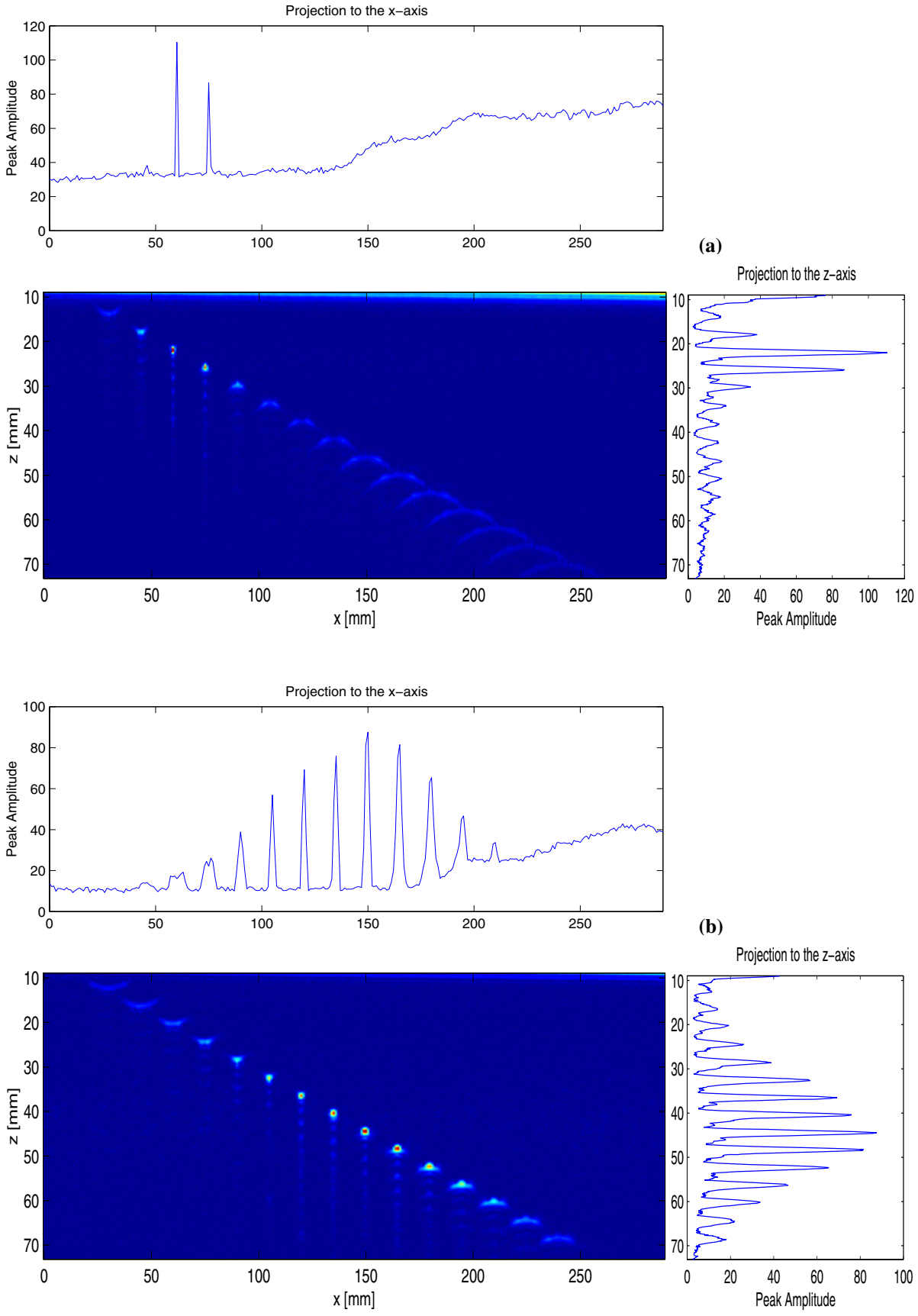

Fig. 2.3. The focused beams by the 32-element aperture into copper immersed in water. (a) - (d) the focal points are supposed to be located at 20, 40, 60, and 80, respectively. The water path is 28 mm.

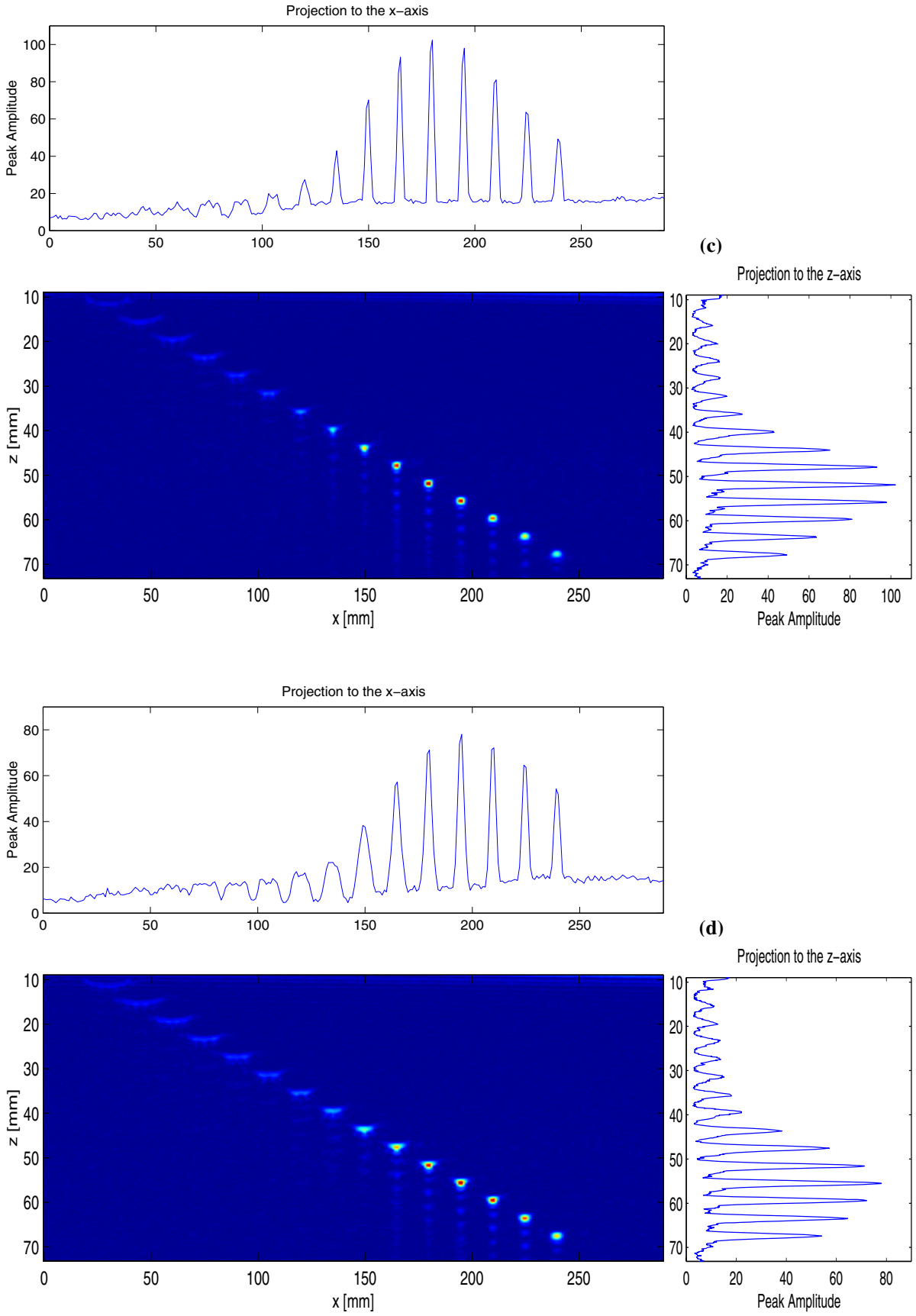

Fig. 2.3. The focused beams by the 32-element aperture into copper immersed in water. (a) - (d) the focal points are supposed to be located at 20, 40, 60, and 80, respectively. The water path is 28 mm.

Table 2.1 Amplitudes (Apeak in relative unit) and the -3 dB beam widths (BW, in mm) of the peaks in Fig. 2.2.

Depth	**Foc12E16**		**Foc20E16**		**Foc40E16**		**Foc60E16**		**Foc80E16**	
mm (*Hole*)	Apeak	BW	Apeak	BW	Apeak	BW	Apeak	BW	Apeak	BW
12 (*#3*)	101.88	**2.27**	81.42	**2.29**	45.68	**5.35**	32.06	**7.63**	31.63	**7.63**
16 (*#4*)	75.09	**2.29**	82.41	**2.67**	57.56	**3.05**	40.19	**5.34**	32.27	**7.26**
20 (*#5*)	54.99	**3.44**	78.22	**3.05**	66.91	**3.43**	49.30	**4.20**	40.06	**5.35**
24 (*#6*)	40.85	**4.93**	67.88	**3.44**	66.85	**3.44**	55.41	**4.20**	46.26	**4.58**
28 (*#7*)	31.25	**7.63**	57.57	**3.82**	60.90	**4.18**	53.61	**4.20**	47.38	**4.58**
32 (*#8*)	24.15	**10.68**	46.98	**4.58**	58.57	**4.18**	51.48	**4.58**	48.09	**4.58**
36 (*#9*)	23.20	**12.96**	44.10	**4.96**	55.99	**4.58**	52.09	**4.96**	47.36	**4.96**
40 (*#10*)			48.26	**5.72**	62.19	**5.34**	61.90	**4.96**	56.19	**5.34**
44 (*#11*)			49.24	**6.86**	73.37	**5.73**	72.70	**5.73**	70.20	**5.35**
48 (*#12*)			46.21	**8.39**	70.94	**6.11**	73.78	**6.11**	73.03	**5.73**
52 (*#13*)			39.00	**9.53**	62.01	**6.11**	65.04	**6.11**	61.28	**6.11**
56 (*#14*)			29.98	**13.35**	52.20	**6.49**	53.02	**6.49**	51.24	**6.87**
60 (*#15*)					36.81	**8.01**	38.99	**7.25**	38.27	**7.25**
62 (*#16*)					26.49	**8.01**	27.00	**7.96**	28.26	**7.63**
66 (*#17*)					17.20	**9.17**	19.32	**9.06**	18.79	**8.78**

Table 2.2 Amplitudes (Apeak in relative unit) and the -3 dB beam widths (BW, in mm) of the peaks in Fig. 2.3.

Depth	**- - -**		**Foc20E32**		**Foc40E32**		**Foc60E32**		**Foc80E32**	
mm (*Hole*)			Apeak	BW	Apeak	BW	Apeak	BW	Apeak	BW
12 (*#3*)										
16 (*#4*)										
20 (*#5*)			110.40	**1.14**						
24 (*#6*)			86.68	**1.90**	26.12	**7.25**				
28 (*#7*)					38.88	**4.20**				
32 (*#8*)					56.87	**2.25**				
36 (*#9*)					69.25	**2.28**	27.46	**6.44**	18.10	**9.51**
40 (*#10*)					75.97	**2.67**	42.95	**3.41**	22.14	**9.13**
44 (*#11*)					87.63	**2.67**	70.19	**3.41**	38.25	**7.22**
48 (*#12*)					81.52	**3.44**	93.23	**3.03**	57.26	**4.95**
52 (*#13*)					65.40	**3.82**	102.26	**3.03**	71.21	**4.19**
56 (*#14*)					46.71	**7.88**	97.96	**3.41**	78.05	**3.81**
60 (*#15*)							81.02	**3.41**	72.14	**3.81**
62 (*#16*)							63.69	**3.78**	64.58	**3.81**
66 (*#17*)							49.23	**3.79**	54.21	**3.82**

2.3 Resolution limits to defect sizing in the weld in a copper canister

Sec. 2.2 presented various beams focused at different depths in copper which were developed using the beamforming tool. In this section, we apply them to the inspection of the weld of a copper canister.

2.3.1 Copper canister CAN1 and experimental setup

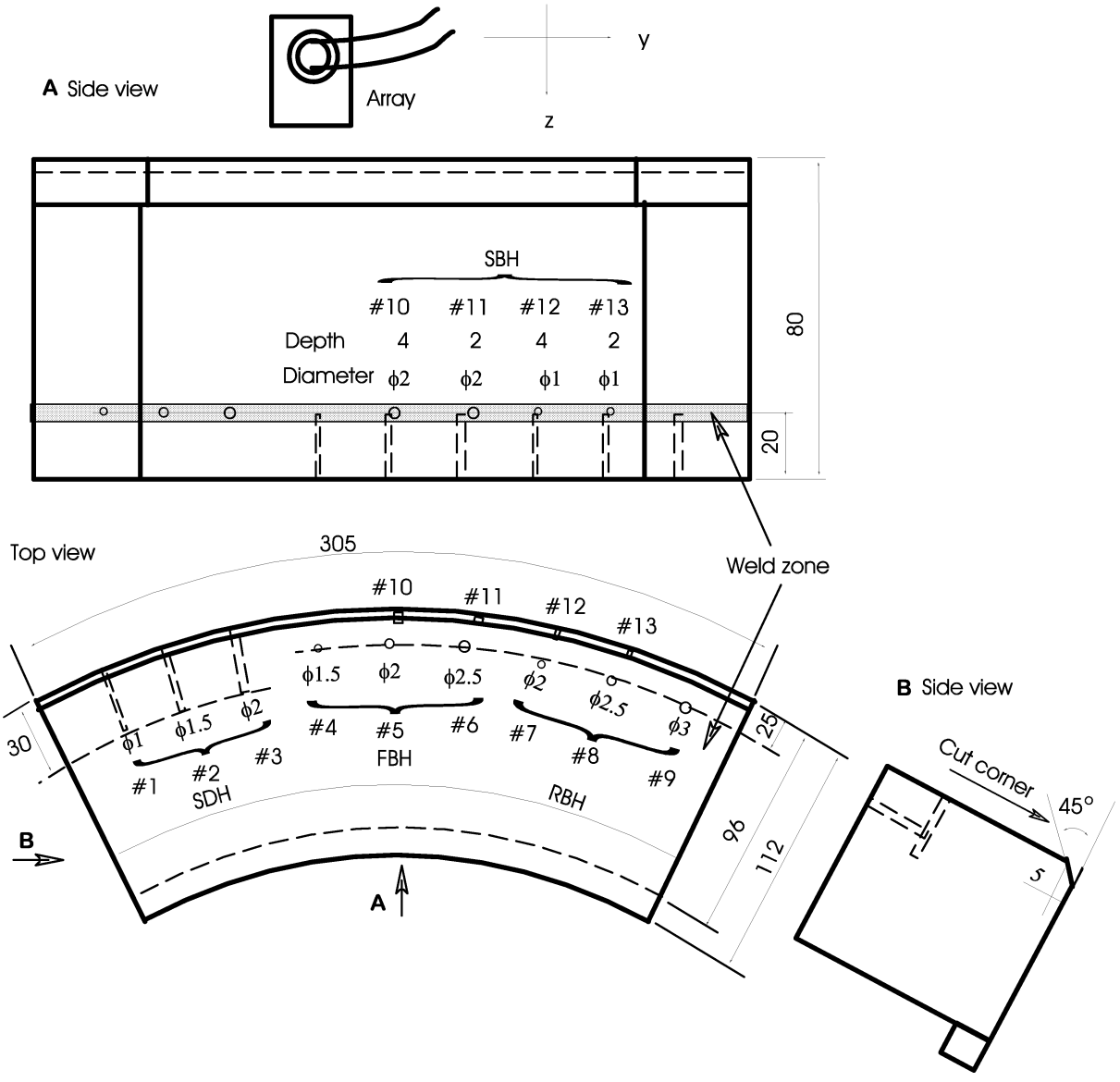

Fig. 2.4. Schematic of the copper canister CAN1 and the array for inspection of the weld in the canister.

Fig. 2.4 shows the schematic drawing of copper canister CAN1 and the experimental setup. The weld in the canister is located at 60 mm. In the weld, 13 holes were drilled, specifically, Three side drilled

holes (SDH, #1 - #3, and #10 - #13), three flat-bottom holes (FBH, #4 - #6), and three round bottom holes (RBH, #7 - #9). Here the six bottom-drilled holes are of our interest because the beam resolution is under investigation. Since the weld zone is a slice around at 60 mm deep in the canister, a suitable choice for defect sizing is a beam which has a good resolution in the zone and does not need a long focal zone in the *z* direction. Thus, we choose the beam produced by the 32-element aperture with focusing law Foc60E32. For the sake of comparison, we choose another focused beam which was produced by the 16-element aperture with focusing law Foc60E16. The array was put above the canister, and the water path is 28 mm long. The electronic scanning and mechanical scanning were performed along the *x* and *y* directions, respectively.

2.3.2 Measurements and discussions

The weld was inspected in C-scan by means of the two focused beams mentioned in Sec. 2.3.1. The gains used in the cases of 16- and 32-element apertures were 10 dB and 4 dB, respectively. The C-scan images of the weld obtained in the two cases are shown in Fig. 2.5 and 2.6, respectively.
Both Figs. 2.5 and 2.6 cover the six bottom-drilled holes (holes #4 - #9). Each of the figures shows a C-scan and the profiles along the *x* axis at the positions of six holes, i.e., at *y*=13, 40, 69, 97, 127, and 155 mm, respectively. In the figures, the three FBHs' are clearly seen, and two RBHs' (#7 and #9) are possible to recognize, but RBH #8 is difficult to see. In comparison of Figs. 2.5 and 2.6, we can say that the beam resolutions in the *y* direction in both cases are almost the same but those in the *x* direction differ quite a lot. That is, in the *x* direction, the resolution of the beam radiated by the 32-element aperture is much better than that by the 16-element aperture. A more exact evaluation of the beam resolutions can be made from the profiles in the figure. The -3 dB widths of the peaks were measured which corresponded to the echoes from FBHs #4, #5 and #6. They are 7.03, 6.24 and 6.90 mm, respectively, in the case of 16-element aperture with Foc60E16, and 3.40, 3.48 and 4.09 mm, respectively, in the case of 32-element aperture with Foc60E32. From the measured data, we see that the resolution in the latter case is two times high as the one in the former case. Therefore, for defect sizing in the weld zone, a larger aperture yields better performance.

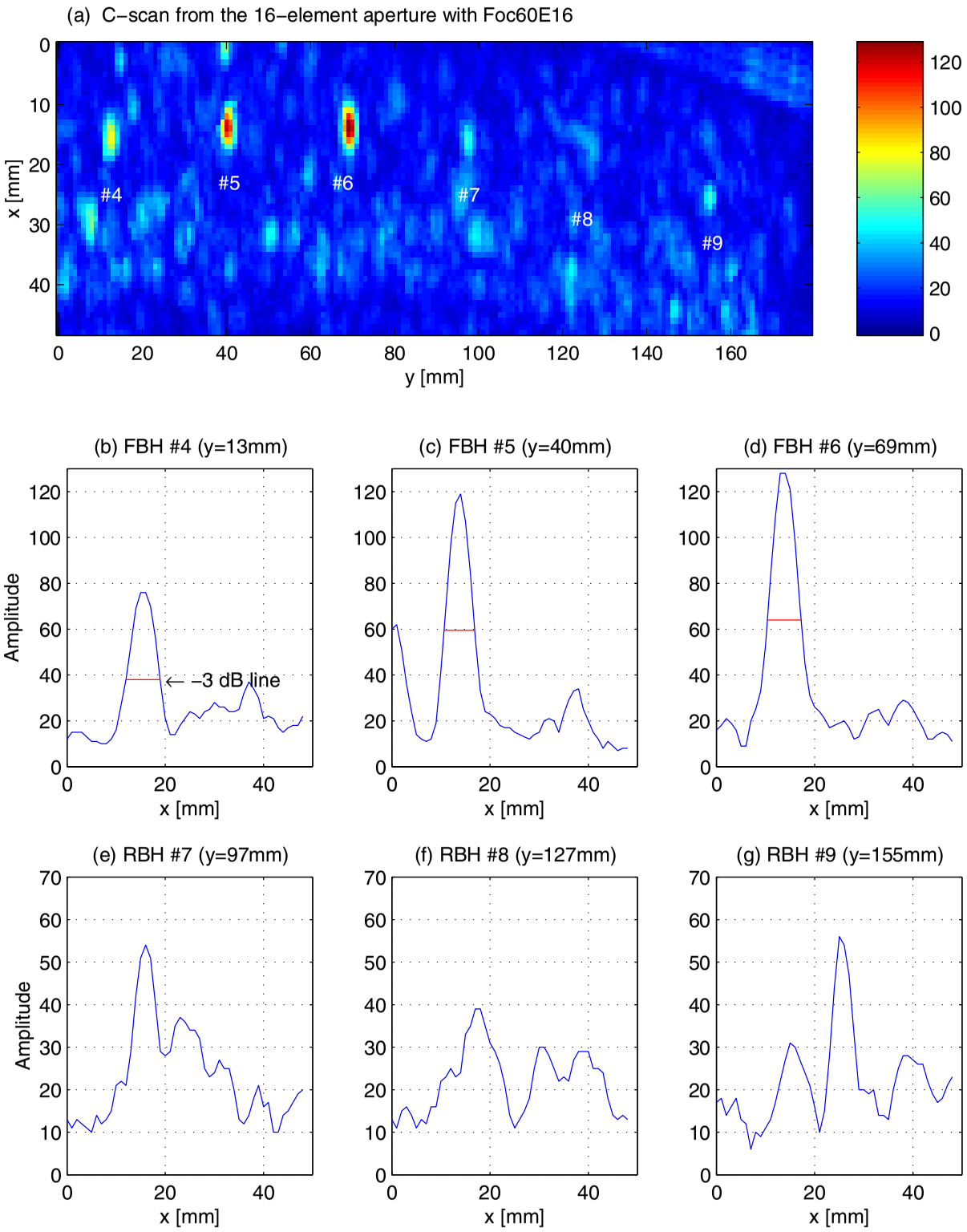

Fig. 2.5. C-scan of the weld zone obtained from the 16-element aperture with Foc60E16 (a), and its profiles (b)-(g) along the *x* axis at *y*=13, 40, 69, 97, 127, and 155 mm, respectively. The water path is 28 mm. The -3 dB widths of peaks in profiles (b) - ((d) showing the strengths of echoes from FBH #4, FBH #5 and FBH #6 are 7.03, 6.24 and 6.90 mm, respectively.

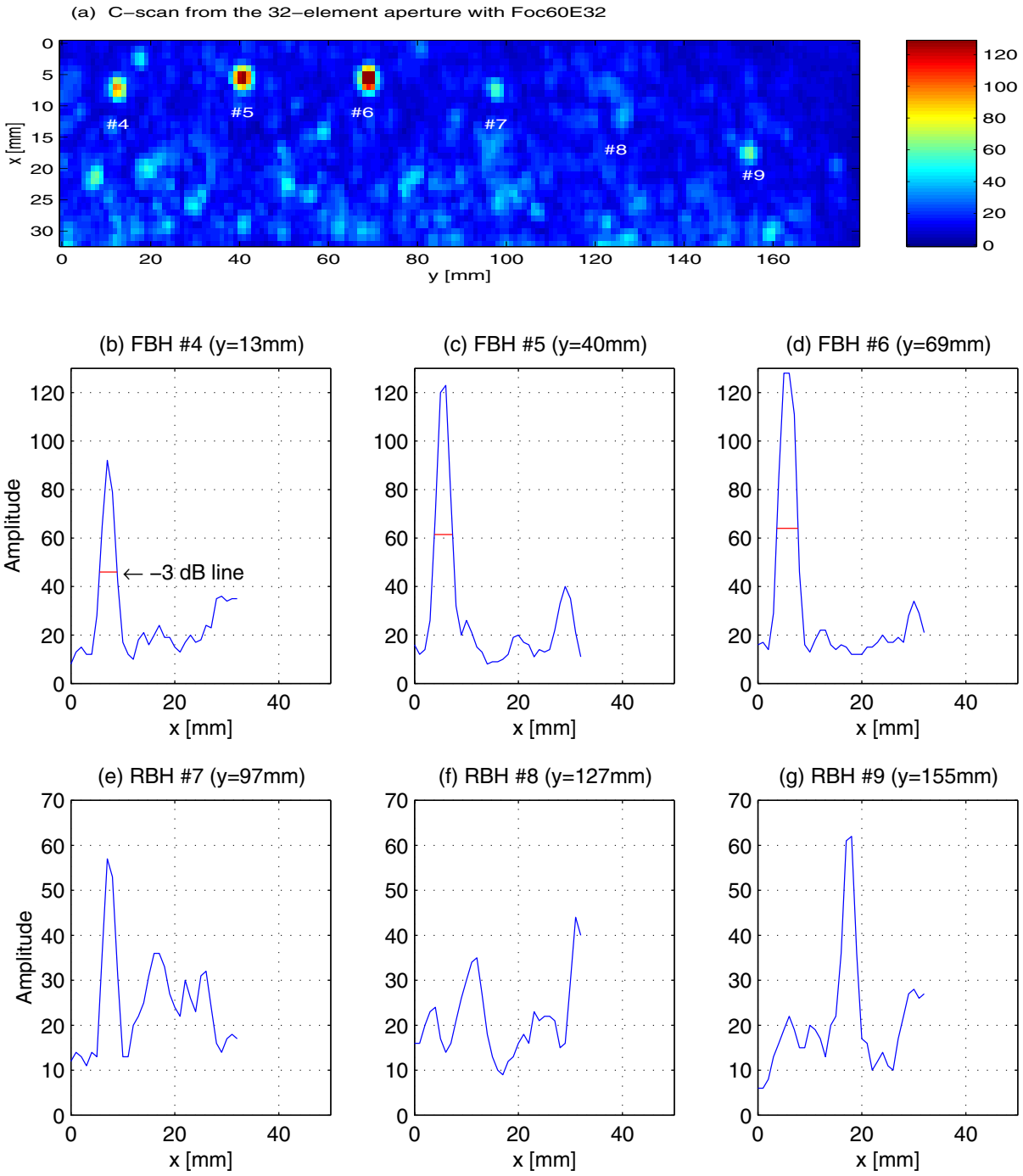

Fig. 2.6. C-scan of the weld zone obtained from the 32-element aperture with Foc60E32 (a), and its profiles (b)-(g) along the *x* axis at *y*=13, 40, 69, 97, 127, and 155 mm, respectively. The water path is 28 mm. The -3 dB widths of peaks in profiles (b) - ((d) showing the strengths of echoes from FBH #4, FBH #5 and FBH #6 are 3.40, 3.48 and 4.09 mm, respectively.

2.4 Detection of defects close to the outer wall of copper blocks and canisters

Very often the zones close to the outer wall of a material are difficult or even impossible to inspect if normal incident beams are used in the inspection. The reason for this can be the constraint of the geometry of an inspected material and the limitation due to diffraction. In our case, the cut corner of the copper canister CAN1 (see Fig. 2.4) results in total reflection of the incident beams, and thus the zone close to the outer wall is impossible to inspect by means of normal incident beams. In the case of a straight corner, the zones close to the outer wall are only insonated by part of the beam. To overcome this difficulty, we use angle beams for such inspections. The angle beams can be easily generated by the ALLIN array system. For better inspection performance, angle beams need to be focused. The beamforming tool developed and presented in Sec. 1.2 is applied here to optimize the beams.

Using steered beams, we performed experiments on a special copper block with flat bottom holes close to the outer wall, and on two copper canister segments with shallow side-drilled holes located in weld zones.

2.4.1 Detection of defects close to the outer wall of copper block CU3

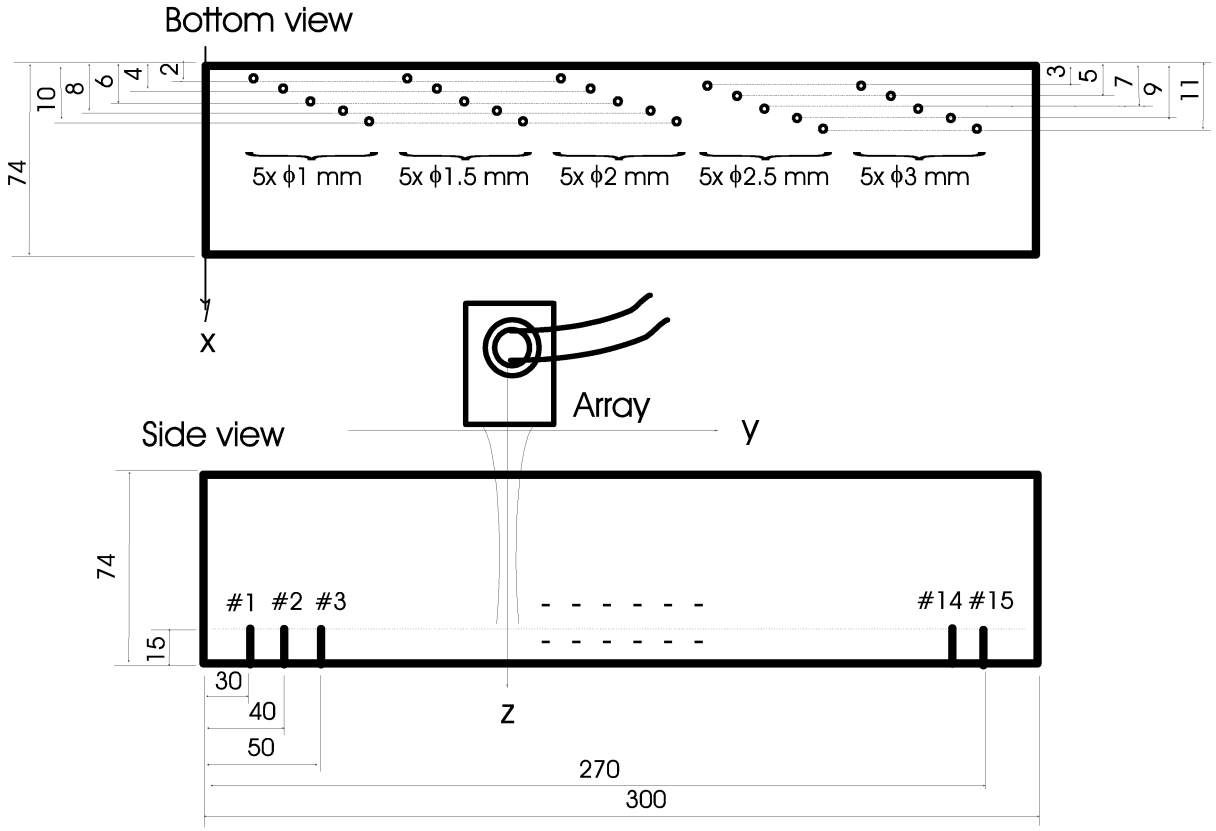

Fig. 2.7. Geometry of the copper block and the array for measuring the ultrasonic fields in the block.

2.4.1.1 Copper block CU3 and experimental setup

A copper block was designed specially for the investigation of the detection limits for defects located close to its outer wall, and it was named CU3. As shown in Fig. 2.7, the block has five sets of FBHs. Each set consists of five holes of the same diameter. The holes are 15 mm deep from bottom (approximately 60 mm deep from the upper surface) and their distances from the outer wall vary uniformly. The five holes in the first set to the fifth set are 1, 1.5, 2, 2.5 and 3 mm in diameter, respectively. The centers of the holes closest to the outer wall in the first, second and third sets are all 2 mm from the wall, and those in the forth and fifth sets are 3 mm from the wall.
The array performed electronic scanning along the x direction and mechanical scanning along the y direction. The water path was always 35 mm long.

2.4.1.2 Measurements and discussions

In measurements, we used nonfocused and focused beams which were steered at various angles. The nonfocused beams were steered at 0, 1, 2, 3, 4 and 5 degrees towards the outer wall, respectively, and the focused beams were all designed to be focused at 60 mm deep into the block and were steered at 0, 2, 3, and 5, 8, 10 and 12 degrees towards the outer wall, respectively. Here we present some of the measured results. Fig. 2.8 shows C-scan images of FBHs obtained by using nonfocused beams steered by 0, 2, 3 and 5 degrees, respectively. Fig. 2.9 shows C-scan images of FBHs obtained by using focused beams steered by 0, 5, 8 and 12 degrees, respectively. Obviously, both figures indicate that larger holes give larger echoes (backscattering). Comparing the results from the nonfocused beams (Fig. 2.8) with those from the focused beams (Fig. 2.9), we see that the beam resolutions of the focused beams are all better than those of the nonfocused beams.
Let us investigate the results obtained from the normally incident beams and the steered ones. In Fig. 2.8(a) showing the result from the nonfocused, normal incident beam, FBH #1 is not visible, and FBHs #5, and # 11 are hardly seen, but the remaining holes are clearly visible. In Fig. 2.8(b)-(d) showing the result from the nonfocused beams steered by 2, 3 and 5 degrees, respectively, all the FBHs are easily seen. When using focused beams, normally incident or steered, the results in Fig. 2.9(a)-(d) show that all holes are clearly seen. From this observation, we should focus ourselves on holes FBHs #1, #5 and # 11, because the remaining holes are clearly visible in all cases. These three holes are 1, 1.5 and 2 mm large in diameter, and closest to the outer wall (to which their centers are 2 mm). We can conclude that such FBHs that are so small as 1mm in diameter and 2 mm close to the outer wall are detectable using steered beams, and that the use of focused beams improves the ultrasonic inspection performance. The best result obtained is the one in Fig. 2.9(b) showing the case when the focused beam steered by 5 degrees was used. This indicates that a proper angle used for steering a beam also needs to be considered in beam design.

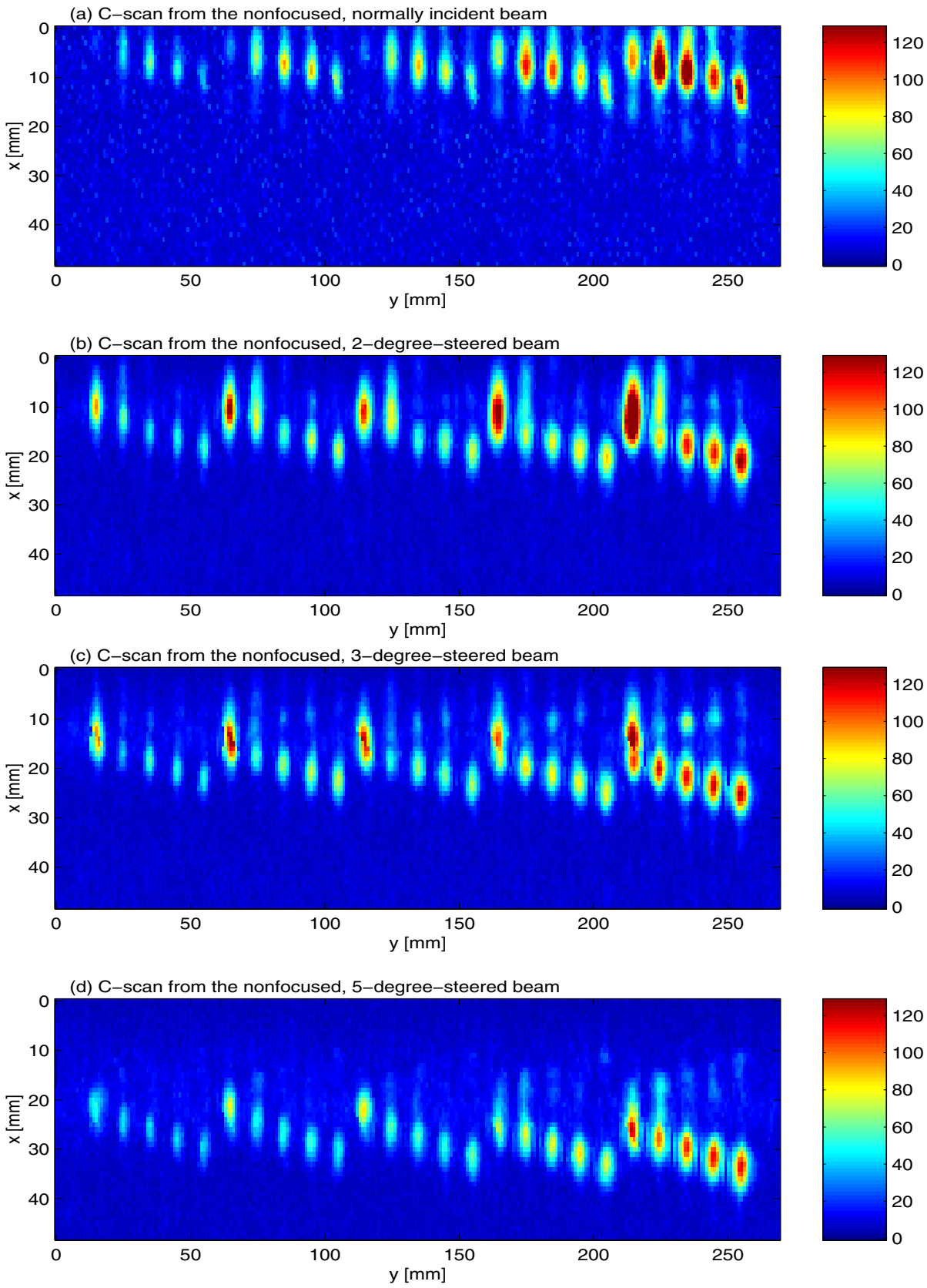

Fig. 2.8. C-scan imaging of bottom-drilled holes by using nonfocused beams steered by (a) 0 degree, (b) 2 degrees, (c) 3 degrees and (d) 5 degrees.

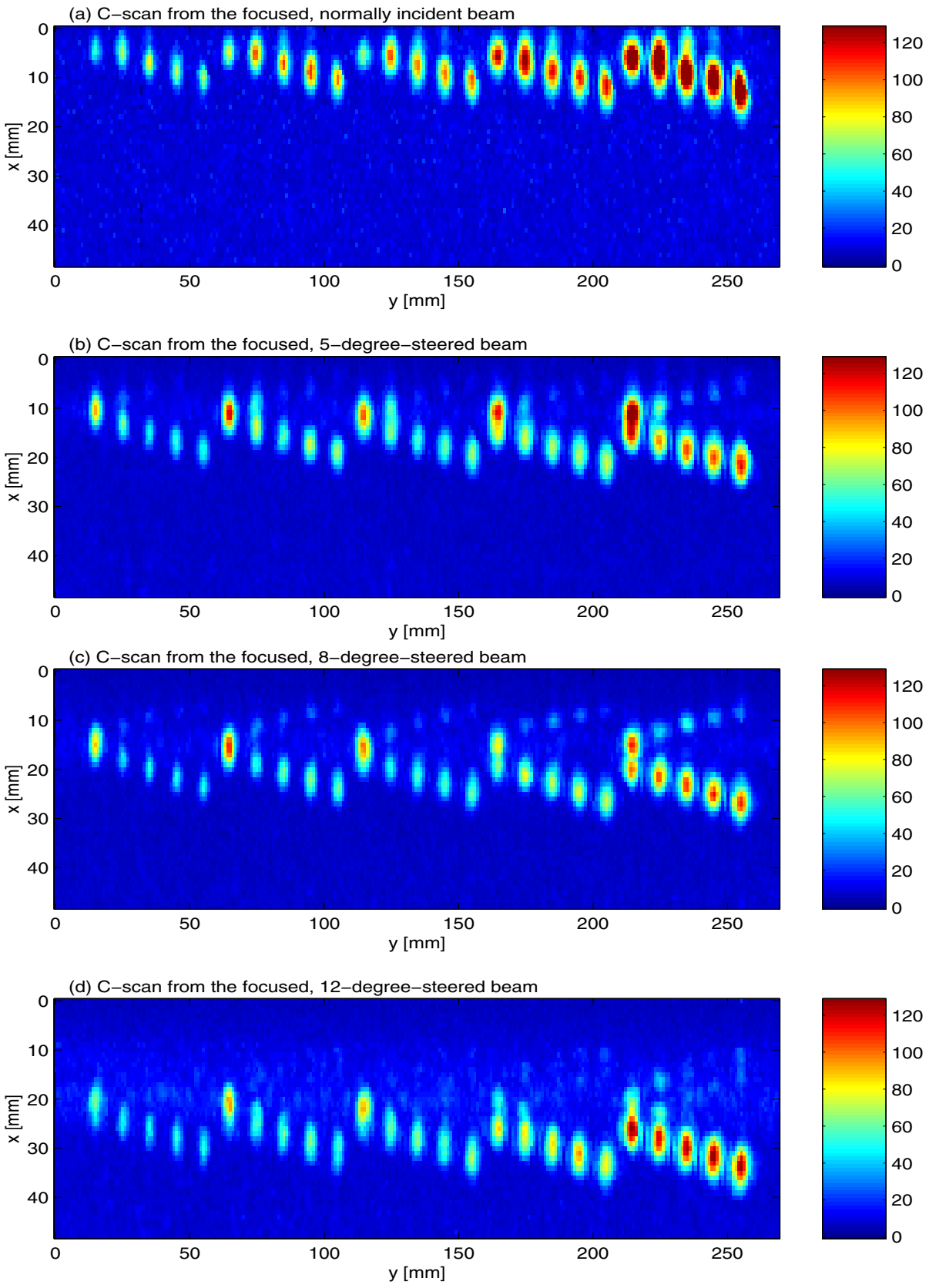

Fig. 2.9. C-scan imaging of bottom-drilled holes by using focused beams steered by (a) 0 degree, (b) 5 degrees, (c) 8 degrees and (d) 12 degrees.

2.4.2 Detection of defects in the weld and close to the outer wall of copper canister CAN1

2.4.2.1 Copper canister CAN1 and experimental setup

Let us go back to Fig. 2.4 that shows drawing of the copper canister CAN1. Due to the existence of a cut corner, the weld zone close to the outer wall of a copper canister could not be inspected using a normal incident beam (see Fig. 2.10(a)). Due to the presence of strong structure noise scattered from the weld, the defects in the weld are difficult to distinguish from the structure noise. Therefore, the use of focused, angle beams becomes necessary for the inspection of the weld zone close to the outer wall. To investigate the limits of detection of defects in the weld zone close the outer wall, we used canister CAN1 with four side-drilled holes, two with diameter 2-mm diameter (SDH #10 and #11) and two with 1-mm diameter (SDH #12 and #13). SDHs #10 and #12 are 4 mm deep, and SDHs #11 and #13 are 2 mm deep.

The array performed electronic scanning along the x direction and mechanical scanning along the y direction. The water path was 28 mm long.

2.4.2.2 Measurements and discussions

In measurements, the beams used were steered by 0, 3, 5, 8, 10 and 12 degrees, respectively. All the beams used were focused and the focal points were located at 60 mm in the canister, corresponding to the depth of the weld zone. C-scans obtained using different angle beams are shown in Fig. 2.10. In the case of normal incident beam (Fig. 2.10(a)), the holes (SDHs #10 - #13) of interest are not visible at all; for the beam steered by 2 degrees, SDHs # 10 and #12 can be seen, but SDHs # 11 and #13 still do not appear; for the beam angle of 5 degrees, SDH # 11 comes out, but SDH #13 is still not distinguishable. When the beam was steered by 8 degrees, SDH #13 appears. Finally, as the beam was steered by 10 and 12 degrees, the echoes from SDHs #11 and #13 become stronger. From these experiments, we conclude that the side-drilled holes which are as large as 2 mm in diameter and 4 mm deep are impossible to detect by using a normal incident beam, but they can be seen using steered beams with properly large angles (e.g., 8 - 12 degrees). Therefore, the use of angle beams is an effective solution to the inspection of the weld zone close to the outer wall of canisters with cut corners.

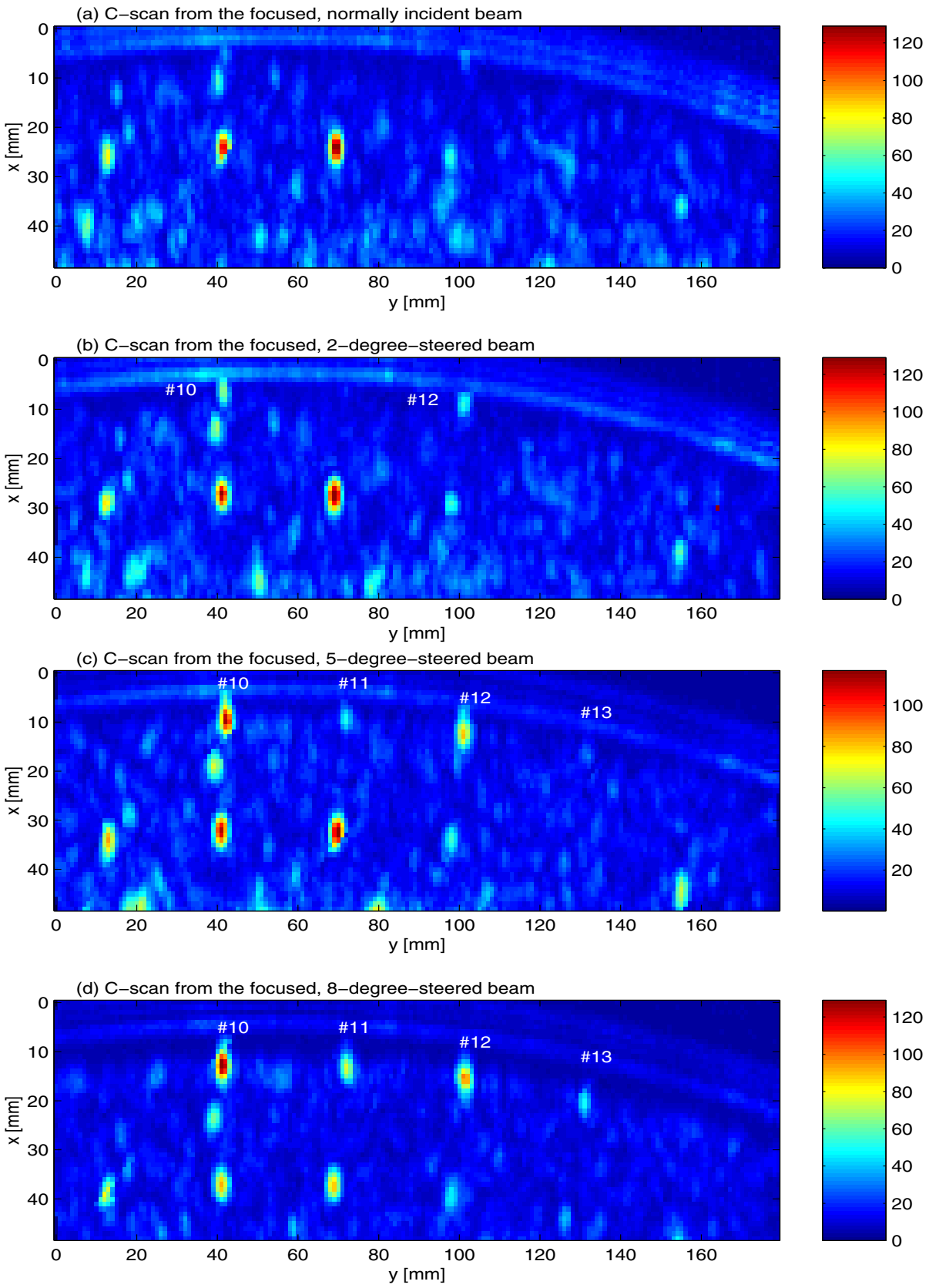

Fig. 2.10. C-scan imaging of the weld in copper canister CAN1 by using focused beams steered by (a) 0 degree, (b) 3 degrees, (c) 5 degrees, (d) 8 degrees, (e) 10 degrees and (d) 12 degrees, respectively.

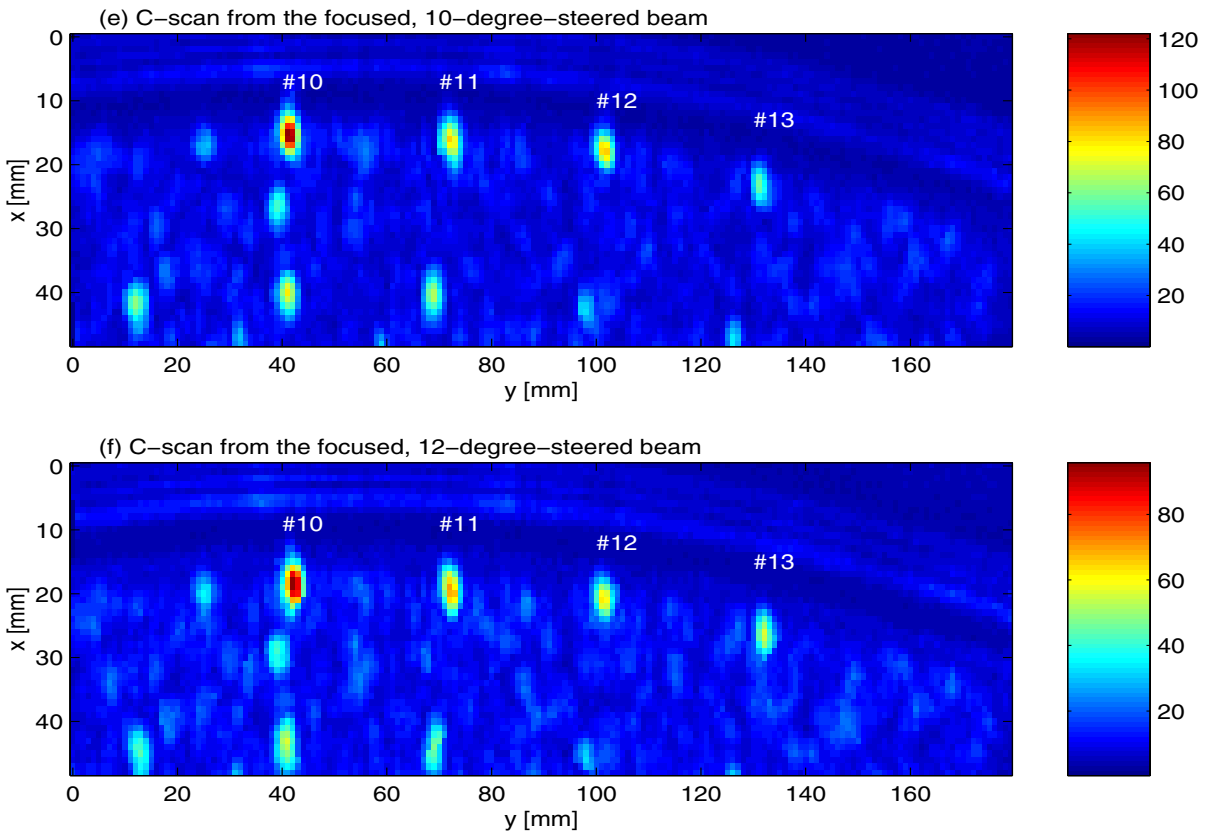

Fig. 2.10. C-scan imaging of the weld in copper canister CAN1 by using focused beams steered by (a) 0 degree, (b) 3 degrees, (c) 5 degrees, (d) 8 degrees, (e) 10 degrees and (d) 12 degrees, respectively.

2.4.3 Detection of defects in the sectioned weld W123 close to the outer wall of a copper canister

2.4.3.1 Weld W123 in copper canister BLOCK1 and experimental setup

Here we inspect one of five sections of a copper canister weld W124. We chose one of the five segments denoted BLOCK1 that has natural flaws and two side-drilled holes in the weld zone (see Fig. 2.11). Both SDHs #1 and #2 have 1.5-mm diameter but different depths. SDH #1 is 2 mm deep and SDH #2 is 3 mm deep. Since BLOCK1 does not have the cut corner like canister CAN1, the SDHs #1 AND #2 should be easier to detect. In experiments, we used the same beams as in Sec. 2.4.2 to inspect the weld zone close to the outer wall. The experimental setup used was the same as in Sec. 2.4.2.

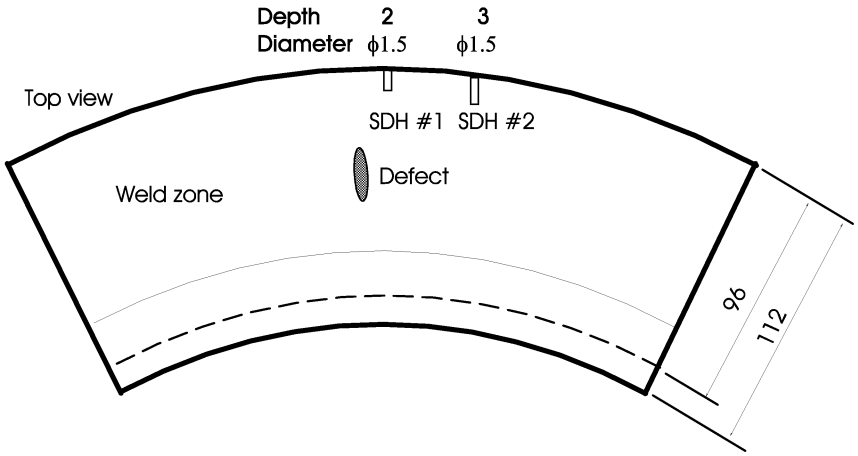

Fig. 2.11. Schematic drawing of weld W123 in copper canister segment BLOCK1.

2.4.3.2 Measurements and discussions

The results obtained by using the focused beams steered by 0, 3, 5, 8, 10 and 12 degrees are shown in Fig. 2.12(a)-(f), respectively. In the case of normal incident beam, SDH #1 is invisible and SDH #2 is difficult to distinguish from the structure noise scattered from the weld (see Fig. 2.12(a)). When the beam was steered by 2 degrees, SDH #1 was still invisible and SDH #2 looks slightly stronger (Fig. 2.12(b)). SDH #2 is clearly seen for the beams steered by 5 degrees or larger. SDH #1 can not be seen until the beam was steered by 10 degrees (Fig. 2.12(b)-(e)), and it is clearly visible for the beam steered by 12 degrees (Fig. 2.12(f)). In comparison of the results in the present experiments with those in Sec. 2.4.2, we can find that the existence of cut corners in a canister makes it more difficult to detect the defects in the weld close to the outer wall. From analysis of these experiments, we can make similar conclusions to those made in Sec. 2.4.2.

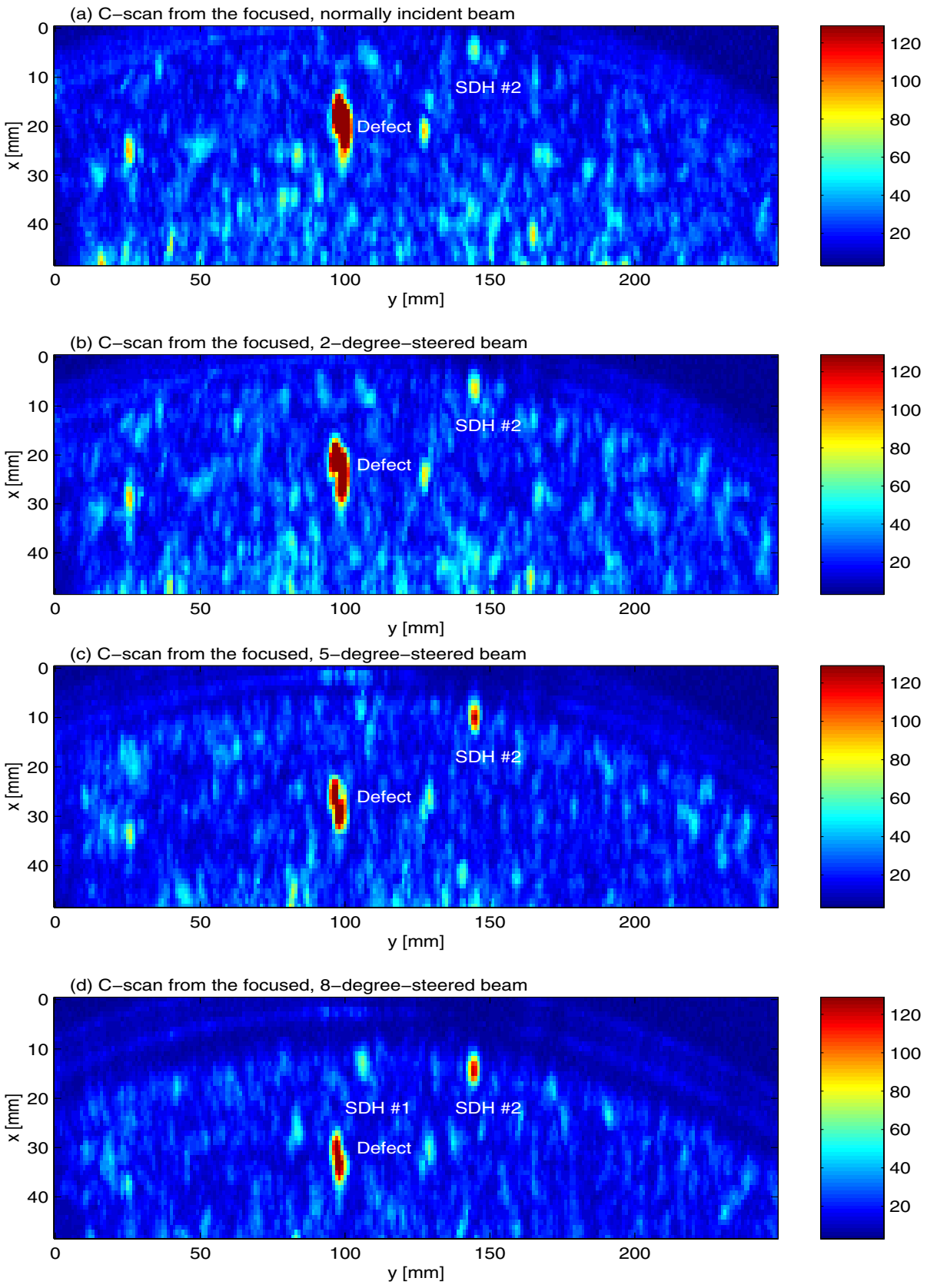

Fig. 2.12. C-scan imaging of weld W123 in copper canister segment BLOCK1 by using focused beams steered by (a) 0 degree, (b) 3 degrees, (c) 5 degrees, (d) 8 degrees, (e) 10 degrees and (d) 12 degrees, respectively.

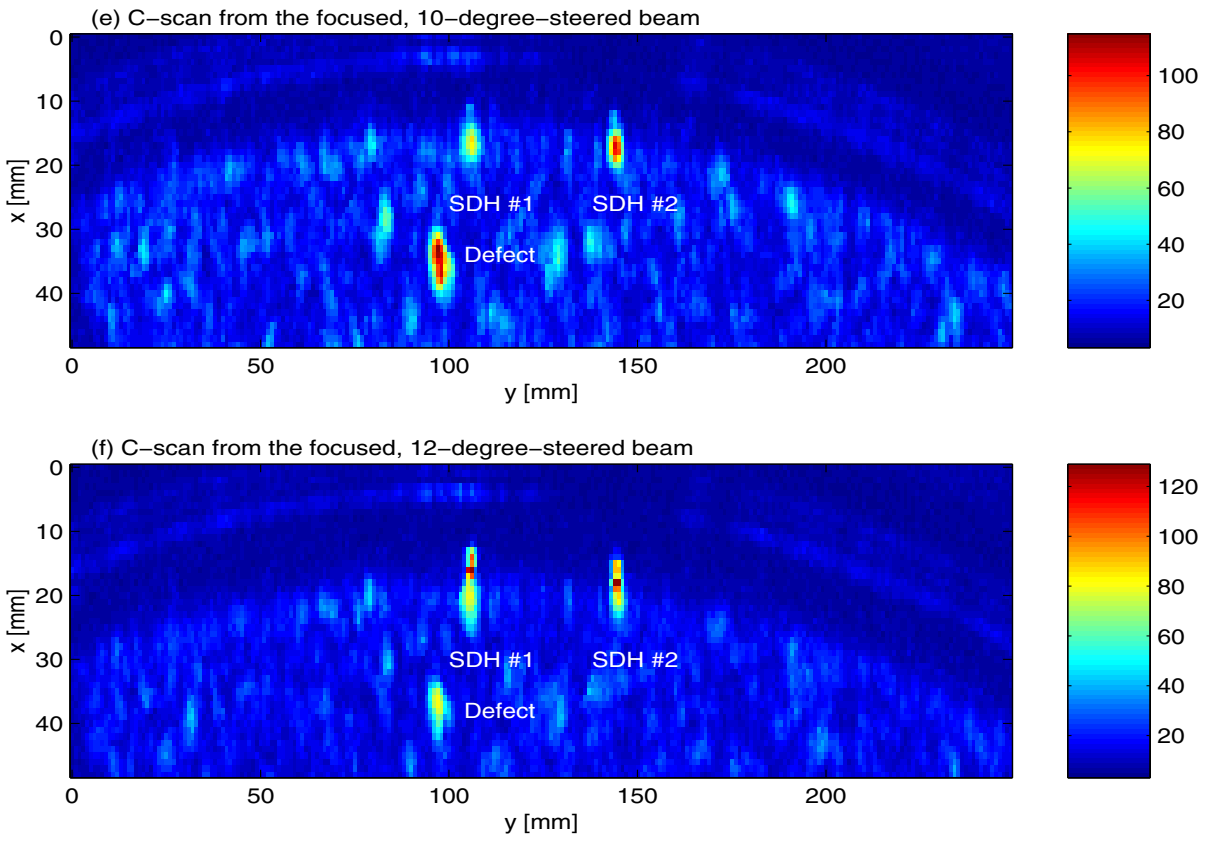

Fig. 2.12. C-scan imaging of weld W123 in copper canister segment BLOCK1 by using focused beams steered by (a) 0 degree, (b) 3 degrees, (c) 5 degrees, (d) 8 degrees, (e) 10 degrees and (d) 12 degrees, respectively.

2.5 Conclusions

Detection and resolution limits have been investigated based on a series of experiments. The results of the experiments coincide with theory.

First, the beamforming tool developed and presented in Sec. 1.2 has been applied to design (electronically) focused beams for the ALLIN array system to make immersion inspection of copper canisters. Beams focused at different depths have been tested on a copper test block. The results showed that the focusing in the near field region gives a sharper focal zone than the one in the far field region, and generates a focal zone at the position close to what expected from the focusing law, whereas the focal position for the far field focusing deviates from what expected, especially when an array has a curved surface used for focusing beams in elevation (the y direction). Also from the results, it follows (i) that the larger the aperture, the sharper the focusing, namely the smaller the focal zone, because of the faster beam convergence to and the faster divergence off the focal point, and (ii) that the larger focal zone yields more uniform imaging (in comparison of Fig. 2.2(c) - (e) with Fig. 2.3(b) - (d)).

By choosing to use an optimal beam from the specified inspection (e.g., from the fact that the welds were inspected in C-scans gated in a short time interval), the weld in a copper canister with artificial defects (like flat- and round-bottom holes) located in the weld zone has been inspected. The results showed that the larger aperture yields better performance of defect sizing in welds because of better beam (lateral) resolution.

secondly, the beamforming tool has been applied to design focused and steered beams for inspection of zones close to the outer walls of materials. A copper block CU3 which has bottom-drilled holes of various diameter and various distance to the outer wall has been inspected by using focused beams which were steered by various angles. The welds of two copper canister segments with side-drilled holes that are shallow to the outer wall have been examined with focused, steered beams. One of the canister segments, CAN1, has a cut corner joining the top surface and the outer wall surface. These experiments have demonstrated that use of focused, steered beams is an very effective solution to the inspection of the zone close to the outer walls of copper canisters, and they have also indicated that the angle which a beam is steered needs be properly large.

2.6 References

[1] T. Stepinski, and P. Wu, *Ultrasonic Inspection of Nuclear Copper Canisters*, SKB Projektrapport 97-01, December 1996.

[2] T. Stepinski, and P. Wu, *Ultrasonic Inspection of Nuclear Copper Canisters*, SKB Projektrapport 97-08, August 1997.

3 Evaluation of attenuation, and estimation and suppression of grain noise

3.1 Introduction

Crystals, known as grains, in a polycrystalline metal can be assembled in differing amounts and configurations to form microstructure [1]. Grains are the smallest structural units that are observable with ordinary light microscopy. In general, these grains are of various shapes and sizes, filling all space within the boundaries of the metals, they can be deformed elastically and plastically, dislocated, and have random orientations. Therefore, metals are random (polycrystalline) media. Scattering by inhomogeneities or, in the case of polycrystals, by randomly oriented grains, brings about "apparent" attenuation of progressive waves and in turn their dispersion [2]. The metals commonly used in engineering are basically anisotropic. This results both from the structure of materials and from the degree of anisotropy within individual crystals. For example, orientation distribution (texture) of grains in the polycrystalline aggregates can be preferred in some direction, and thus a textured polycrystalline material is elastically anisotropic [3-5].

Copper is a kind of polycrystalline metal, a random medium characterized by attenuation, dispersion, and anisotropy [2,4]. Our previous work has dealt with detecting and imaging defects in copper canisters and with simulation of propagation of elastic waves in copper which was treated as an isotropic solid without attenuation and scattering [6,7]. Presently, we will extend our work and investigate attenuation and scattering in copper. Dispersion and anisotropy, although occurring when ultrasound travels in polycrystalline metals, is not of our present interest.

Scattering and attenuation occur when an ultrasound travels through a metal, and the scattering and attenuation vary with the properties of materials. Due to this, both scattering and attenuation (and also ultrasound velocity which, however, is not considered here) have been employed to characterize the microstructure of metals [8-10]. It is assumed here that because the crystallites in a metal are relatively small and usually almost randomly arranged, this underlying structure does not normally influence ultrasonic propagation in MHz range and these materials are therefore regarded as being isotropic (of course, this assumption will lead to a certain amount of error in the modeling and evaluation of ultrasonic attenuation and ultrasonic grain noise in polycrystalline metals) [5]. Because of the grain structure of a polycrystalline metal, the grains act as irresolvable scatterers that produce the coherent interference. The coherent interference results in grain noise in ultrasonic A-scan and B-scan signals [11]. From the point of view of the defect detection, grain noise is unwanted because it masks defect signals [12-14]. Whereas, from the point of view of the material characterization, grain

noise is a useful signal containing the information about the microstructure of materials [15-17]. This indicates that there is much more information present in an ultrasonic signal than the simple absence or presence of a defect.

A large amount of work has been done for material characterization by making use of ultrasonic attenuation and scattering, and a big body of literature on this subject is available. Ultrasonic attenuation and scattering in polycrystalline materials have been investigated both experimentally [18-25] and theoretically [26-29]. For quantitative estimation of attenuation, the effects of diffraction has to be considered [30,31]. Since the advent of pulse-echo technique, ultrasonic backscattering has been employed for predicting grain noise related to material's properties [7,15-17,32-37]. A review of the models for ultrasound backscattering was also given in detail in [7].

In the present work, ultrasonic attenuation and scattering are investigated theoretically and experimentally. Although attenuation and scattering are closely related to each other, they can be used to deal with different problems.

This chapter is arranged in the following way. Starting from propagation of plane waves in attenuating media, the fundamentals for evaluation of attenuation are introduced. Then, two commonly used methods, i.e., the log-spectral difference and spectral shift methods [38-40], are briefly presented which can be used to evaluate attenuation coefficients by using reflection echoes. The two methods were applied to the evaluation of attenuation of three copper specimens.

For evaluation of grain noise, two statistical models, i.e., the independent scattering model (ISM) proposed by Margetan *et al* [32-34] and the K-distribution model [7], are used.

Starting from the motion equation governing propagation of elastic waves in inhomogeneous media and then following Rose [35-37], we give the derivation of fundamental formulation for the ISM. This yields better understanding and properly applying the ISM to the evaluation and to interpretation of deviation of predicted results from the measured ones. Evaluation of grain noise in the three copper specimens is conducted. The theory on the K-distribution model was presented in our previous report [7]. Here the model is applied to evaluate grain noise from welds in copper canisters and to find the connection between grain noise and microstructure of the welds, and also applied to detect defects in the welds.

To suppress structure noise in weld, formerly developed frequency diversity technique, the noncoherent detector (NCD), has been applied. A novel technique based on the concept of spatial diversity has been proposed for the suppression of noise in the weld zone. The spatial diversity is realized by using a set of beams steered at different angles by the array.

3.2 Evaluation of ultrasonic attenuation in polycrystalline metals

3.2.1 Ultrasonic attenuation in polycrystalline metals

As an ultrasound travels in a polycrystalline metal, it attenuates. Numerous experiments have shown that the attenuation is sensitive to the grains, inclusions, pores, grain boundaries, twin boundaries, interphase boundaries, dislocations, substitutional impurities of a material. In general, ultrasonic attenuation in a medium may be classified into types [10]. One is the scattering attenuation due to the scattering from discontinuities such as grain boundaries and inclusions. The other is the absorption attenuation caused by thermoelastic loss, dislocation motion, and mechanical hysteresis [10,22,23,41, 42]. The mechanism of attenuation is given in details in [22,23]. As a measure of the attenuation, an attenuation coefficient is used and written as [43,44]

$$\alpha(f) = \alpha_s(f) + \alpha_a(f) \tag{3.1}$$

where α_s and α_a represent the scattering and absorption attenuation coefficients, respectively, and they are dependent on frequency *f*. The attenuation coefficient contains information about absorption and scattering processes occurring in a material, and is related to the properties of the material. Therefore, ultrasonic attenuation has become a very valuable tool for the study of the properties of materials.

The attenuation of a polycrystalline material in most cases is determined almost entirely by scattering from grains [21-23], that is

$$\alpha(f) \approx \alpha_s(f)\,. \tag{3.2}$$

3.2.2 Evaluation of acoustical attenuation by means of plane waves

A. Continuous plane waves in a homogeneous attenuating medium

Plane waves with angular frequency $\omega = 2\pi f$ travelling through an unbounded medium (fluid) can be expressed as, in terms of pressure (for simplicity $\exp(-j\omega t)$ is omitted and $\alpha(f)$ is abbreviated as α in sequel)

$$p(r) = p_0 \exp\left(j\mathbf{k}\cdot\mathbf{r}\right) \tag{3.3}$$

where p_0 is an initial amplitude at $r = 0$, and $\mathbf{k}$ is the wave vector. For a attenuating medium, $\mathbf{k} = k\hat{\mathbf{k}}$ is complex, its magnitude is equal to $k = k_0 + j\alpha$, and $\hat{\mathbf{k}}$ is a unit vector. Here α is the attenuation

coefficient of the medium, $k_0 = 2\pi/\lambda = \omega/c$ is the propagation constant, λ is the wave length, and c is the phase velocity. With the above notation, Eq. (3.3) can be rewritten as

$$p(r) = p_0 \exp(-\alpha r)\exp(jk_0 r) \tag{3.4}$$

When a plane wave propagates from r_1 to r_2 which is assumed to be $r_1 + D$ below, we have $p(r_2)$ and $p(r_1)$, and their relation is

$$p(r_2) = p_0 \exp(-\alpha r_2)\exp(jk_0 r_2) = p(r_1)\exp(-\alpha D)\exp(jk_0 D)\,. \tag{3.5}$$

From Eq. (3.5), it follows that the amplitude is attenuated by $\exp(-\alpha D)$ after the plane wave travels through a distance D. The attenuation coefficient can be easily found to be

$$\alpha = \frac{1}{D}\ln\frac{|p(r_1)|}{|p(r_2)|} = \frac{\ln|p(r_1)| - \ln|p(r_2)|}{D}\,. \tag{3.6}$$

Here α is given in nepers/cm, abbreviated Np/cm. Another unit, dB/cm, is often used to measure α which is expressed, by use of the logarithm to base 10, as

$$\alpha = \frac{1}{D}20\log\frac{|p(r_1)|}{|p(r_2)|}\,. \tag{3.6a}$$

For conversion between the two coefficients values, recall that 1 Np = 8.686 dB.

B. Transient plane waves in a attenuating solid layer immersed in a lossless fluid

Consider a case shown in Fig. 3.1 where a solid plate has thickness D and attenuation coefficient α, and it is submerged in a lossless fluid and located in the plane $z = z_{fs}$.

In general, when a plane wave p impinges on the plate at incident angle θ, it excites a reflected plane wave, a transmitted longitudinal wave (LW), and a transmitted shear wave (SW) at the fluid/solid interface (front surface), and the transmitted LW and SW travel to the solid/ fluid interface (back surface), reflect, propagate back to the front surface and transmit into the fluid. In the case of normal incidence, i.e., when $\theta = 0$, only LW is excited and propagates in the solid plate. Here we only deal with the normal incident case.

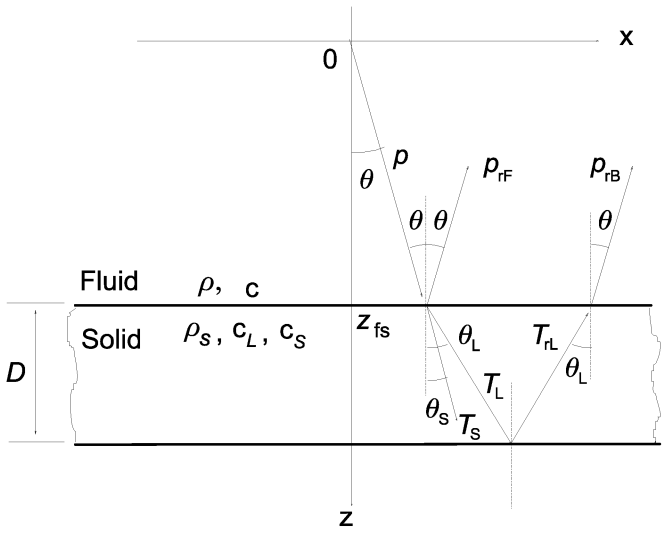

Fig. 3.1. Geometry and notation for the estimation of attenuation coefficient from reflected plane waves.

Suppose a transient plane wave $p(z, t)$ propagating in a lossless fluid. It is well known that a transient plane wave can be decomposed into an infinite set of continuous plane waves by means of Fourier transform. The component of the transient plane wave at frequency ω is denoted by $P(z,\omega)$, and the plane waves reflected from the front surface at $z = z_{fs}$ and the back surface are represented by $P_{rF}(z,\omega)$, and $P_{rB}(z,\omega)$, respectively. Considering reflection and transmission at the front and the back surface and the longitudinal wave number $k_L = k_{0L} + j\alpha_L$ in the solid layer, we can find the attenuation coefficient of the solid plate to be

$$\alpha_L(\omega) = \frac{1}{2D}\ln\frac{4\rho c\rho_s c_L}{(\rho c+\rho_s c_L)^2}\frac{|P_{rF}(z,\omega)|}{|P_{rB}(z,\omega)|} = \frac{1}{2D}\ln\frac{|P_{rF}(z,\omega)|}{|P_{rB}(z,\omega)|} + \frac{1}{2D}\ln\frac{4\rho c\rho_s c_L}{(\rho c+\rho_s c_L)^2}. \qquad (3.7)$$

The detailed derivation of Eq. (3.7) is given in Appendix 3-A. Eq. (3.7) indicates that evaluation of attenuation in a solid plate using the reflected waves from the front and the back interface needs to take into account transmission ratios at both interfaces.

3.2.3 Evaluation of attenuation by means of pulse echoes - the log-spectral difference method and the spectral shift method

Ultrasonic attenuation in materials [40] and tissues [38,39] can conveniently evaluated by means of reflected ultrasound. In NDT, immersion measurement of a metal is a commonly-used method which we have also been using to inspect copper canisters [6,7]. To evaluate ultrasonic attenuation in copper, we will base ourselves on the log-spectral difference method and the spectral shift method which had been presented in [38-40]. The two methods both use as inputs the echoes from the front and back surfaces of the immersed metal, or from within grains in the metals. In the present study, we

will use as transmitter/receiver a focusing array of the ALLIN system (abbreviated the ALLIN array) and utilize the echoes from the front and back surfaces in the evaluation. Below, we give a brief introduction to the log-spectral difference method and the spectral shift method.

The log-spectral difference method and the spectral shift method were introduced by Kuc [38,39] based on the knowledge of signal processing. In the case of human tissues, the attenuation coefficient $\alpha(f)$ is an approximately linear function of frequency. But in the case of polycrystalline metals, it is usually not [18-23,43,44,47,48], and thus, the linear fitting of log-spectral difference does not hold in our case. Therefore, we shall present the methods in a more general style, i.e., $\alpha(f)$ is an nonlinear function of frequency.

Suppose the input pulse is $p_i(t)$ and has power spectrum $P_i(f)$ with central frequency f_i. After passing through an attenuating medium, the observed output pulse $p_o(t)$ is attenuated and its power spectrum $P_o(f)$ with central frequency f_o can be written as,

$$P_o(f) = |H(f)|^2 P_i(f), \tag{3.8}$$

where $|H(f)|^2$ is the power transfer function, expressed as

$$|H(f)|^2 = \exp[-\alpha(f)2D], \tag{3.9}$$

where $2D$ is the path length through which the pulse $p_i(t)$ propagates.

The log-spectral difference method is the way of estimating the attenuation coefficient $\alpha(f)$ by taking logarithm on both sides of Eq. (3.8) and inserting Eq. (3.9) into Eq. (3.8); that is,

$$\alpha(f) = \frac{\ln P_i(f) - \ln P_o(f)}{2D}. \tag{3.10}$$

Obviously, Eq. (3.10) does not include the diffraction correction, and thus it is only good to use for small D so that the beam does not spread so much to induce significant error.

The spectral shift method is an alternative of the log-spectral difference method with the assumption of the input pulse $p_i(t)$ being Gaussian shaped and $\alpha(f)$ being a linear function of frequency. In practice, attenuation coefficient $\alpha(f)$ is obtained by using an appropriate way to determine the central frequencies of the input and output signals, f_i and f_o, and the bandwidth of the input signal, B, that is,

$$\alpha(f) = \frac{(2\pi)^2}{B^2} \frac{f_i - f_o}{2D} f \ . \tag{3.11}$$

Note that the spectral shift method always assumes $\alpha(f)$ to be a linear function of frequency and the input pulse $p_i(t)$ to be Gaussian shaped, and thus the output pulse $p_o(t)$ is Gaussian shaped, whereas the log-spectral difference method is not limited to $\alpha(f)$ to be a linear function of frequency.

3.2.4 Evaluation of attenuation in copper specimens

Attenuation in three copper specimens was evaluated by means of the log-spectral difference method and the spectral shift method. The three copper specimens used in the following experiments came from High Profile Ultrasonics Ltd., England, and the specifications of the specimens are listed in Table 3.1 [60]. The original specimens had rough surfaces. To reduce the effects of the surface roughness on measurements, two sides in the thickness direction were machined and ground.

Table 3.1 Specifications of the specimens [60]

No	Specimen reference	Origin	Length (mm)	Width (mm)	Thickness (mm)	Nominal grain size (microns)	Condition
4	SE 1550	TWI-OUTOKOMPU	92	67	36	250-350	Hot rolled
1	SE 1593	TWI-REVERE	99	59.5	41.5	175-200	Hot rolled
2	SE 1603	TWI-MKM	102.6	59.5	40.2	125-175	Hot rolled

Since the spectral shift method gave more stable estimation of attenuation than the log-spectral difference method, the results from the spectral shift method are presented here. From table 3.1, it follows that grains in specimen 4 are largest, and those in specimen 2 smallest. Measurements were carried out based on the ALLIN array system in MONO TRANSDUCER mode which enables a single element transducer to be used. The transducer used in the measurements was PANAMETRICS V307, 25-mm diameter, 191.1-mm focal length (measured), and 5.35-MHz central frequency (measured). The measurements were made in immersion configuration. The sound velocities of water and the copper specimens measured at room temperature were 1485 m/s, and 4596 m/s, respectively. Considering the effect of diffraction (not the correction of diffraction) on the evaluation of attenuation, the water path was set 130 mm. This made the focal zone located around the middle depth in the inspected specimens. The transducer was scanned in the *x*-*y* plane. The specimens were put with their thickness being parallel to the *z* direction. Therefore, the thickness of specimens 4, 1, and 2

used in calculating attenuation were 36, 41.5, and 40.2 mm, respectively. The scanning positions for acquiring data on specimens 4, 1, and 2 were 70x50, 60x48, and 70x44 with 1-mm step, respectively, which corresponded to 3500, 2880, and 3080 A-scans, respectively. The temporal sampling frequency used was 100 MHz. Since the attenuation in copper is so large that, when the echoes from the front surfaces (called front echo below) were not saturated and were seen in full wave-form, those from the back surfaces (called back echo below) were too small to be seen, the front and the back echoes were recorded in separate measurements using different amplifier gains (c.f. columns 4 and 6 in table 3.2).

Before calculating attenuation using the recorded data, we checked the peak amplitudes of the front echoes and the back echoes in all A-scans for each case. The distributions of the peak amplitudes are shown in Fig. 3.2. The mean values and the deviations of each case in the figure are calculated and listed in table 3.2 (see columns 5 and 6). From Fig. 2.3 and table 3.2, we see that the deviation of front echo peak amplitudes is small, while that of back echo peak amplitudes is very large. Thus, we have confirmed that all the specimens are not homogeneous. Due to the inhomogeneity, the attenuation should be evaluated using large set of A-scans. We used all the A-scans in the data recorded from each specimen. Fig. 3.3 shows how the evaluation of attenuation was conducted. First, we gated out the front echo and then the back echo (Fig. 3.3(a)); secondly, we performed the fast Fourier transform on the two gated echoes and made Gaussian fitting for two amplitude spectra (Fig. 3.3(b)); and finally, we determined two central frequencies and band widths from the Gaussian fit spectra and obtained the attenuation coefficients from Eq. (3.11).

The evaluated attenuation coefficients of the specimens are listed in table 3.2. Due to the inhomogeneity of the specimens, the attenuation coefficients obtained from different A-scans were different, and thus, they fluctuated about the mean value in a certain range. Relating grain sizes of the specimens (see table 3.1) with the coefficients, we see that the larger the grain size the higher the attenuation. This coincides with theory.

Table 3.2 Experimental setup, measured peak amplitude and measured attenuation coefficients for Specimens 4, 1 and 2

No:	Scanning position	Thickness (mm)	Front echoes' Gain (dB) & amplitude		Back echoes' Gain (dB) & amplitude		Attenuation (dB/mm)
4	70x50	36	8	$98.24^{+5.76}_{-4.24}$	43	$85.86^{+42.14}_{-48.86}$	$0.4613^{+0.0489}_{-0.0645}$
1	60x48	41.5	9	$107.71^{+4.29}_{-3.71}$	48	$78.43^{+34.57}_{-30.43}$	$0.3803^{+0.0279}_{-0.0288}$
2	70x44	40.2	8	$98.78^{+4.22}_{-2.78}$	38	$85.78^{+25.22}_{-22.78}$	$0.3684^{+0.0398}_{-0.0469}$

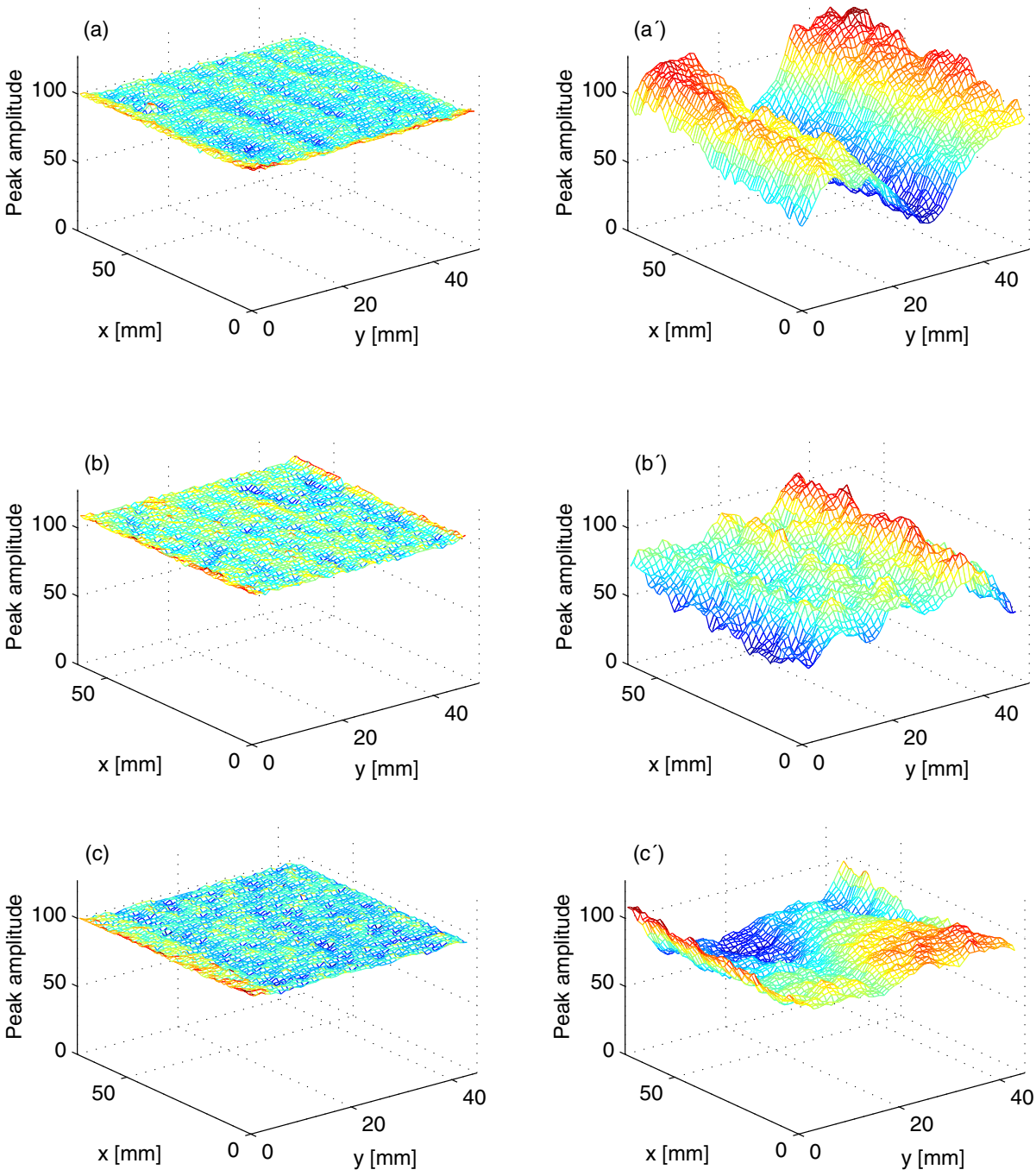

Fig. 3.2. Distributions of peak amplitudes of front echoes from (a) specimen 4, (b) specimen 1, and (c) specimen 2, respectively, and those of back echoes from (a') specimen 4, (b') specimen 1, and (c') specimen 2, respectively.

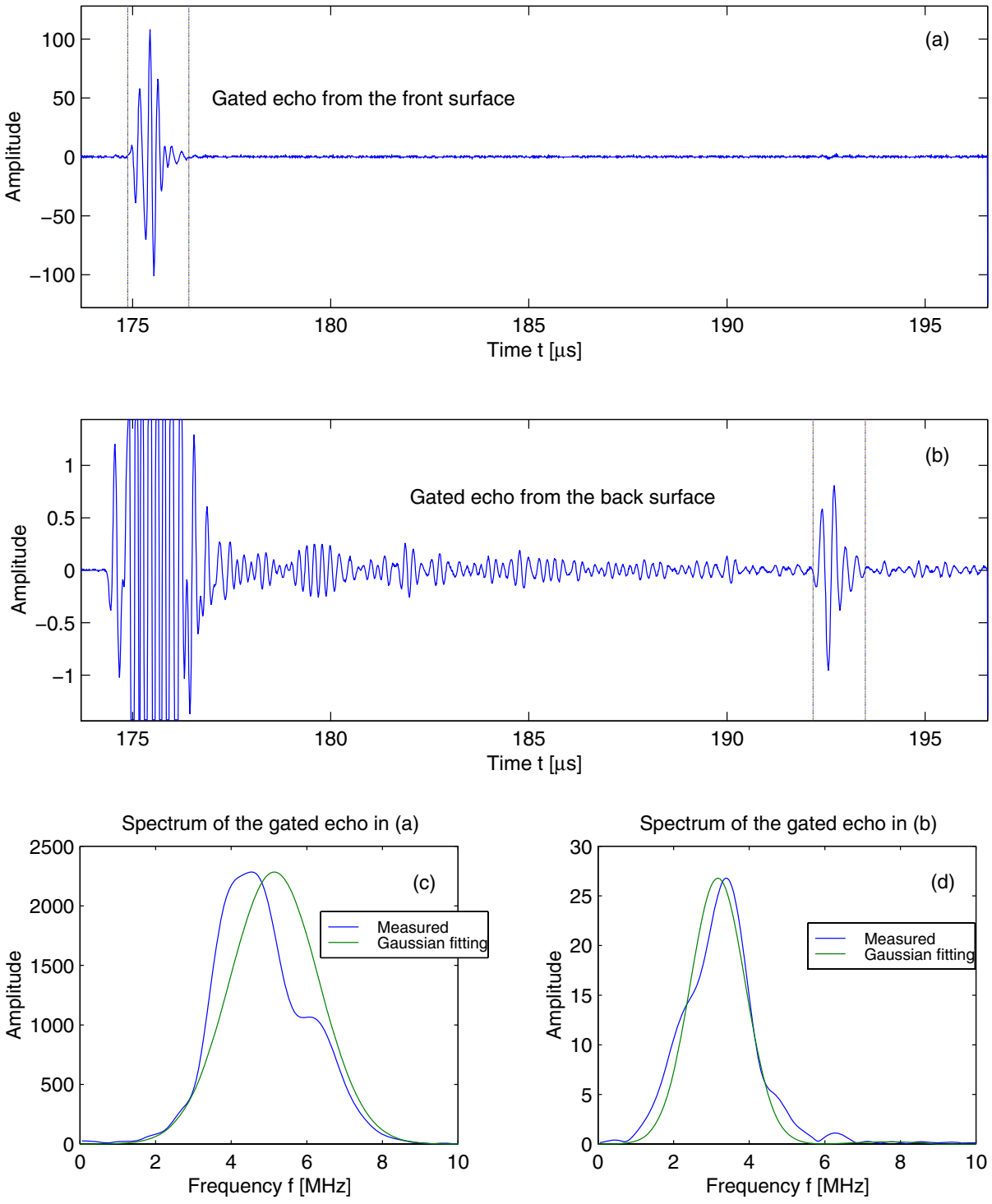

Fig. 3.3. Evaluation of attenuation. (a) Gating front echo, (b) Gating back echo. Gaussian fitting the spectra of (c) gated front echo, and (d) gated back echo.

3.3 Evaluation of ultrasonic grain noise in polycrystalline metals

Ultrasonic grain noise in an ultrasonic signal from a polycrystalline metal results from the grain structure of the metal. It may mask defect signals, and thus needs to be suppressed when the defects need to be detectable [12-14]. However, grain noise is also a useful signal containing the information about the microstructure of a material [15-17], and this information can be helpful for a materials scientist to design a material (e.g., an alloy) with desirable mechanical properties by controlling the microstructure. Therefore, it is necessary to understand how the grain noise is related to the microstructure. To this purpose, some authors have done research to relate the grain noise signals to ultrasonic grain size [43,44], and others have developed a number of models to predict the grain noise [7, 15, 32-37,55]. Here we will present a model used to predict grain noise. The model is similar to that proposed by Margetan *et al*.

3.3.1 Properties of grain noise

Grains act as irresolvable scatterers that produce the coherent interference. The coherent interference on a phase-sensitive receiver (most of transducers used in NDT are phase sensitive) results in grain noise in ultrasonic echo signals like A-scan and B-scan signals. Ultrasonic grain noise, although temporally stable, is spatially random. Therefore, the properties of grain noise are estimated statistically in space. Typical ultrasonic measures of grains (scatterers), called material parameters, can be scatterer number density, scatterers' mean size, and scatterers' mean spacing. To determine the material parameters, the statistics of measured signals are employed. Different material parameters are determined using different statistics. One material parameter can be determined using different statistics, that depend on the models used. Due to random character of media, the methods used to establish the models are stochastic.

The statistics of magnitude distribution of pulse-echo signals can be modeled by the K-distribution [7,55]. The root-mean-squared (RMS) deviation of grain noise signals from its ensemble average can be predicted by the independent scattering model [32-33], which will be presented below.

Before presenting the ISM, we shall give the RMS value of grain noise signals. A measured signal voltage at time t for transducer position m is denoted by $V_m(t)$. If signals are acquired at M transducer positions, then the background voltage $b(t)$ which would be observed in the absence of grain noise may be estimated as

$$b(t) = \frac{1}{M}\sum_{m=1}^{M} V_m(t)\,. \tag{3.12}$$

The root-mean-squared (rms) deviation of grain noise from the background is then,

$$n(t) = \left[\frac{1}{M}\sum_{m=1}^{M}\left(V_m(t) - b(t)\right)^2\right]^{1/2}. \tag{3.13}$$

Normalized version of *n(t)* is obtained by dividing by $E_{\max}$, the peak amplitude of the reference signal:

$$N(t) = n(t)/E_{\max}\,. \tag{3.14}$$

For broadband pulses $E_{\max}$ is defined as one half of the peak-to-peak voltage of the reference signal. For near-harmonic tone-burst pulses, where the reference signal takes the form $E(t)\sin(\omega t)$, $E_{\max}$ is defined as the peak value of the envelope function *E(t)*. Note that the rms grain noise which is shown as a function of time may be regarded as a function of depth within the specimen. This normalized RMS grain noise, *N*(*t*) will be predicted by the ISM.

3.3.2 Theoretical model of grain noise

The independent scattering model (ISM) was developed by Margetan *et al* [32] based on the scattering measurement model proposed Thompson and Gray [59]. The scattering measurement model was established by using the Auld's electromechanical reciprocity relations. The independent scattering approximation (properly defined) can be interpreted as the first term in a systematic expansion for the backscatter signal. The detailed, rigid theory for the backscattered signal is presented in Appendix 3-B.

The geometry for the ISM is shown in Fig. 3.4. The water paths Z_{0R} for the reference signal and Z_{0S} for the noise measurement are measured outward from the transducer face along the central ray direction. The coordinates for the points in the metal are measured for the intersection of the central ray and the water/solid interface (see Fig. 3.4).

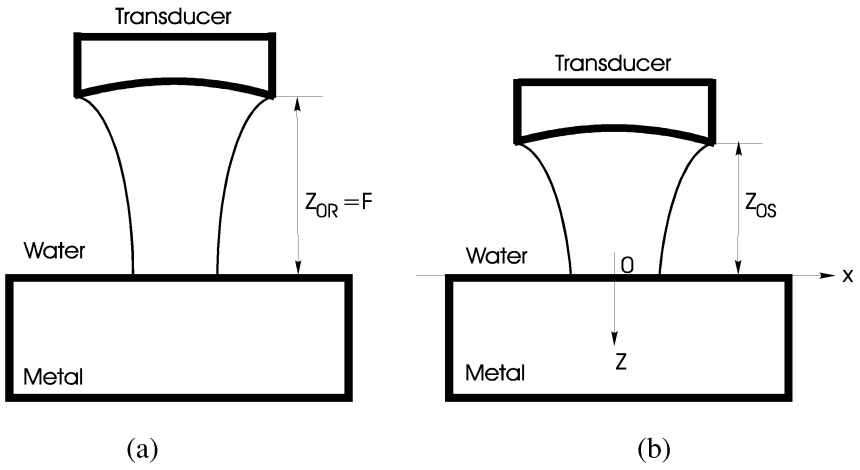

Fig. 3.4. Geometries for (a) reference signal acquisition and (b) noise measurement.

The first step. The establishing of the ISM started with using the results from the measurement model proposed by Thompson and Gray [59]. The pulse-echo from the front-surface is used as reference signal, denoted by $V_{ref}(t)$, and the voltage signal due to scattering by a single grain located at position (x, y, z) is denoted by $\delta S(t,x,y,z)$. Assuming $\tilde{V}_{ref}(\omega)$ and $\delta\tilde{S}(x,y,z;\omega)$ to be the Fourier transform of $V_{ref}(t)$ and $\delta S(t,x,y,z)$, respectively, and from [59], we have

$$\tilde{V}_{ref}(\omega) = \beta R_{00} D(\omega) \exp(-j2k_0 z_{0R} - 2\alpha_0 z_{0R}), \tag{3.15}$$

and

$$\delta\tilde{S}(\omega,x,y,z) = \left[\frac{2\beta A(\omega,x,y,z)\rho_1 c_1}{jk_1 a^2 \rho_0 c_0}\right] T_{01}^2 C^2(\omega,x,y,z) \exp\left[-j2(k_0 z_{0S} + k_1 z) - 2\alpha_0 z_{0S} - 2\alpha_1 z\right]. \tag{3.16}$$

Eq. (3.16) was derived employing the Auld's reciprocity relations [57]. In Eqs. (3.15) and (3.16), c, $k = \omega/c$, ρ, α and a denote longitudinal wave velocity, wave number, density, attenuation coefficient, and transducer radius, respectively, with subscripts 0 and 1 referring to water and metal. β is the transducer efficiency, defined as the ratio of the outgoing ultrasonic power to the incident electric power in the transducer cable. R_{00} and T_{01} are the reflection and transmission coefficients for plane wave velocity fields propagating in the central-ray direction. $A(\omega,x,y,z)$ is the amplitude of the backscattered sound from the single grain under consideration. $C(\omega,x,y,z)$ is a measure of ultrasonic field strength in the metal; if the velocity on the transducer face is $V_0 \exp(j\omega t)$, then $V_0 C(\omega,x,y,z)\exp[j\omega t - j2(k_0 z_{0S} + k_1 z)]$ is the velocity at point (x,y,z) that would exist in the absence of attenuation and interface transmission losses. $D(\omega)$, which accounts for the effects of diffraction losses in the reference signal, is defined as the integral of the reflected velocity field over the

equilibrium location of the transducer face, divided by $\pi a^2 V_0 \exp[j(\omega t - 2k_0 z_{0R})]$, again in the absence of other losses. In addition to the explicit dependence on frequency, $C(\omega, x, y, z)$ and $D(\omega)$ depend on the transducer characteristics (a and F), water path, and sound speeds. The reference signal in Eq. (3.15) is used for eliminating β.

The second step. Assuming that the total noise signal $S(t, x, y, z)$ is an incoherent superposition of noise signals backscattered by the individual grains of the metal (i.e., only single-scattering events is considered explicitly), and that the attenuation of the beam with depth will be treated through an effective attenuation constant, we have

$$\frac{\sqrt{\langle \tilde{S}^2(\omega) \rangle}}{\tilde{V}_{ref}(\omega)} = n^{1/2} \left| \overline{A}(\omega) \right| \frac{2T_{01}^2 \rho_1 v_1 \exp[-2\alpha_0 (z_{0S} - z_{0R})]}{R_{00} a^2 \rho_0 v_0 |D(\omega)| k_1} \left[\int_0^\infty P \exp(-4\alpha_1 z) dz \int_{-\infty}^{\infty} \int_{-\infty}^{\infty} \left| C(\omega, x, y, z) \right|^4 dx dy \right]^{1/2}, \tag{3.17}$$

where n is the volume density of grains, and $\overline{A}(\omega)$ is an averaged grain backscatter amplitude at frequency ω. The normalized rms grain noise is directly proportional to $n^{1/2} \left| \overline{A}(\omega) \right|$, which is called figure of merit (FOM) for noise severity.

3.3.3 Experimental evaluation of grain noise by means of the ISM

The three copper specimens were inspected using the ALLIN array system, and grain noise from the specimens were evaluated by means of the ISM. The same experimental setup as in Sec. 3.2.4 was used. The gains used for measuring the reference signals and the grain noise signals are listed in table 3.3.

The RMS grain noise from the three specimens were calculated from Eqs. (3.13) and (3.14), and the results are shown in blue in Fig. 3.5. The prediction of the RMS grain noise was made based on Eq. (3.17), and the results are shown in red in Fig. 3.5. From the measured results and the model, the FOMs for the specimen were obtained and listed in table 3.3.

Comparison of the measured and the predicted results indicates that the ISM gives good prediction in the shallow parts of copper specimens (the early time portions of signals), but shows gradual deviation as the depth increases. The reason for this can be (i) that the ISM was established for narrow band signal [32], and (ii) that the ISM was established based on such an approximation (see the approximation used for Eq. (B3.9) in Appendix 3-B) that is expected to be valid for the early time portion of the signal when the main beam has not been significantly attenuated (also see [36]).

From the values of FOM in table 3.3, we can conclude that the larger the grains, the bigger the FOM. Therefore, FOM can be an appropriate parameter used for depicting noise severity as stated in the theory (c.f. Sec. 3.3.2).

Table 3.3 Experimental setup and measured figure of merit (FOM).

Specimen No	Gain for reference signal (dB)	Gain for grain noise signal (dB)	Figure of merit (FOM, $1/\text{mm}^{1/2}$)
4	2	56	0.43
1	3	56	0.37
2	3	57	0.33

To facilitate comparison of the results obtained from different specimens, we put the results in the same figure (Fig. 3.6 (a) the measured and (b) the predicted). From the figure, we see that specimen 4 yields a largest grain noise in the shallow part, specimen 2 gives the smallest noise, and specimen 1 produces the noise in between; whereas in the deep range (35 - 40 mm), specimen 2 gives the largest noise, specimen 4 gives the smallest. The reason is that in the shallow range the larger grains generate stronger backscattering, and then attenuate more ultrasonic energy as the sound travels deeper. Thus, we have demonstrated the usefulness of the ISM for the evaluation of grain noise severity in copper.

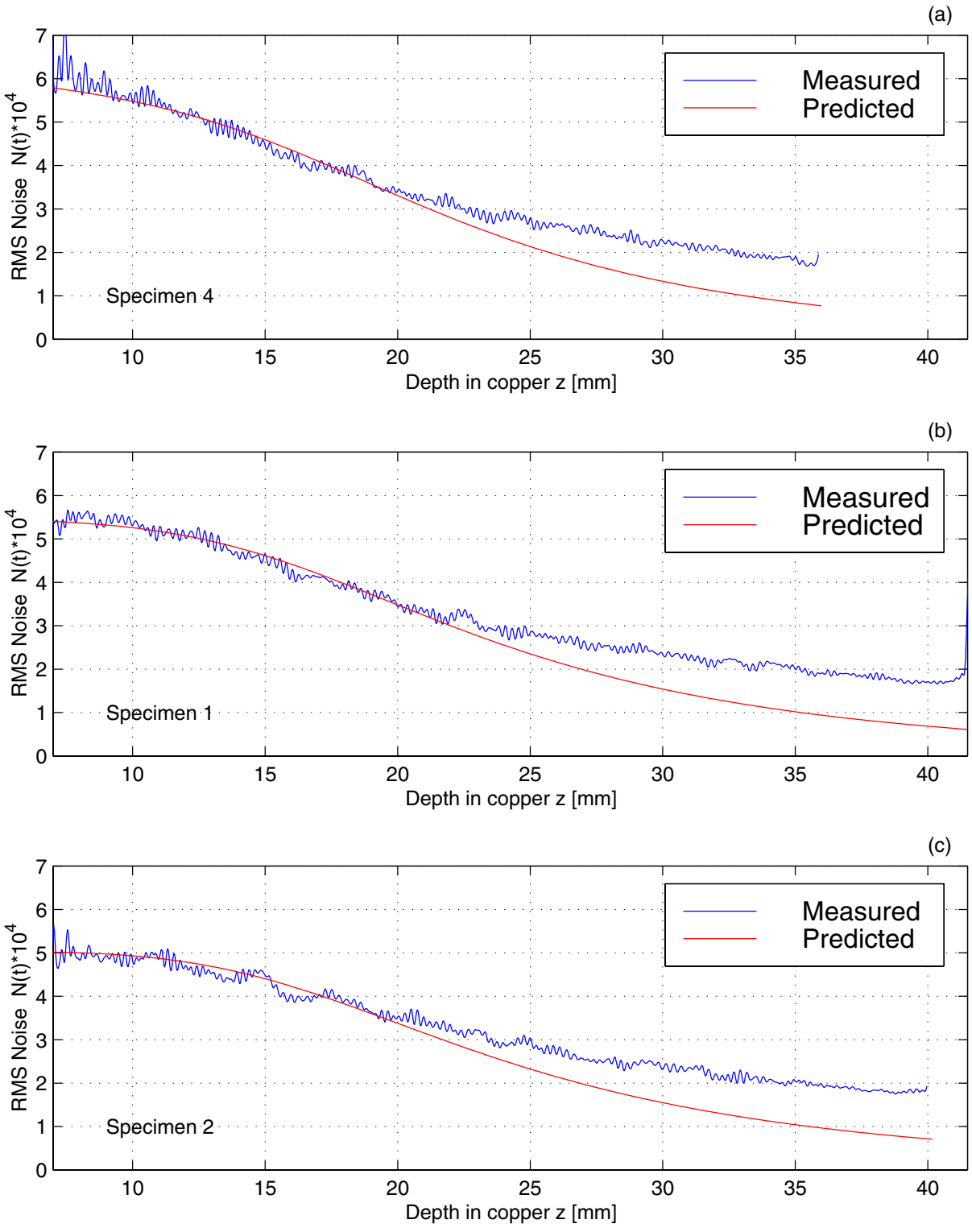

Fig. 3.5. Measured (blue) and predicted (green) RMS grain noise, $N(t)$, in copper specimens (a) 4, (b) 1, and (c) 2.

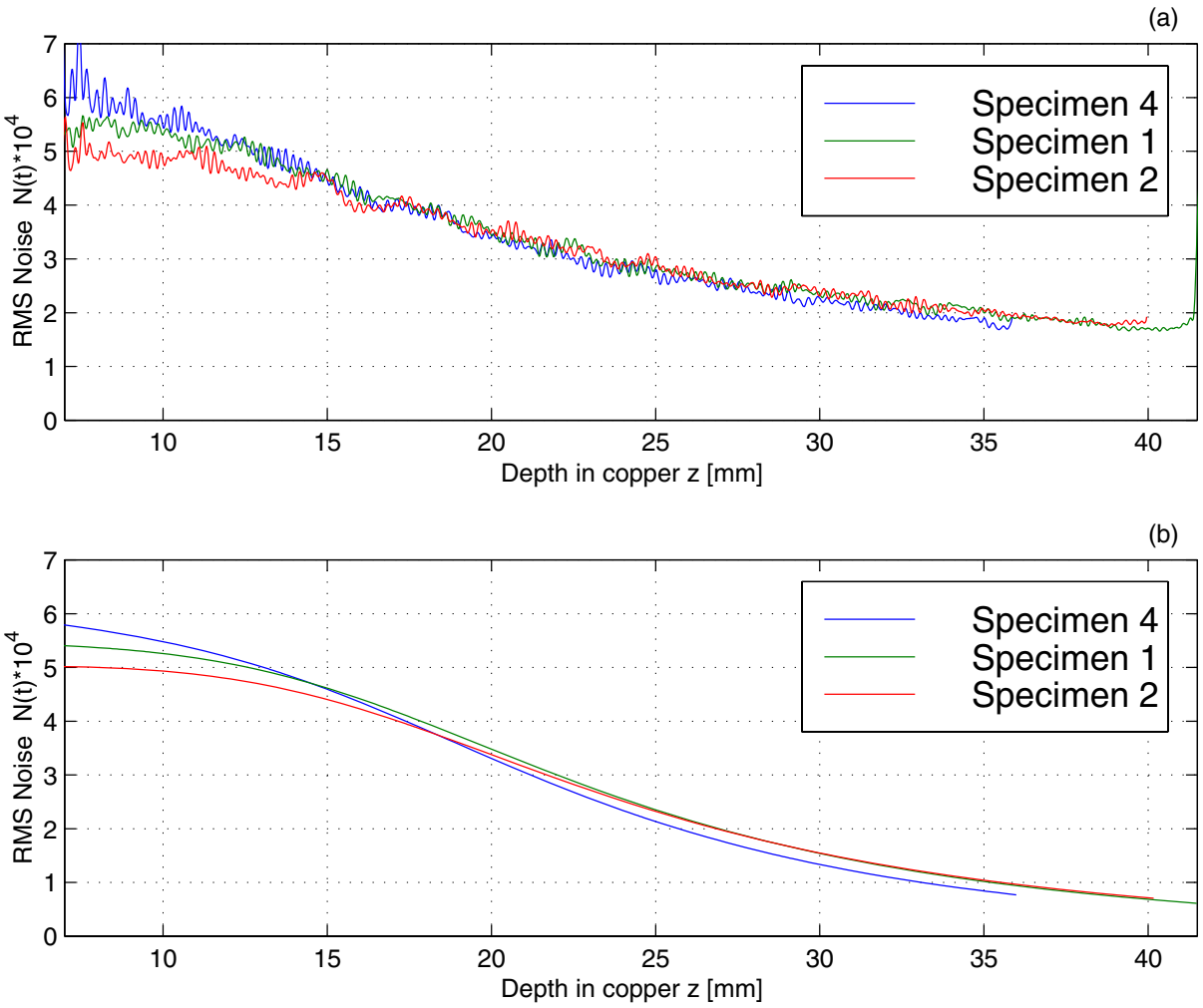

Fig. 3.6. Comparison of (a) measured results and of (b) predicted results in copper specimens 4, 1, and 2.

3.3.4 Evaluation of grain noise in welds in copper canister by means of the K-distribution

In our previous work, the K-distribution model was applied to evaluate grain noise from copper blocks without welds and to detect defects in the blocks [7]. Here the model is used to evaluate grain noise from welds of a copper canister and to detect flaws in the welds. The K parameters, α_1, α_4, α_6, used here are all defined in [7].

One of five sections of a copper canister weld W123 was inspected by means of the ALLIN array system. The section inspected was denoted by BLOCK4. The ALLIN array was the transducer used in the measurements. The experimental setup used was the same as that for Fig. 2.28(d), e.g., the focusing law being Foc60E16, and the water layer being 28 mm.

For the evaluation of grain noise from the weld, the effects of defects need to be excluded, whereas for the detection of defects, the defects are the targets. For this purpose, we need to select the regions of interest (ROI). The selection of ROI was done in the following way. First, the C-scan (Fig. 3.7(a)) was generated with the weld gated in a window (the two vertical white lines in Fig. 3.7(b)); secondly, the C-scan was divided into four regions, that is, region #3 which does not contain defects, region #2 which contains defects, and region #1 which is the part in the C-scan excluding regions #2 and #3, and is mostly out of the weld; and thirdly, the ROI selected for the evaluation was region #3, and the ROI for the detection was region #3 + region #2. All the regions have the same thickness, the one between the two white lines in Fig. 3.7(b).

In ROI = #3 and in ROI = #3+#2, the K parameters were calculated based on the C-scans at different depths. The results for the two cases are shown in Fig. 3.8 and Fig. 3.9. Fig. 3.8, (a) & (b) show the K parameters for ROI = #3 with two different scales, and (c) & (d) show the K parameters for ROI = #3+#2. Fig. 3.9, (a) & (b) show the difference of K parameters for ROI = #3, and (c) & (d) show that for ROI = #3+#2. In comparison of the results in ROI = #3 and ROI = #3+#2, we can find the difference between the results in the two cases which is large in the range of z = 55 - 60 mm that corresponds to the weld zone. In the former case (ROI = #3), the K parameters in this range are larger than unity; whereas in the latter case (ROI = #3+#2), the K parameters are much smaller than unity (c.f., Fig. 3.10(b)). According to Fig. 3.8, we selected the C-scans at three different depths for evaluation of their probability density functions (pdf's). The first C-scan was at z = 54.69 mm, which was before the defect-containing zone; the second C-scan was at z = 57.45 mm, which was just in the defect-containing zone; and the third one was at z = 62.09 mm, which was after the defect-containing zone. The three C-scans and their pdf's, the measured and the predicted, are shown in Fig. 3.10. From the figure, we see that in the case of the C-scan containing defects the predicted pdf's can not fit the measured pdf at all (Fig. 3.10(b)); whereas the rest cases, the predicted fit the measured well (Fig. 3.10(a) and (c)).

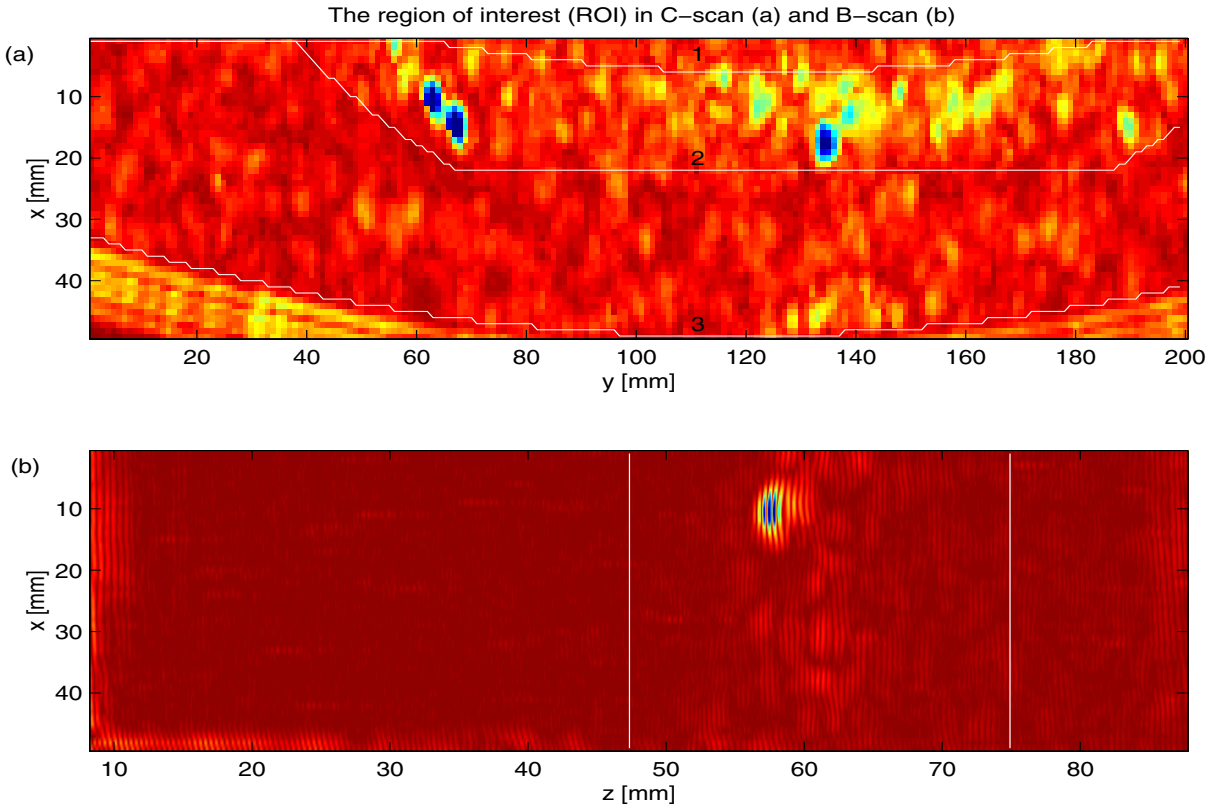

Fig. 3.7. The region of interest (ROI) used for the evaluation of grain noise in weld W123 by means of the K-distribution.

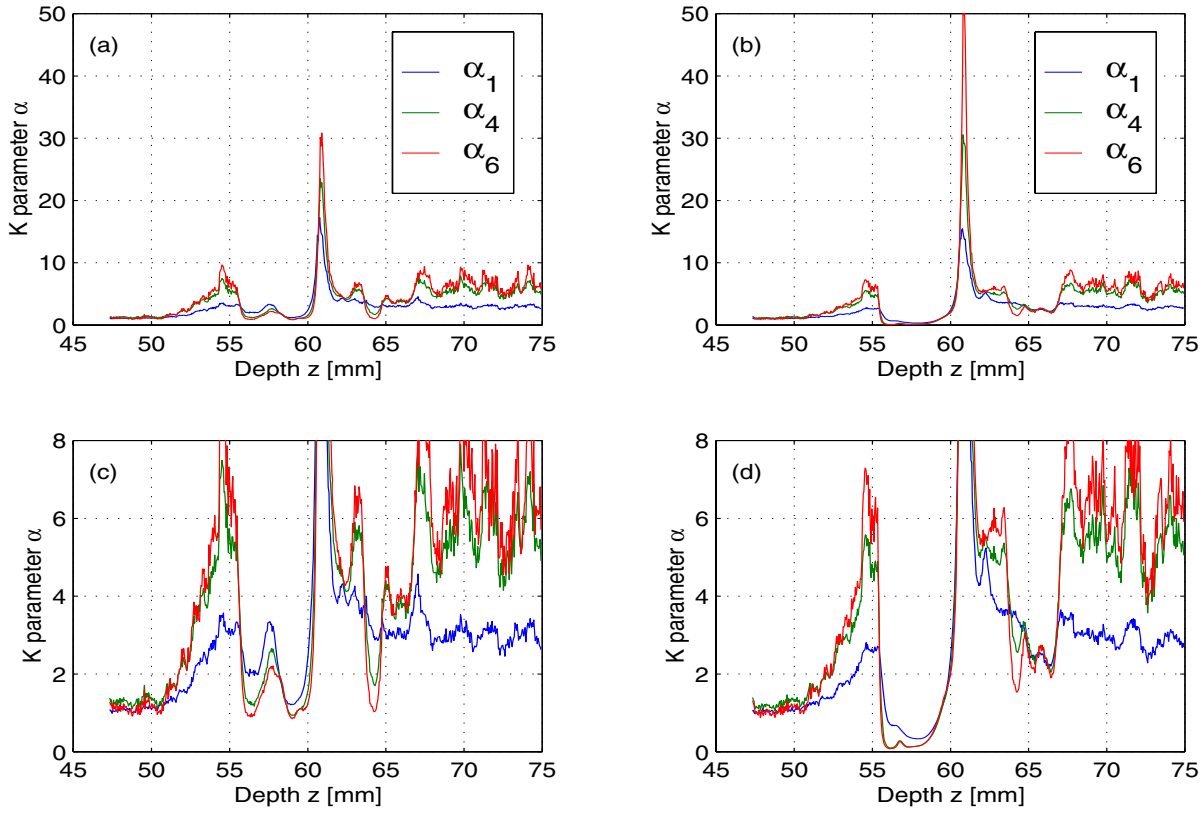

Fig. 3.8. The K-parameters α_1, α_4, α_6 in the ROI of weld W123 (a) & (c) in ROI=#3, and (b) & (d) in ROI=#3+#2.

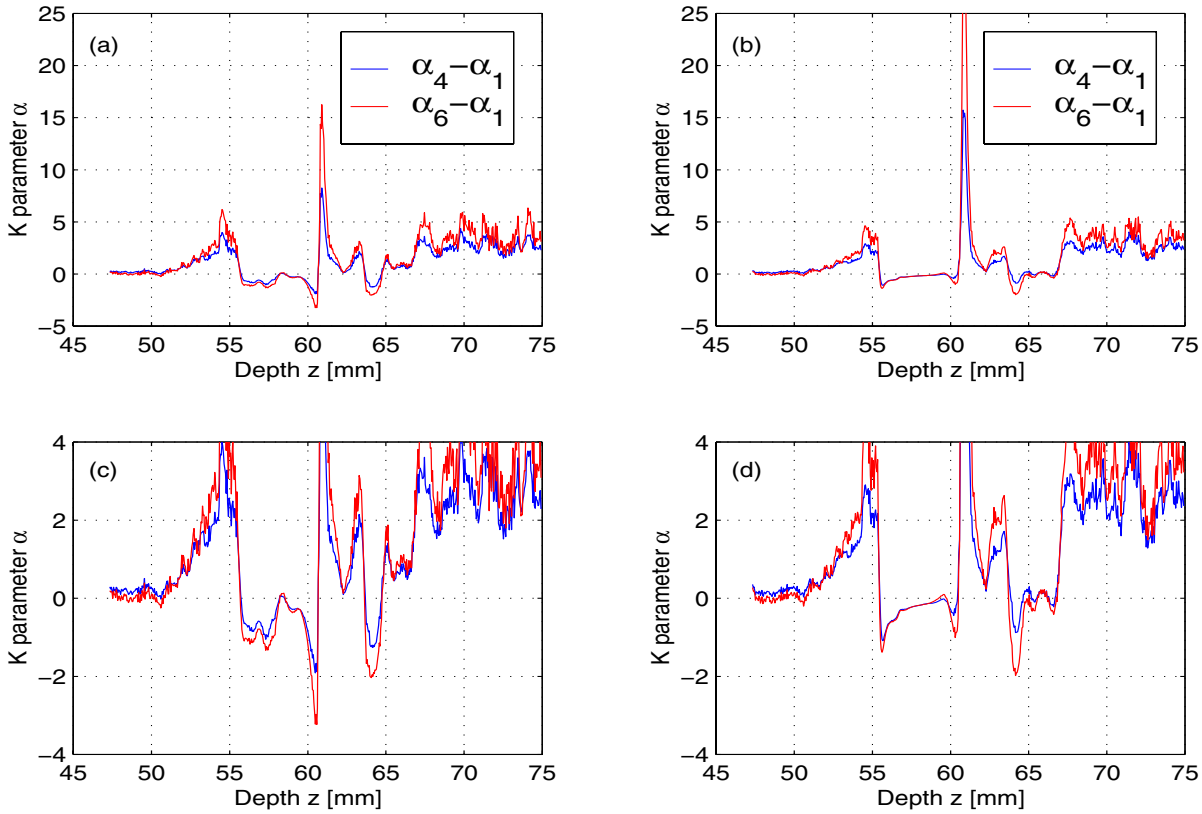

Fig. 3.9. $\alpha_4 - \alpha_1$ and $\alpha_6 - \alpha_1$ where α_1, α_4, α_6 are the same as in Fig. 3.8.

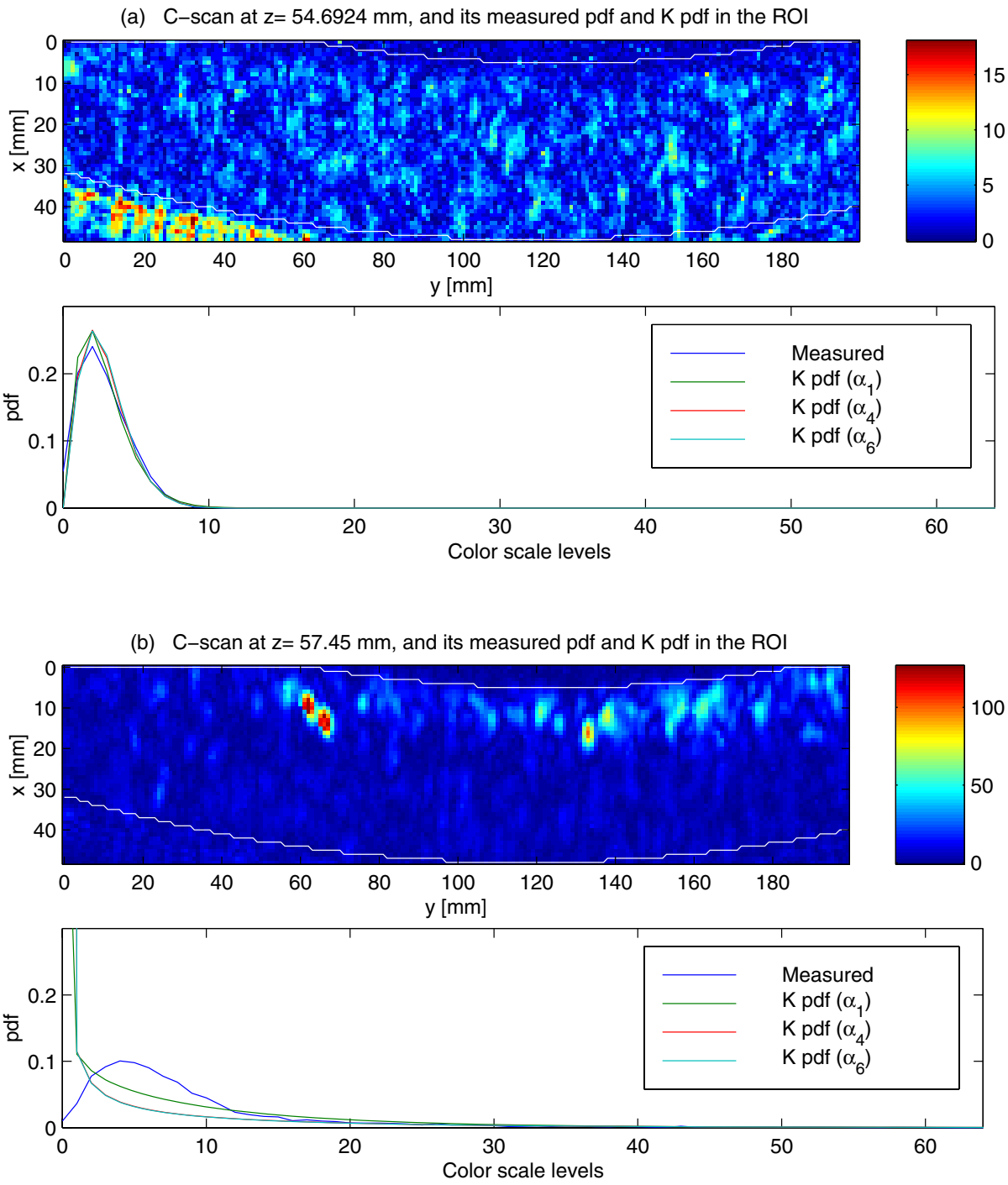

Fig. 3.10. The measured and the predicted probability density functions (pdf) in the ROI's at
(a) $z = 54.69$ mm, $\alpha_1 = 2.767$, $\alpha_4 = 5.477$, $\alpha_6 = 7.012$;
(b) $z = 57.45$ mm, $\alpha_1 = 0.362$, $\alpha_4 = 0.128$, $\alpha_6 = 0.126$; and
(c) $z = 62.09$ mm, $\alpha_1 = 4.961$, $\alpha_4 = 5.523$, $\alpha_6 = 5.701$.

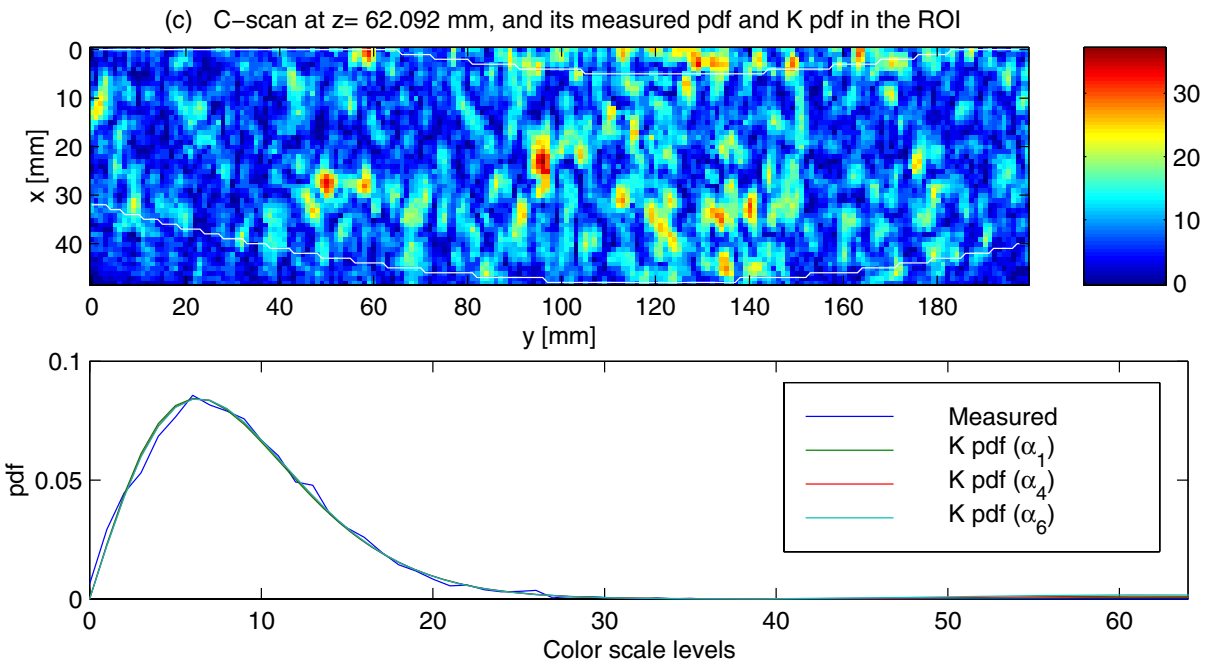

Fig. 3.10. The measured and the predicted probability density functions (pdf) in the ROI's at

(a) $z = 54.69$ mm, $\alpha_1 = 2.767$, $\alpha_4 = 5.477$, $\alpha_6 = 7.012$;

(b) $z = 57.45$ mm, $\alpha_1 = 0.362$, $\alpha_4 = 0.128$, $\alpha_6 = 0.126$; and

(c) $z = 62.09$ mm, $\alpha_1 = 4.961$, $\alpha_4 = 5.523$, $\alpha_6 = 5.701$.

3.4 Suppression of ultrasonic grain noise in polycrystalline metals

3.4.1 Introduction

The objective of this task was to investigate techniques capable of suppressing material (structure) noise backscattered from copper structure, especially in the EB weld zone. Level of material noise in ultrasonic signal determines the ability to detect small flaws in the weld zone.

Material noise, backscattered from the irresolvable scatterers randomly distributed throughout the material is one of the main factors limiting imaging of flaws in metals. Grain noise present in ultrasonic B- and C-scans masks flaws and decreases the detection limit of ultrasonic systems. Intensity of such noise strongly depends on the ratio between average grain size and length of ultrasonic wave used for inspection. Noise intensity can be reduced by using longer ultrasonic waves (lower frequencies), however at the price of reduced resolution.

In copper canisters sealed with EB weld we encounter two noise patterns, first in the solid copper used for lid and walls, and second in the weld zone. The first pattern is typical for metals composed of randomly oriented anisotropic grains backscattering elastic waves. The second is different since ultrasound is scattered both from the material grains and weld structure which is characterized by certain regularity. Indeed, when looking at the results of metallographic examination of the EB weld presented in [61], we can see various forms of plume-shaped fusion zones that depend on welding parameters (cf. e.g., Figure 20 or 23). There are well pronounced striations within the weld zone indicating one or more freezing fronts. Typical freezing point is located at approx. 2/3 depth of the weld counting from the outside wall. The striations can in some cases form a number of distinct, relatively wide bulbous profiles centered at the freezing point. Looking in magnification we can observe a distinct copper microstructure superimposed on the striations (cf. Fig. 26 in [61]).

Looking at the ultrasonic images (C-scans) obtained in pulse-echo inspection we can see a well pronounced difference between the parent material and the welded copper, the weld structure exhibits substantially more backscattering than the parent material. Ultrasonic image of backscattering from the EB weld can provide the operator with a very useful information about the weld structure, penetration depth of the electron beam and flaws present in the weld (cf. our previous reports [6] and [7]). However, extracting information about the flaws from the structure noise requires special means and is generally a very complex task.

Techniques used for suppressing backscattering from the material structure utilize its inherent diversity resulting from the randomness of the irresolvable scatterers. They are based on the assumption that typical flaws due to their regular shape and significant size are characterized by

relatively uniform scattering observed both in frequency domain and for different transducer positions in space. Thus, material noise can be reduced by some type of statistical operation (e.g., averaging) performed on a set of diverse ultrasonic signals backscattered from the material structure and flaws. Techniques utilizing the above mentioned types of diversity are known as respective, frequency diversity and spatial diversity.

Frequency diversity techniques which include different split spectrum processing (SSP) and specialized digital filters, such as noncoherent detector (NCD), are sophisticated non-linear filtering algorithms applied to ultrasonic signals stored in a digital form. It has been shown that when properly tuned, the algorithms can efficiently suppress grain noise in many practical applications [62]. In our previous report [7] we demonstrated successful application of NCD to signals acquired from a copper material characterized by a high level of grain noise.

It appears however, that these techniques are inefficient when applied to the signal from the EB weld zone in copper. Our experiments performed on ultrasonic data acquired for different sections of canister weld have shown practically no reduction of backscattering from the weld zone after the NCD processing. This can be partly explained by the form of the ultrasonic signal reflected from the weld that appears as a short waveform concentrated within the depth interval corresponding to the weld. This signal is different from a typical material noise present throughout the whole material depth. Since the NCD and SSP techniques are aimed at detecting an ultrasonic pulse present in a backscattered noise they are not capable of reducing scattering from the EB weld. We can conclude that it seems to be very difficult to distinguish between flaws and backscattering from the weld structure by electronic processing only one ultrasonic measurement obtained for a single focusing law of ultrasonic array.

The other mentioned above approach, spatial diversity, is more complex since it requires several independent ultrasonic measurements to perform the statistical operation. Such measurements can be relatively easily performed using an ultrasonic array, for example by steering its beam at different angles and acquiring data from the same material volume for all those angles. Obtained in this way ultrasonic data due to the diversity of the signal backscattered from the weld should enable its suppression. There are many ways to create spatial diversity in data and to compound it in order to suppress the undesired backscattering.

3.4.2 Experiments

Here we present results obtained for two sections of EB weld inspected by beams steered at different angles and focused in the weld zone. Two previously used test blocks were used in the experiments, CAN1 with artificial flaws, and Block 3, a section of Weld 123. CAN1 contains 9 drilled holes of different types in the weld zone and 9 twin holes outside the weld zone (see Fig. 2.4 in Section 2 for

details). Block 3 exhibits a number of strong ultrasonic indications from the weld zone (see [63] for details). The blocks were inspected with steered beams inclined in the radial direction from canister center to its outside wall at the angles 0°, 3°, 5°, 7° and 10° (in copper). Beam steering laws were developed using tools described in Section 1 of this report. The array position with respect to the block was adjusted according to the beam angle to obtain C-scan of exactly same area in the weld zone for all angles. C-scans obtained for different angles for CAN1 and Block 3 are presented respectively in Figure 3.11 and 3.13. The C-scans reveal considerable differences in the backscattered patterns obtained for various angles. Local intensity of the ultrasound backscattered from the weld structure is nonuniform over the C-scans, for higher angles a more intensive irregular ring at 2/3 of weld depth is well pronounced. This ring can be associated with freezing fronts observed in the microstructure of the EB weld.

To illustrate the dependence of the weld scattering on beam direction we present in Fig. 3.12 C-scans of a section of CAN1 with flat bottom holes ϕ2.0 and 2.5 mm acquired for the same angles (0°, 3°, 5°, 7° and 10°) but for the beam inclined in circumferential direction. Backscattering from freezing striations is much less pronounced in these C-scans than for those acquired with the beam steered in the radial direction.

Scattering from several strong reflectors located at both sides of the C-scan from Block 3 does not depend much on the beam angle. This indicates volumetric flaws (voids or inclusions). Scattering from the artificial flaws in CAN1 follows expected rules, plain reflectors (FBH) result in the strongest responses at normal incidence while soft round reflectors (RBH) reflect more or less uniformly at all angles.

Above observations can motivate different ways of compounding individual C-scans. The most natural way would be creating a resulting image by taking mean value of corresponding pixels in the individual C-scans. This operation would result in suppressing structure noise due to local averaging and at the same time enhancing targets with uniform response over the used angle range. Plane targets would be also suppressed after averaging. Results of averaging performed on C-scans acquired for CAN1 and Block 3 are shown in Fig. 3.11 (f) and 3.13 (f), respectively. The Averaging of the C-scans obtained for CAN1 reduced weld scattering and revealed round bottom holes that are hardly visible at normal beam incidence. However, other flaws are less pronounced comparing with normal beam C-scan. The averaged image of Block 3 does not reveal any new details, scattering from the weld has been slightly suppressed but intensity of strong local reflectors has been also reduced.

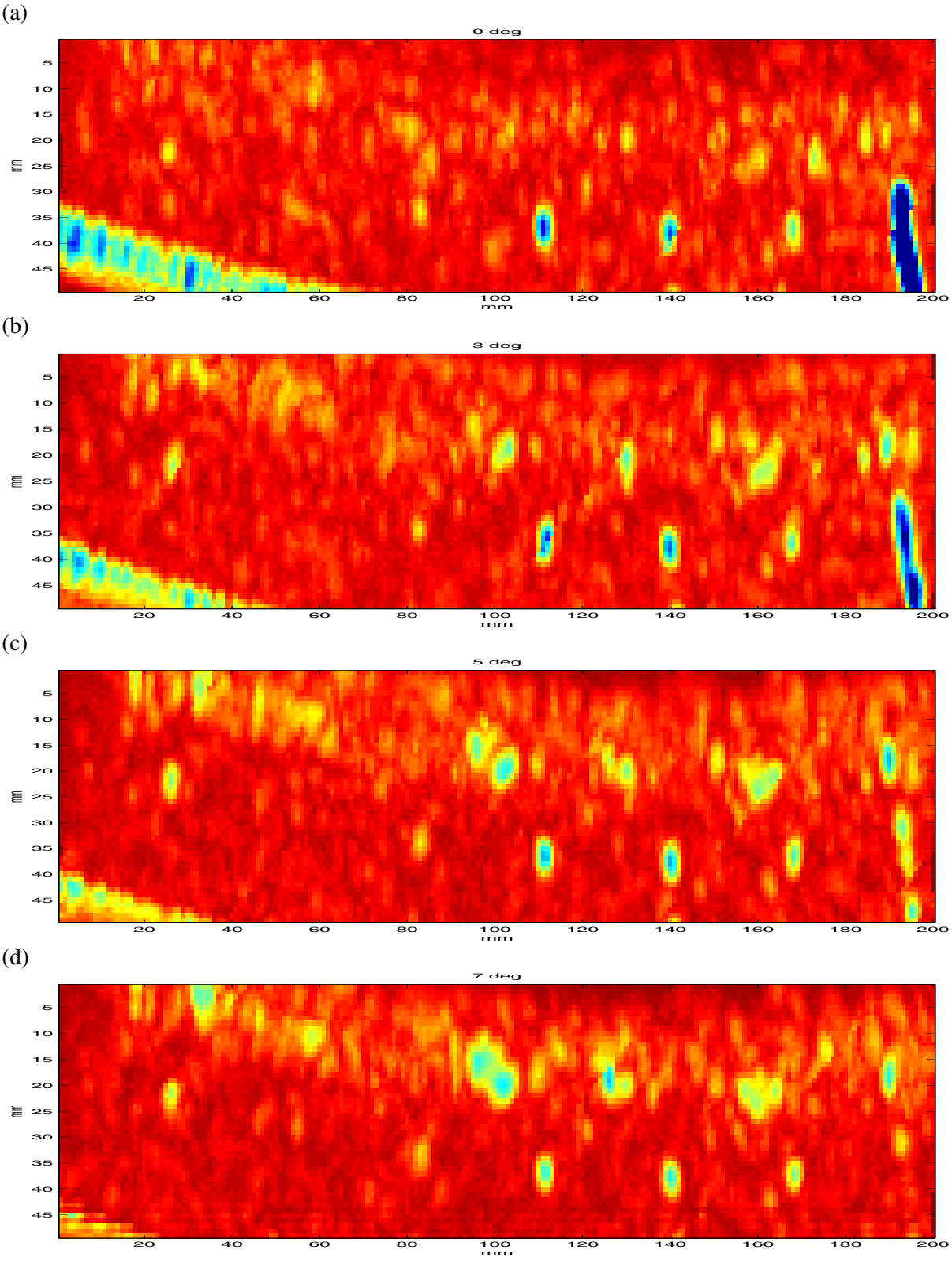

Fig. 3.11. C-scan images of EB weld in block CAN1 for beam launched at different angles in radial direction. (a) for normal beam 0°, (b) for 3°, (c) for 5°, (d) for 7°, and (e) for 10°. C-scans (a)-(e) compounded using averaging (f) and maximization (g).

(e)

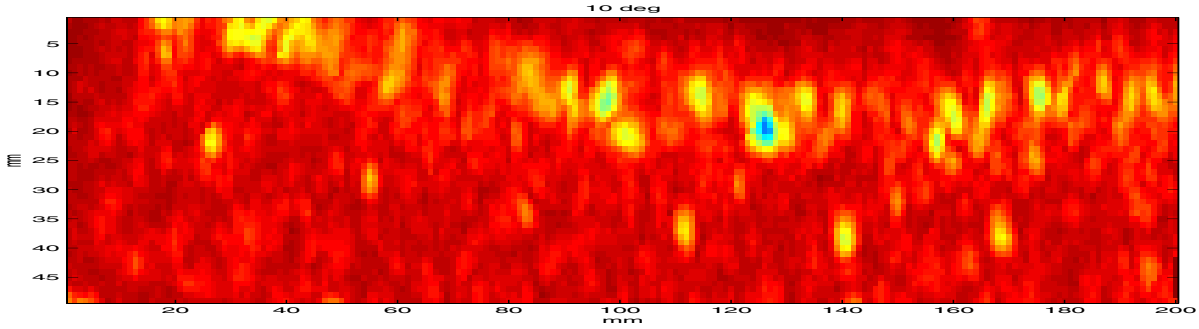

(f)

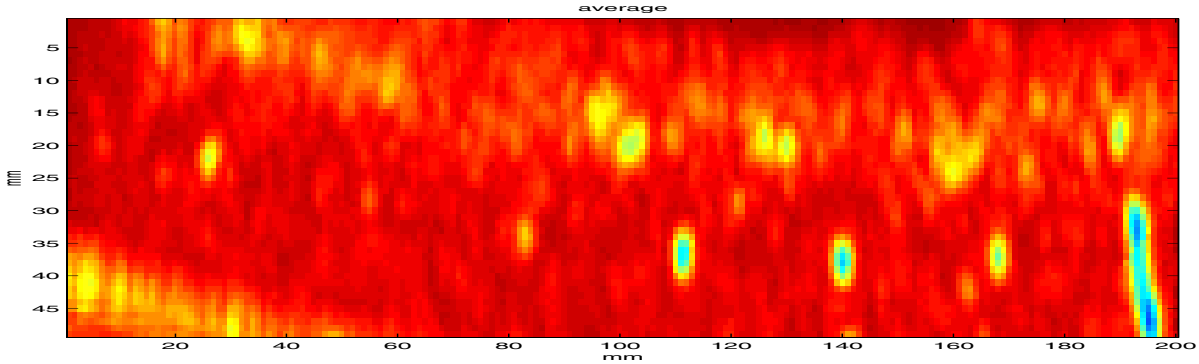

(g)

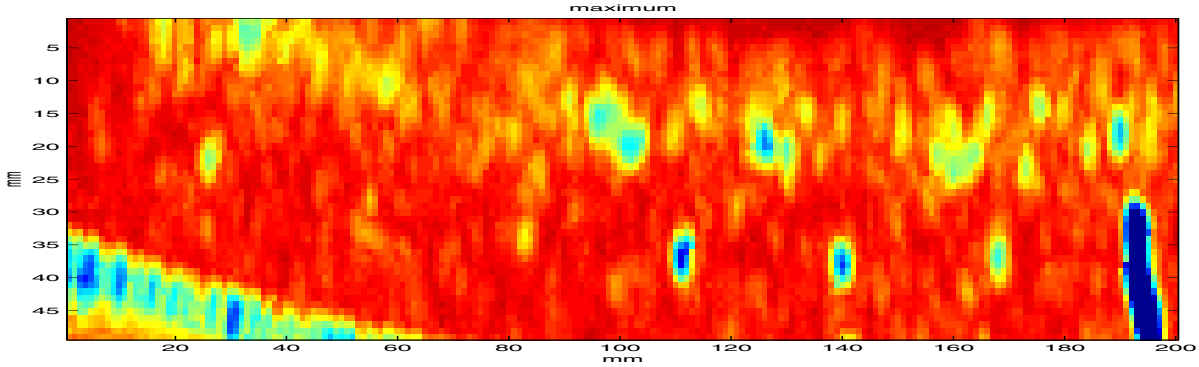

Fig. 3.11. C-scan images of EB weld in block CAN1 for beam launched at different angles in radial direction. (a) for normal beam 0°, (b) for 3°, (c) for 5°, (d) for 7°, and (e) for 10°. C-scans (a)-(e) compounded using averaging (f) and maximization (g).

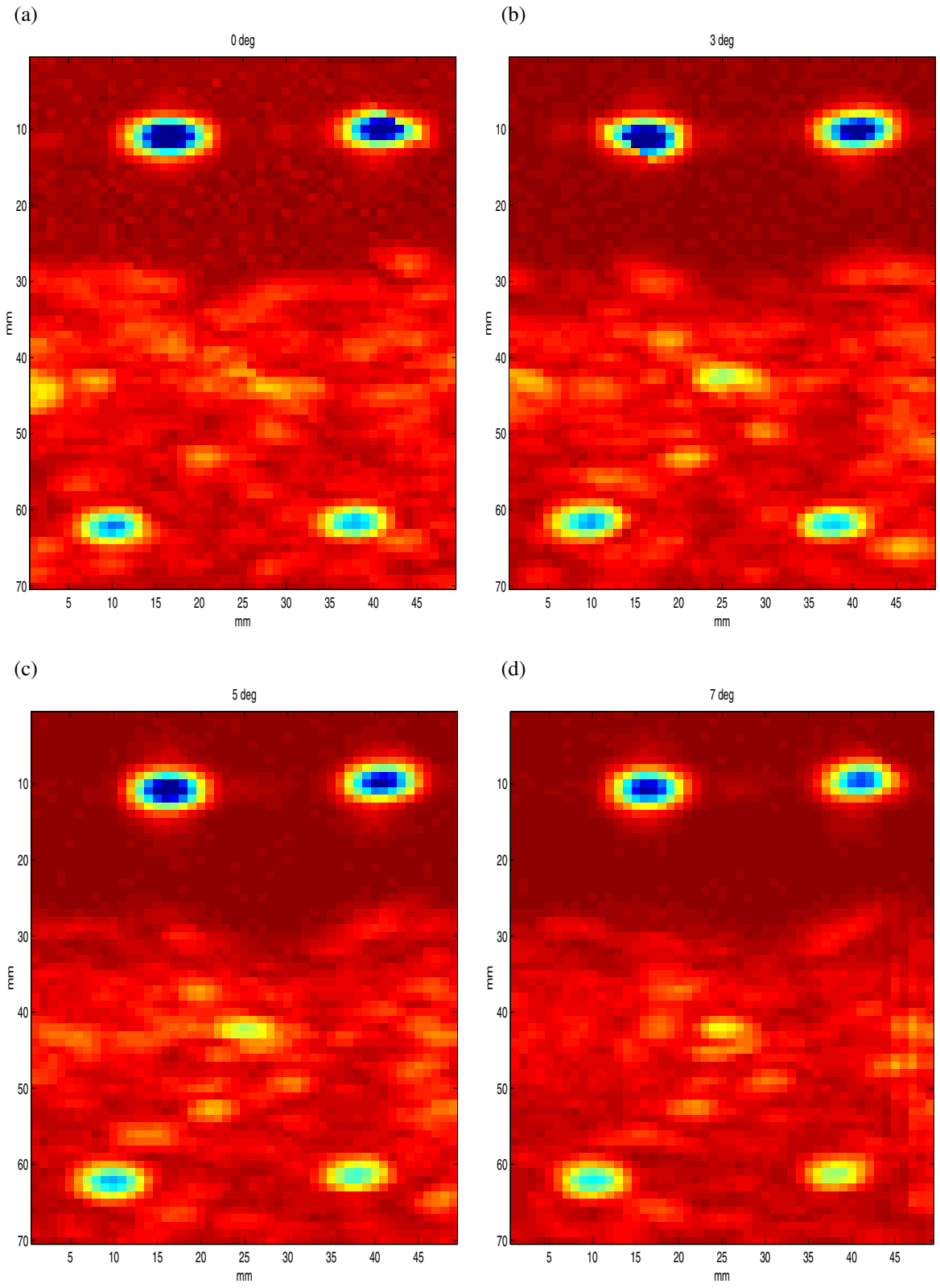

Fig. 3.12. C-scan images of a section of EB weld with flat bottom holes ϕ 2.0 and 2.5 mm in block CAN1 for beam launched at different angles in circumferential direction. (a) for normal beam 0°, (b) for 3°, (c) for 5°, (d) for 7°, and (e) for 10°. C-scans (a)-(e) compounded using averaging (f) and maximization (g).

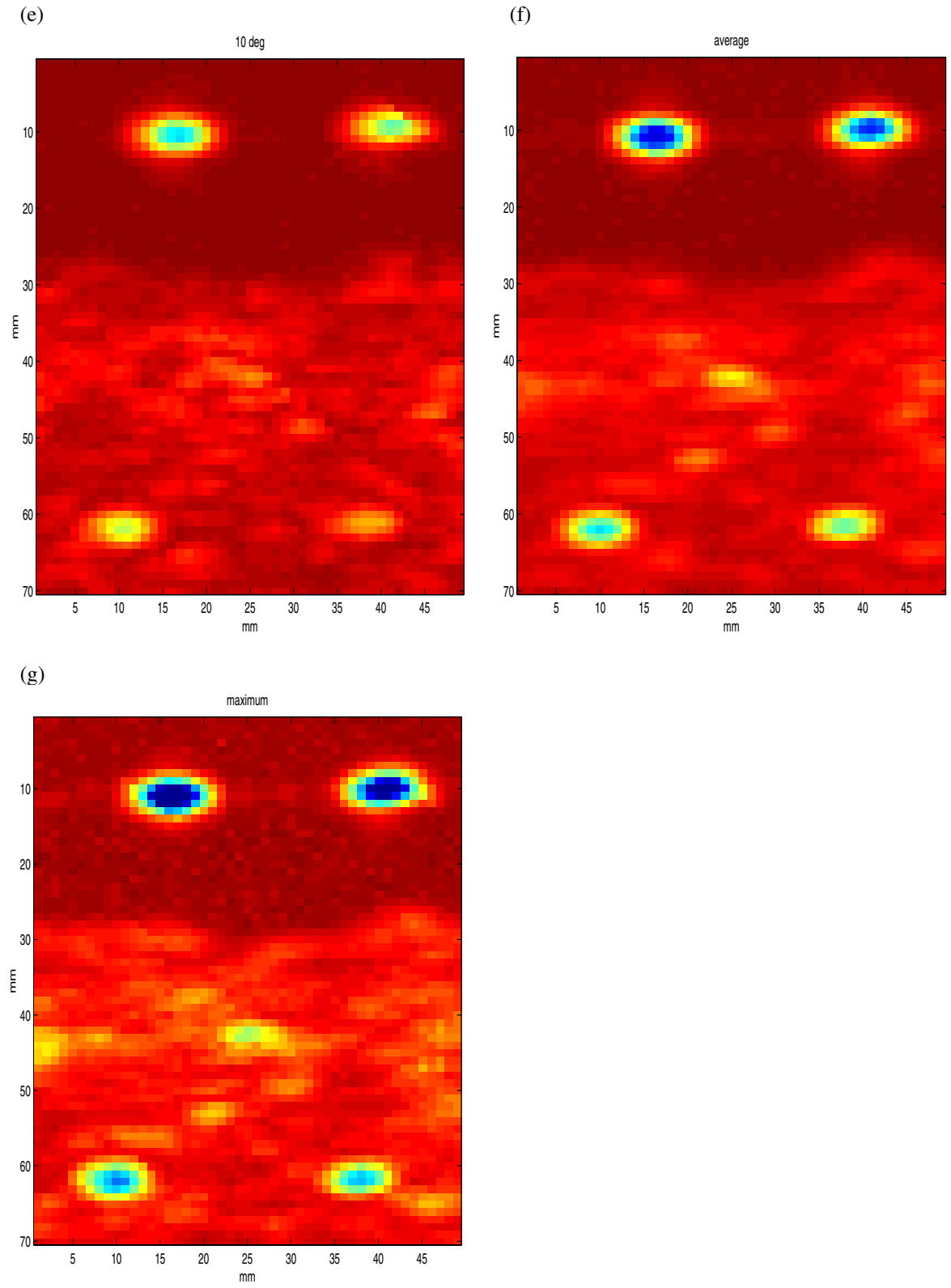

Fig. 3.12. C-scan images of a section of EB weld with flat bottom holes ϕ 2.0 and 2.5 mm in block CAN1 for beam launched at different angles in circumferential direction. (a) for normal beam 0°, (b) for 3°, (c) for 5°, (d) for 7°, and (e) for 10°. C-scans (a)-(e) compounded using averaging (f) and maximization (g).

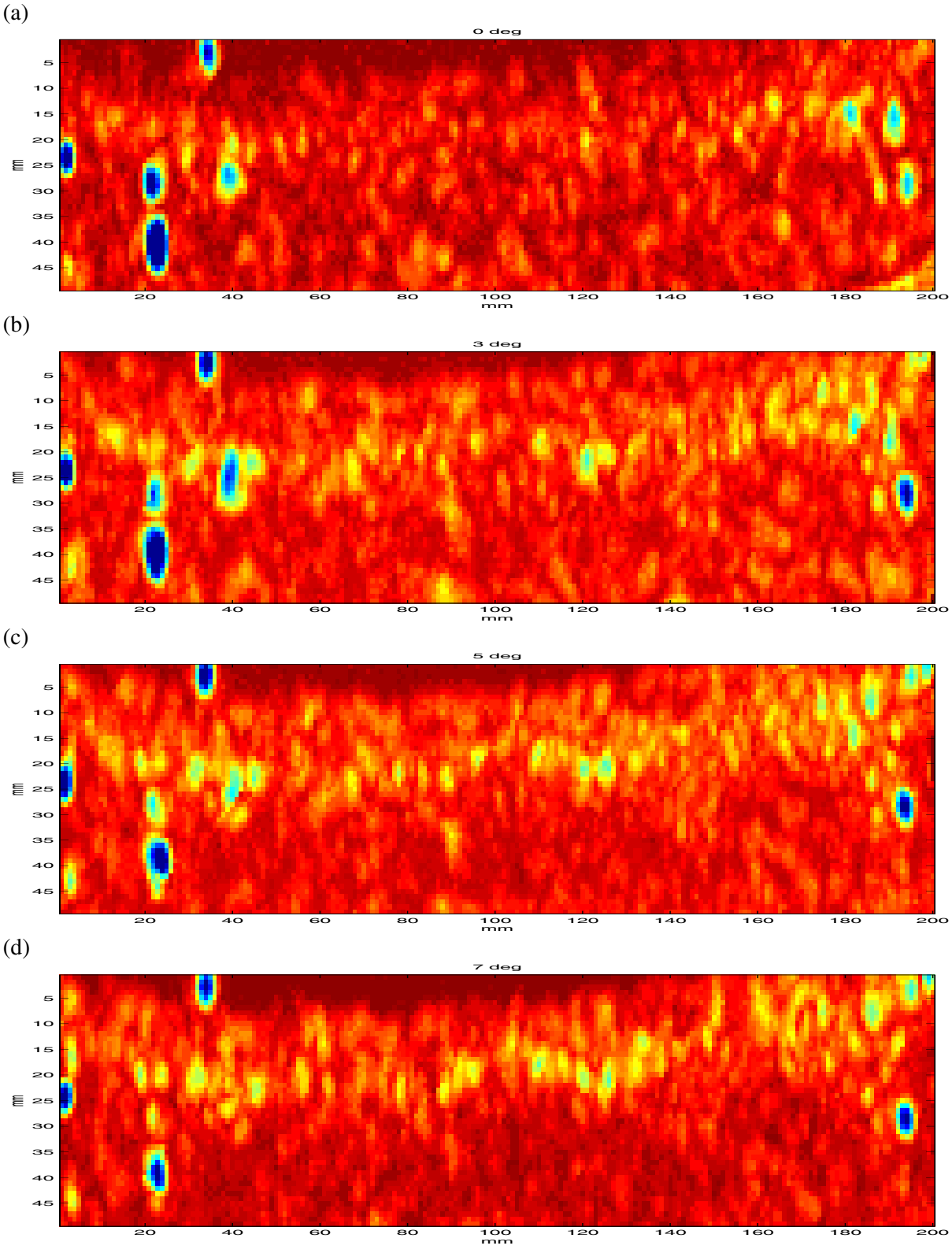

Fig. 3.13. C-scan images of EB weld in Block 3 for beam launched at different angles in radial direction. (a) for normal beam 0°, (b) for 3°, (c) for 5°, (d) for 7°, and (e) for 10°. C-scans (a)-(e) compounded using averaging (f) and maximization (g).

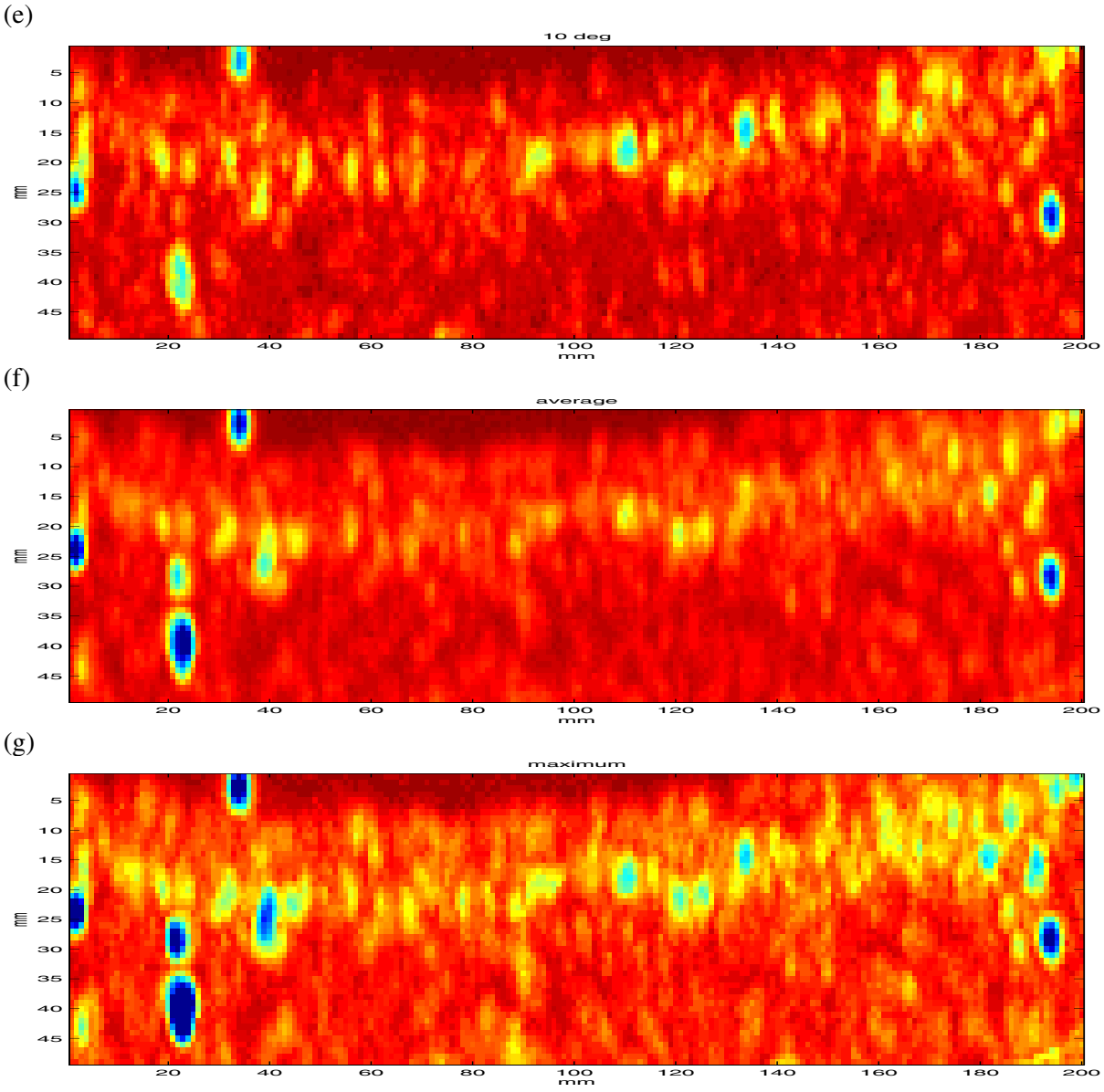

Fig. 3.13. C-scan images of EB weld in Block 3 for beam launched at different angles in radial direction. (a) for normal beam 0°, (b) for 3°, (c) for 5°, (d) for 7°, and (e) for 10°. C-scans (a)-(e) compounded using averaging (f) and maximization (g).

Another way of compounding would be taking maximum amplitude of all pixels in the individual C-scans. This operation should result in enhancement of all the strong scatterers observed at any angle. However, structure noise would be also more pronounced after this operation. Results obtained of maximum operation applied to C-scans acquired for CAN1 and Block 3 is shown in Fig. 3.11 (g) and 3.13 (g), respectively. Round bottom holes in CAN1 cannot be distinguished at the compounded image and the noise has been intensified. However for Block 3 the result seems to be positive, the strong reflectors are very well pronounced in the background noise.

3.4.3 Discussions

Experiments with frequency diversity techniques used for suppressing microstructure noise in the weld zone gave negative result, no improvement was observed after processing ultrasonic data using NCD algorithms, capable of reducing grain noise in copper. This could be explained by the fact that due to very similar frequency responses, ultrasonic responses from flaws and weld microstructure cannot be resolved using frequency diversity approach. Other features should be investigated, one natural candidate is phase of the ultrasonic pulse. When ultrasonic wave in solid is reflected from a void or inclusion (volumes characterized by low acoustic impedance) phase of the received ultrasonic pulse is reversed. Phase change should not normally occur for the reflections from the weld microstructure. Designing an appropriate phase detector (which is not a trivial task) would enable extracting ”phase C-scans” and detecting volumetric flaws.

Spatial diversity approach has been investigated by using steered beams with different angles generated in an electronic way by the array. The resulting C-scans demonstrate variation of the backscattering pattern for different angles. The presence of striations in weld microstructure could be associated to the observed backcsattering patterns. Two methods of compunding individual C-scans were demonstrated, first based on averaging and second on maximization of pixel amplitude. Averaging, used in medical applications is capable of suppressing random scattering but can also result in weaker signal from flaws if their response depends on the beam angle. Amplitude maximization results in enhancement of all scatterers including backscattering from the weld microstructure. Thus preliminary tests show some potential of spatial diversity but more effort is required to evaluate it.

Generally, we can conclude that detecting responses of small flaws embedded in backscattering from the weld structure requires using specialized tools that are unavailable today.

3.5 Conclusions

Attenuation and grain noise in solid materials and welds have been investigated theoretically and experimentally. Suppression of grain noise from welds has been conducted experimentally.

Having employing the log-spectral difference method and the spectral shift method, we have evaluated attenuation in copper specimens of different grades. From the experiments made, it follows that the spectral shift method gives a stable estimation of attenuation when the echoes from front and back surfaces of a specimen are used. The results obtained from the spectral shift method have been presented, and they have shown that the larger the size of grains in copper the higher the acoustic attenuation in the copper. This is in agreement with theory.

To estimate grain noise, we have used two statistical models, i.e., the independent scattering model (ISM) and the K-distribution model. The ISM has been applied to estimate grain noise in three copper specimens with different grades. The results have shown that the model gives good prediction in the shallow regions of copper specimens (i.e., the early time portions of signals). This is reasonable because the approximation under which the model is established is expected to be valid for the early time portion of a signal when the main beam has not been significantly attenuated. The results have also demonstrated that the figure of merit FOM obtained from the ISM can be a good parameter used for depicting grain noise severity. The K-distribution model has been further exploited and applied to evaluate grain noise from welds in copper canisters, and also applied to detect defects in welds. The results have shown that the K parameters obtained in the regions of interest (ROIs) excluding flaws are different from those in the ROIs including flaws. The probability density function (pdf) obtained from the K parameters in the former case (the ROIs excluding flaws) gives good prediction to the measured one, but it does not in the latter case.

To suppress structure noise in weld, formerly developed frequency diversity technique has been applied. Unfortunately, no improvement has been observed after processing the ultrasonic data using noncoherent detector (NCD). A novel technique based on the concept of spatial diversity has been proposed for the suppression of noise in the weld zone. The spatial diversity is realized by using a set of beams steered at different angles by the array. The preliminary tests have shown some potential for the noise suppression, but more effort is needed to evaluate it.

3.6 References

[1] E.P. DeGarmo, J.T. Black, and R. A. Kohser, *Materials and Processes in Manufacturing*. 7th Edition, Macmillan Publishing Company, New York, Chap. 3, pp.63-81,1990.

[2] A.W. Lipsett, R.J. Tait, J.B. Haddow, and A.I. Beltzer, "A comparison study of transient waves in random (polycrystalline) media," *J. Nondestr. Eval.* vol. 11, pp. 9-17, 1992.

[3] Y. Li, and B.B. Thompson, "Relations between elastic constants C_{ij} and texture parameters for hexagonal materials," *J. Appl. Phys.* vol. 67, pp. 2663-2665, 1990.

[4] C.J. Yu, J.C. Conway, Jr, J. Hirsch, C.O. Ruud, and K.J. Kozaczek, "Application of nondestructive techniques for the prediction of elastic anisotropy of a textured polycrystalline materials," *J. Nondestr. Eval.* vol. 12, pp. 79-95, 1993.

[5] M.G. Silk, "Relationship between metallurgical texture and ultrasonic propagation," *Met. Sci.* vol. 15, pp. 559-565, 1981.

[6] T. Stepinski, and P. Wu, *Ultrasonic Inspection of Nuclear Copper Canisters*, SKB Projektrapport 97-01, December 1996.

[7] T. Stepinski, and P. Wu, *Ultrasonic Inspection of Nuclear Copper Canisters*, SKB Projektrapport 97-08, August 1997.

[8] J. Krautkrämer and H. Krautkrämer, *Ultrasonic Testing of Materials*. 4th Edition, Springer-Verlag, Berlin, (1990).

[9] H. Willems and K. Goebbels, "Characterization of microstructure by backscattered ultrasonic wvaes," *Met. Sci.* vol. 15, pp. 549-553, 1981.

[10] R.L. Smith, WN. Reynolds, and H.N.G. Wadley, "Ultrasonic attenuation and microstructure in low-carbon steels," *Met. Sci.* vol. 15, pp. 554-558, 1981.

[11] S.P. Neal, and D.O. Thompson, "The measurement and analysis of acoustic noise as a random variable," in *Rev. of Progr. in Quantitative NDE.*, vol. 9, pp. 625-632, 1990.

[12] P. M. Shankar, P. Karpur, V.L. Newhouse, and J.L. Rose, "Split-spectrum processing: analysis of polarity threshold algorithm for improvement of signal-to-noise ratio and detectability in ultrasonic signals," *IEEE Trans. Ultrason. Ferroelec. Freq. Contr.* vol. 36, pp. 101-108, 1989.

[13] M.G. Gustafsson, "Nonlinear clutter supression using split spectrum processing and optimal detection," *IEEE Trans. Ultrason. Ferroelec. Freq. Contr.* vol. 43, pp. 109-124, 1996.

[14] M.G. Gustafsson, and T. Stepinski, "Studie of split spectrum processing, optimal detection, and maximum likelihood amplitude estimation using a simple clutter model," *Ultrasonics* vol. 35, pp. 31-52, 1997.

[15] I. Yalda, F.J. Margetan, and R.B. Thompson, "Predicting ultrasonic grain noise in polycrystals: a Monte Carlo model," *J. Acoust. Soc. Am.* vol. 99, pp. 3445-3455, 1996.

[16] R.B. Thompson, F.J. Margetan, and Y.H.K. Han, "Relationship of microstructure to backscattered ultrasonic noise," in *Rev. of Progr. in Quantitative NDE.*, vol. 11, pp. 1685-1691, 1992.

[17] K.Y. Han, R.B. Thompson, F.J. Margetan, and J. Rose, "Relationships between ultrasonic noise and microstructure of titanium alloys," in *Rev. of Progr. in Quantitative NDE.*, vol. 11, pp. 1743-1750, 1993.

[18] W.P. Mason, and H.J. McSkimin, "Attenuation and scattering of high frequency sound waves in metals and glasses," *J. Acoust. Soc. Am.* **19:** 464-473 (1947).

[19] W.P. Mason, and H.J. McSkimin, "Energy losses of sound waves in metals due to scattering and diffusion," *J.Appl. Phys.* **19:** 940-946 (1948).

[20] W. Roth, "Scattering of ultrasonic radiation in polycrystalline metals," *J.Appl. Phys.* **19:** 901-910 (1948).

[21] E.P. Papadakis, "Ultrasonic attenuation caused by scattering in polycrystalline metals," *J. Acoust. Soc. Am.* **37:** 711-717 (1965).

[22] E.P. Papadakis, "Ultrasonic attenuation caused by scattering in polycrystalline media," in *Physical Acoustics*, ed. W.P. Mason, Academic Press, New York. **4** Part B: 269-328 (1968).

[23] E.P. Papadakis, "Scattering in polycrystalline media," in *Methods of experimental physics: -- Ultrasonics*, ed. P.E. Edmonds, Academic Press, New York. **19**: 237-299 (1981).

[24] A.B. Bhatia, "Scattering of high-frequency sound waves in polycrystalline materials," *J. Acoust. Soc. Am.* **31:** 16-23 (1959).

[25] A.B. Bhatia, "Scattering of high-frequency sound waves in polycrystalline materials. II," *J. Acoust. Soc. Am.* **31:** 1140-1141 (1959).

[26] F.E. Stanke, and G.S. Kino, "A unified theory for elastic wave propagation in polycrystalline materials," J. Acoust. Soc. Am., Vol. 75, pp. 655-681, 1984.

[27] S. Hirsekorn, "The scattering of ultrasonic waves by polycrystals," J. Acoust. Soc. Am., Vol. 72, pp. 1021-1031, 1982.

[28] S. Hirsekorn, "The scattering of ultrasonic waves by polycrystals. II. Shear waves," J. Acoust. Soc. Am., Vol. 73, pp. 1160-1163, 1983.

[29] S. Hirsekorn, "The scattering of ultrasonic waves by multiphase polycrystals," J. Acoust. Soc. Am., Vol. 83, pp. 1231-1241, 1988.

[30] H. Seki, A. Granato, and R. Truell, "Diffraction effects in the ultrasonic field of a piston source and their importance in the accurate measurement of attenuation," *J. Acoust. Soc. Am.* **28:** 230-239 (1956).

[31] E.P. Papadakis, "Ultrasonic diffraction from single apppertures with application to pulse measurements and crystal physics," in *Physical Acoustics*, ed. W.P. Mason, Academic Press, New York. **11**, 151-211 (1975).

[32] F.J. Margetan, T.A. Gray, and R.B. Thompson, "A technique for quantitatively measuring microstructurally induced ultrasonic noise," in *Rev. of Progr. in Quantitative NDE.*, vol. 10, pp. 1721-1728, 1991.

[33] F.J. Margetan, and R.B. Thompson, "Microstructural noise in titanium alloys and its influence on the detectability of hard-alpha inclusions," in *Rev. of Progr. in Quantitative NDE.*, vol. 11, pp. 1717-1724, 1992.

[34] F.J. Margetan, R.B. Thompson, and I. Yalda-Mooshabad, "Modeling ultrasonic microstructural noise in titanium alloys," in *Rev. of Progr. in Quantitative NDE.*, vol. 12, pp. 1735-1742, 1993.

[35] J.H. Rose, "Ultrasonic backscattering from polycrystalline aggregates using time-domain linear response theory," in *Rev. of Progr. in Quantitative NDE.*, vol. 10, pp. 1715-1720, 1991.

[36] J.H. Rose, "Ultrasonic backscatter from microstructure," in *Rev. of Progr. in Quantitative NDE.*, vol. 11, pp. 1677-1684, 1992.

[37] J.H. Rose, "Theory of ultrasonic backscatter from multiphase polycrystalline solids," in *Rev. of Progr. in Quantitative NDE.*, vol. 12, pp. 1719-1726, 1993.

[38] R. Kuc, "Estimation of acoustic attenuation from reflected ultrasound signals: Comparison of spectral-shift and spectral-difference approaches," *IEEE Trans. Acoust. Speech, Signals Process.* vol. ASSP-32, pp. 1-6, 1984.

[39] R. Kuc, "Bounds on estimating the acoustic attenuation of small tissue regions from reflected ultrasound," *Proc. IEEE.* vol. 73, pp. 1159-1168, 1985.

[40] P.B. Nagy, and L. Adler, "Scattering induced attenuation of ultrasonic backscattering," in *Rev. of Progr. in Quantitative NDE.*, vol. 7, pp. 1263-1271, 1988.

[41] K. Lücke, "Ultrasonic attenuation caused by thermoelstic heat flow," *J.ppl. Phys.* **27:** 1433-1438 (1956).

[42] R.L. Granato, and K. Lücke, "," *J.ppl. Phys.* **27:** 583-593 (1956).

[43] J. Saniie, and N. M. Bilgutay, "Quantitative grain size evaluation using ultrasonic backscattered echoes," *J. Acoust. Soc. Am.* **80:** 1816-1824 (1986).

[44] J. Saniie, T. Wang, and N. M. Bilgutay, "Statistical evaluation of backscattered ultrasonic grain signals," *J. Acoust. Soc. Am.* **84:** 400-408, (1988).

[45] K.B. Ocheltree and L.A. Frizzell, "Sound field calculation for rectangular sources," *IEEE Trans. Ultrason. Ferroelec. Freq. Contr.* vol. 36, pp. 242-248, 1989.

[46] R.L. Roderick, and R. Truell, "Measurement of ultrasonic attenuation in solids by the pulse technique and some results in steel," *J.Appl. Phys.* **23:** 267-279 (1952).

[47] E.P. Papadakis, "Ultrasonic velocity and attenuation: measurement methods with scientific and industrial applications," in *Physical Acoustics*, ed. W.P. Mason, Academic Press, New York. **12**: 277-374 (1976).

[48] M.A. Breaseale, J.H. Cantrel, Jr., and J.S. Heyman, "Ultrasonic wave velocity and attenuation measurements," in *Methods of experimental physics: -- Ultrasonics*, ed. P.E. Edmonds, Academic Press, New York. **19**: 67-135 (1981).

[49] P. Wu, R. Kazys and T. Stepinski, "Analysis of the numerically implemented angular spectrum approach based on the evaluation of two-dimensional acoustic fields--Part I: Errors due to the discrete Fourier transform and discretization," *J. Acoust. Soc. Am.* **99:** 1339-1348 (1996).

[50] P. Wu, R. Kazys and T. Stepinski, "Analysis of the numerically implemented angular spectrum approach based on the evaluation of two-dimensional acoustic fields--Part II: Characteristics as a function of angular range," *J. Acoust. Soc. Am.* **99:** 1349-1359 (1996).

[51] P. Wu, R. Kazys and T. Stepinski, "Optimal selection of parameters for the angular pectrum approach to numerically evaluate acoustic fields," *J. Acoust. Soc. Am.* **101**: 125-134, (1997).

[52] L.E. Kinsler, A.R. Frey, A.B. Coppens, and J.V. Sanders, *Fundamentals of Acoustics*. Wiley, New York, Chap. 7, (1982).

[53] P. Cervenka, and P. Challande, "A new efficient algorithm to compute the exact reflection and transmission factors for plane waves in layered absorbing media (liquids and solids)," *J. Acoust. Soc. Am.* **89:** 1579-1589, (1991).

[54] M. Deschamps and P. Chevée, "Reflection and refraction of a heterogeneous plane wave by a solid layer," *Wave Motion* **15:** 61-75, (1992).

[55] L. Vergara-Domínguez, and J.M. Páez-Borrallo, "Backscattering grain noise modelling in ultrasonic non-destructive testing," *Waves in Ranom Media* **1:** 81-92, (1991).

[56] B.A. Auld, *Acoustic Fields and Waves in Solids*, 2nd Ed. Malabar, Florida: Krieger Publishing Company, Vol. I, Chap. 4, 1990.

[57] B.A. Auld, "General electromechanical reciprocity relations applied to the calculation of elastic wave scattering coefficients," *Wave Motion,* vol. 1, pp. 3-10, 1979.

[58] B.A. Auld, *Acoustic Fields and Waves in Solids*, 2nd Ed. Malabar, Florida: Krieger Publishing Company, Vol. II, Chap. 10, 1990.

[59] R.B. Thompson, and T.A. Gray, "A model relating ultrasonic scattering measurements through liquid-solid interfaces to unbounded medium scattering amplitudes," *J Acoust. Soc. Am.,* vol. 74(4), pp. 1279-1290, 1983

[60] W.H. Bowyer, and R.L. Crocker, *Modelling of attenuation and scattering of ultrasound in polycystalline copper*, SKI Projektrapport, Order number 95062, Jan. 1997.

[61] A. Sanderson, TF Szluha, C N Ribton, B G Dance and A B Day, The Application of High Power Non-Vacuum EB Welding for Encapsulation of Nuclear Waste at Reduced Pressure, SKB Inkapsling, Projektrapport 94-01, January 1994

[62] L. Ericsson, M.G. Gustafsson, Perceptron and entropy inspired ultrasonic grain noise suppression using noncoherent detector statistics, presented at 7th ECNDT, Copenhagen, May 1998.

Appendix 3-A. Transient plane waves in a attenuating solid layer immersed in a lossless fluid

Consider the case shown in Fig. 3.1 where a solid plate has thickness D and attenuation coefficient α, and it is submerged in a lossless fluid and located in the plane $z = z_{fs}$.

In general, when a plane wave p impinges on the plate at incident angle θ, it excites a reflected plane wave, a transmitted longitudinal wave (LW), and a transmitted shear wave (SW) at the fluid/solid interface (front surface), and the transmitted LW and SW travel to the solid/ fluid interface (back surface), reflect, propagate back to the front surface and transmit into the fluid. In the case of normal incidence, i.e., when $\theta = 0$, only LW is excited and propagates in the solid plate.

Here we only deal with the normal incident case. Suppose a transient plane wave $p(z, t)$ propagating in a lossless fluid. It is well known that a transient plane wave can be decomposed into an infinite set of continuous plane waves by means of Fourier transform. The component of the transient plane wave at frequency ω can be written as

$$P(z,\omega) = P_0(\omega)\exp(jk_0 z). \tag{A3.1}$$

The plane wave reflected from the front surface at $z = z_{fs}$ can be written, in terms of pressure, as

$$P_{rF}(z,\omega) = R_{fs}P_0(\omega)\exp\left[-jk_0(z - z_{fs})\right],\ (z \le z_{fs}) \tag{A3.2}$$

where R_{fs} is the reflection coefficient of pressure at the fluid/solid interface. The transmitted longitudinal wave (LW) in terms of particle velocity can be found to be

$$T_L(z,\omega) = \Gamma_{fsL}\exp\left[jk_L(z - z_{fs})\right]P(z_{fs},\omega)),\ (z_{fs} \le z \le z_{fs} + D), \tag{A3.3}$$

where Γ_{fsL} is the transmission coefficient of LW stress (pressure) at the fluid/solid interface. At the back (solid/fluid) interface, the transmitted LW is reflected and the reflected LW can be written as

$$T_{rL}(z,\omega) = R_{sfL}T_L(z_{fs} + D,\omega))\exp\left[-j(z - z_{fs} - D)k_L\right] = R_{sfL}\Gamma_{fsL}\exp\left[-j(z - z_{fs} - 2D)k_L\right]P(z_{fs},\omega)$$
$$(z_{fs} \le z \le z_{fs} + D), \tag{A3.4}$$

where R_{sfL} is the reflection coefficient of LW stress (pressure) at the solid/fluid interface. At the front (solid/fluid) interface, the reflected LW is transmitted, and it can be written as

$$P_{rB}(z,\omega) = \Gamma_{sfL} T_{rL}(z_{fs},\omega)\exp\left[-j(z-z_{fs})k_z\right] = \Gamma_{sfL} R_{sfL} \Gamma_{fsL} \exp(j2Dk_L)\exp\left[-j(z-z_{fs})k_z\right] P(z_{fs},\omega), \quad (z \le z_{fs}) \tag{A3.5}$$

where Γ_{sfL} is the transmission coefficient of LW stress (pressure) at the solid/fluid interface. From Eqs. (A3.1) - (A3.5), and with substitution of $k_L = k_{0L} + j\alpha_L$, we can find the attenuation coefficient of the solid plate to be

$$\alpha_L(\omega) = \frac{1}{2D}\ln\frac{\left|\Gamma_{sf} R_{sf} \Gamma_{fs} P_{rF}(z,\omega)\right|}{\left|R_{fs} P_{rB}(z,\omega)\right|} = \frac{1}{2D}\ln\frac{\left|\Gamma_{sf} R_{sf} \Gamma_{fs}\right|}{\left|R_{fs}\right|}\frac{\left|P_{rF}(z,\omega)\right|}{\left|P_{rB}(z,\omega)\right|}. \tag{A3.6}$$

In the normal incident case , R_{fs} , R_{sfL} , Γ_{fs} and Γ_{sfL} are expressed as [8]

$$R_{fs} = \frac{\rho_s c_L - \rho c}{\rho_s c_L + \rho c},\ R_{sfL} = \frac{\rho c - \rho_s c_L}{\rho c + \rho_s c_L},\ \Gamma_{fs} = \frac{2\rho_s c_L}{\rho c + \rho_s c_L},\ \Gamma_{sfL} = \frac{2\rho c}{\rho c + \rho_s c_L}. \tag{A3.7}$$

Thus, Eq. (A3.6) reduces to

$$\alpha_L(\omega) = \frac{1}{2D}\ln\frac{4\rho c \rho_s c_L}{(\rho c + \rho_s c_L)^2}\frac{\left|P_{rF}(z,\omega)\right|}{\left|P_{rB}(z,\omega)\right|} = \frac{1}{2D}\ln\frac{\left|P_{rF}(z,\omega)\right|}{\left|P_{rB}(z,\omega)\right|} + \frac{1}{2D}\ln\frac{4\rho c \rho_s c_L}{(\rho c + \rho_s c_L)^2}. \tag{A3.6a}$$

Eq. (A3.6a) indicates that evaluation of attenuation in a solid plate using the reflected waves from the front and the back interface needs to take into account transmission ratios at both interfaces.

Appendix 3-B. Theory for modeling grain noise

A polycrystalline metal is made up of discrete grains, each having a regular, crystalline structure. The grains are anisotropic in elastic properties, and their crystallographic axes are randomly oriented with respect to fixed laboratory axes. As a result, the elastic constants of the metal measured in the laboratory coordinate system are microscopically inhomogeneous. An ultrasound propagating in such an inhomogeneous medium suffers scattering and consequently has an amplitude attenuation and a

phase velocity variation with frequency. The equation of motion in the inhomogeneous medium in the absence of body force is given by [56]

$$\nabla \cdot \mathbf{T} = \rho \frac{\partial \mathbf{v}}{\partial t}, \text{ or } \frac{\partial T_{ij}}{\partial r_j} = \rho \frac{\partial v_i}{\partial t}, \ (i, j = x, y, z), \tag{B3.1}$$

where r_i are Cartesian coordinates, **v** and **T** are particle velocity and stress tensor of 2nd rank, respectively. Stress **T** is related to strain **S** by the elastic constitutive equation,

$$\mathbf{T} = \mathbf{c}:\mathbf{S}, \text{ or } T_{ij} = c_{ijkl} S_{kl}, (i, j, k, l = x, y, z), \tag{B3.2}$$

where **c** is elastic constant tensor of 4th rank. Strain **S** is associated with displacement **u** in the relation

$$\mathbf{S} = \nabla_s \mathbf{u}, \text{ or } S_{ij} = \frac{1}{2}\left(\frac{\partial u_i}{\partial r_j} + \frac{\partial u_j}{\partial r_i} \right), (i, j = x, y, z). \tag{B3.3}$$

The elastic constants c_{ijkl} do not vary within a grain but change from grain to grain if the inhomogeneity is only caused by different orientations of the grains. For the inhomogeneity, the density ρ and the elastic constants c_{ijkl} are supposed to vary as a function of position within the medium, i.e., [26,27]

$$\rho(\mathbf{r}) = \rho_0 + \delta\rho(\mathbf{r}), \tag{B3.4}$$

and

$$c_{ijkl}(\mathbf{r}) = \left\langle c_{ijkl}(\mathbf{r}) \right\rangle + \delta c_{ijkl}(\mathbf{r}), \tag{B3.5}$$

where ρ_0 and $\left\langle c_{ijkl}(\mathbf{r}) \right\rangle$ are the average values of the density and the elastic constants, respectively. Below, we will use the above notations to derive the backscattering from a polycrystalline metal.

A. Backscattering signals from grains

The backscattering (pulse-echo) signals from a polycrystalline metal will be formulated by means of the electromechanical reciprocity relations given by Auld [57,58]. The reciprocity relations are the theorem relating two different solutions to a given set of field equations. From a set of partial equations that characterize a physical field, it is almost possible to derive one or more reciprocity relations defining relations between two possible solutions to the field equations. In many cases,

reciprocity relations are marvellously efficient machines for manufacturing the analytical tools needed in solving applied field problems. Auld [57] derived an expression that directly related the electrical signal received by an ultrasonic receiver to the fields from a transmitter and their modification by scattering from a flaw. It was noted that a significant advantage of reciprocity relation analysis of bulk wave scattering is that it includes directly the diffraction effects of the transducers used in an experiment. The Auld's reciprocity relations have been much applied to NDT [59,35-37].

From [57], the electromechanical reciprocity relation is expressed as

$$\delta\Gamma = \Gamma'_{ba} - \Gamma_{ba} = \frac{1}{4P}\int_{S_F}\left(\mathbf{v}_1\cdot\mathbf{T}_2 - \mathbf{v}_2\cdot\mathbf{T}_1\right)\cdot\hat{\mathbf{n}}dS\ . \tag{B3.6}$$

It states that the flaw-induced variation in the transmission coefficient, $\delta\Gamma = \Gamma'_{ba} - \Gamma_{ba}$, is given by $\int(\mathbf{v}_1\cdot\mathbf{T}_2 - \mathbf{v}_2\cdot\mathbf{T}_1)\cdot\hat{\mathbf{n}}dS/(4P)$, where the velocity and stress fields $(\mathbf{v}_1, \mathbf{T}_1)$ are those that would have been generated in the solid, in the absence of the flaw, in response to an electric excitation carrying power P in coaxial line a. The fields $(\mathbf{v}_2, \mathbf{T}_2)$ are the corresponding fields that would be generated in the solid, in the presence of the flaw, in response to an electric excitation carrying power P in coaxial line b. The integration is conducted over the closed surface S_F whose normal $\hat{\mathbf{n}}$ is inward directed.

By using Gauss' theorem and the relations in Eqs. (B3.1)-(B3.3), Eq. (B3.6) for the time-harmonic case can be written as

$$\delta\Gamma = \frac{-i\omega}{4P}\int_{V_F}\left[\mathbf{S}_2 : \delta\mathbf{c} : \mathbf{S}_1 - \delta\rho\omega^2\mathbf{u}_2\cdot\mathbf{u}_1\right]dV = \frac{-i\omega}{4P}\int_{V_F}\left[\delta c_{ijkl}\frac{\partial u_{(1)i}}{\partial r_j}\frac{\partial u_{(2)k}}{\partial r_l} - \delta\rho\omega^2 u_{(1)i}u_{(2)i}\right]dV\ , \tag{B3.7}$$

where $\delta\mathbf{c} = \mathbf{c}_2 - \mathbf{c}_1$ and $\delta\rho = \rho_2 - \rho_1$, and V_F is the volume enclosed by S_F. The displacement field $\mathbf{u}_2$ is computed from the inhomogeneous solid medium in the presence of scatterer. The displacement field $\mathbf{u}_1$ is computed from the corresponding homogeneous solid with the average properties in the absence of scatterer. Therefore, $\delta\rho$ and δc_{ijkl} in Eq. (B3.7) can be expressed by Eqs. (B3.4) and (B3.5), respectively, with the variation of ρ and c_{ijkl} only happening when $\mathbf{r}$ moves from inside to outside the single scatterer.

As is mentioned above, Eq. (B3.7) is derived for the single scatterer case. For a polycrystalline metal, there are a large number of scatterers (grains) scattering the incident field. In this case, V_F should contain all the scatterers insonified by the incident beam. $\delta\rho$ and δc_{ijkl} in Eq. (B3.7) are determined by Eqs. (B3.4) and (B3.5), respectively.

The expression for the voltage variation in Eq. (B3.7) is related with the transducer response function as well as with the properties of the polycrystalline material. The effects of the transducer response function can to a certain degree be removed by dividing the results of a reference experiment (for example, the reference echo from the front surface of a test sample), and after deconvolution by the reference echo, one obtains a normalized signal $S(\omega)$ that is given by [35]

$$S(\omega) = \frac{1}{j\omega} \int_{V_F} \left[\delta c_{ijkl} \frac{\partial u_{(1)i}}{\partial r_j} \frac{\partial u_{(2)k}}{\partial r_l} - \delta\rho\omega^2 u_{(1)i} u_{(2)i} \right] dV \ . \tag{B3.8}$$

Eq. (B3.8) is basically intractable since it requires one to know the exact displacement u^2 in the presence of the scatterers.

Starting from Eq. (B3.8) and using the Born approximation (i.e., $\mathbf{u}_2 \cong \mathbf{u}_1$) under the assumptions that the polycrystalline material considered is (i) single phase, (ii) macroscopically uniform and isotropic (i.e., the ensemble average of the material's properties are spatially uniform and isotropic), (iii) of no variation in density (i.e., $\delta\rho = 0$, as expected), and (iv) of a weak variation in elastic constants (i.e., $\left|\delta c_{ijkl}\right| / c_{ijkl} << 1$), Rose [36] gave the backscattered signal amplitude in the following manner,

$$S(\omega) = \frac{1}{4\pi\rho c_1^2} \int_{V_F} \delta c_{ijkl}(\mathbf{y}) u_{(1)i,j} u_{(1)k,l} d^3\mathbf{y} \ . \tag{B3.9}$$

This approximation is expected to be valid for the early time portion of the signal when the main beam has not been significantly attenuated. The backscattered power is easy to obtain via Eq. (B3.8) as follows

$$P(\omega) = \left\langle S(\omega) S^*(\omega) \right\rangle = \frac{1}{\left(4\pi\rho c_1^2\right)^2} \int_{V_F} d^3\mathbf{y} \int_{V_F} \left\langle \delta c_{ijkl}(\mathbf{y}) \delta c_{pqrs}(\mathbf{y}') \right\rangle u_{(1)i,j} u_{(1)k,l} u_{(1)p,q} u_{(1)r,s} d^3\mathbf{y}' . \tag{B3.10}$$

As shown by Rose in [36], Eq. (B3.10) has the following consequences. First, it implies the independent scattering model proposed by Margetan *et al* [32-34]; second, it leads to an explicit formula for single phase materials of hexagonal or cubic symmetry; and finally, it permits us to make a preliminary comparison of theory and experiment.

ISSN 1404-0344
CM Gruppen AB, Bromma, 1999